Novel investigations into the formation and micron-scale analyses of firearm discharge residues: insights from experiments and modelling

by

Vassilia Spathis

Thesis

Submitted to the University of Kent

for the degree of

Doctor of Philosophy

School of Physical Sciences

June 2020

Contents

List of Tables

List of Figures

Acknowledgments

The first amongst many academic acknowledgements must be my supervisor, Dr Mark Price, whose "supreme confidence" and assistance made it possible for me to complete my research. Additionally, I would like to thank Dr Chris Shepherd and Professor Mike Went, without whom my research career may have never taken the direction it did.

There have been many people both within and outside the School of Physical Sciences who have helped me reach the end of my PhD. As such, I would like to thank: the University of Kent for offering me a partial scholarship which allowed me to complete my doctorate; Mr Mark Johnson for his help undertaking the shots I required for my first experiments; Mr Mike Cole for operating the light gas gun; the fine gentlemen of Kent Police in Maidstone, Kent who carried out out a full day of test-firings in the name of science; Phil Marsh for 3-D printing the primer holders I designed; the wonderful women of chemistry and forensic science, with special thanks to Diana Suciu, Faith Taylor and Emerald Taylor, whose encouragement and words of female empowerment in a male dominated industry have been the most pleasant reinforcement; Dr James New for bringing me into the Enceladus project, as well as pestering me to finish this thesis and move on to greater things; the many academic and technical staff in SPS; the Shepherd gang at Canterbury Cathedral who kept reminding me to have fun; Professor Bill Schonberg for his continued support and encouragement and my best friend, Mr Ryan Mayhew, whose daily commentary and light in my life I miss every day.

Finally, the most important individual deserving of the utmost acknowledgement is my beautiful Schrödinger, the most pleasant distraction one could ask for.

Declarations

The content herein was composed by the author, and has not been submitted for the purposes of a qualification at any other institution or for any other degree.

The content comprising Chapter 5 was adapted and extended from work which has been published as Spathis V. (2017).

The content comprising Chapter 7 was adapted and extended from work which has been published as Spathis V. & Price M.C. (2019).

All diagrams were drawn by the author, and all data is the author's own, unless explicitly stated otherwise. All instances where the work of others has been used has been cited.

Abstract

The analysis of gunshot residue (GSR) is an important component in the investigation of shooting cases. Once a firearm has been discharged, gases, vapour and solid particulates originating from the ammunition and firearm, are discharged from the barrel and condense to form GSR. GSRs typically have a characteristic elemental composition of lead, antimony and barium, and a discriminative spheroidal morphology. The examination and distribution of these particles can aid in the understanding and reconstruction of a shooting scene.

In this set of experiments, the distance range at which GSR particles are present from a firearm was determined using Oxford Instruments' INCA GSR automated software. The individual particle morphologies observed at each distance were also investigated using Scanning Electron Microscopy, in conjunction with Energy Dispersive X-ray spectroscopy, allowing for the morphological and compositional analyses of GSR at the sub-micron level. These analyses gave rise to the identification of a range of particles with molten-like morphologies, referred to as impact-disrupted GSR, that were previously uncharacterised. These particles were classified according to the degree of melting experienced but the morphologies observed did not appear to be composition-dependent. Instead, they were attributed to the differing cooling times experienced by particles prior to impact.

Experiments using the University of Kent's Light Gas Gun were then carried out to investigate this hypothesis. The results indicate that the 'uncharacteristic' morphologies were a product of insufficient in-flight cooling, with convective cooling being the dominant cooling mechanism experienced. This was reinforced by hydrocode modelling, which was used to determine the peak temperatures experienced by the projectile, as well as morphological changes to lead impactors as a function of temperature and initial velocity.

The novel sampling and analytical techniques used in this set of experiments have provided previously unknown information regarding GSR morphologies and elemental analyses at the sub-micron level. These findings have highlighted how automated software may be excluding GSR particles from analysis due to their non-spheroidal morphologies, which could have greater implications amongst laboratory and law enforcement agency forensic analyses worldwide. However, the successful modelling of molten and non-molten residue impacts using computer modelling software could potentially be a useful tool to take forward for interpreting forensic data, and provide insight into the metallurgy and physicality of GSR upon impact.

Abbreviations

308Winchester .308" Winchester

ASTM American Society for Testing and Materials

AX308 Accuracy International AX308

BSE Back Scatter Electron

CCD Charged Coupled Device

CDR Cartridge Discharge Residue

C.I.P. Commission Internationale Permanente Pour L'Epreuve Des Armes á Feu Portatives

EDX Energy Dispersive X-ray

FDR Firearm Discharge Residue

FEG-SEM Field Emission Gun Scanning Electron Microscope

FMJ Full Metal Jacketed

GSR Gunshot Residue

G36C Heckler & Koch G36 Carbine

HPLC High Performance Liquid Chromatography

IDGSR Impact-Disrupted Gunshot Residue

IPA Iso-Propyl Alcohol

LGG Light Gas Gun

N.D. Neutral Density Filter

OGSR Organic Gunshot Residue

SAAMI Sporting Arms and Ammunition Manufacturers' Institute

SE Secondary Electron

SEM Scanning Electron Microscope

SPH Smoothed Particle Hydrodynamics

Chapter 1

Introduction

The identification and analysis of gunshot residue (GSR) has played an important role in the investigation of shooting cases. When a cartridge-based weapon is discharged, gaseous and solid residues are expelled from the barrel. These residues primarily consist of burnt and unburnt particles from the primer and propellant initially contained within the ammunition, but may also incorporate trace elements from the bullet, cartridge case, firearm, as well as any previously-existing residues residing within the barrel. Once these residues are discharged, the vaporised particulates rapidly condense, mixing with solid residues to form GSR. The existence of these residues is of particular interest regarding efforts to reconstruct a shooting scene. This can be done by investigating the particle distribution on individuals present during the time of a shooting, as well as within the scene itself. This can allow for the determination of shooting distances (Lichtenberg W. (1990); Maehly A. & Williams R. (1989)), in addition to potentially providing invaluable information regarding the ammunition type used.

Due to the multiple constituents present in the ammunition, GSR consists of both organic and inorganic components. However, it is the inorganic particles that are of particular interest as they form the officially recognised 'characteristic' GSR (American Society for Testing Materials (2017); Wolten G. et al. (1979b)). In order for a particle to be considered to have originated from a firearm, and therefore be classified as GSR, there are two primary criteria that need to be fulfilled. Firstly, the particle must be of a spheroidal morphology, and secondly have a specific elemental composition consisting

primarily of lead (Pb), antimony (Sb) and barium (Ba). Once these criteria have both been met, a particle can be assumed to have been produced during the discharge of a firearm and can be classified as inorganic-GSR.

Over the years particular attention has been drawn to the efficient identification and analysis of GSR. In order to enhance our understanding of this trace evidence and to establish universal analytical protocols, various aspects of GSR have been studied. These range from determining the origin of GSR particles from different areas of a firearm, down to establishing the internal composition of individual particles (Basu S., 1982). The collated findings from such experiments allowed for a standardised guide for GSR analysis to be developed, in which Scanning Electron Microscopy (SEM) in conjunction with Energy-Dispersive X-ray Spectroscopy (EDX) was acknowledged as the best practice for inorganic-GSR particle analysis. As SEM/EDX analysis is non-destructive, and has the ability to produce elemental composition information alongside images of individual particles, it means that the information obtained from each sample is maximised without risking the loss of evidence. This, in turn, has led to the development of automated analytical systems. However, as will be discussed in this thesis, it is evident that the automated analyses are not always as reliable and consistent as they may appear to be.

The objective of this investigation was to examine the formation and impact of these metallic residues in order to determine the metallurgy and physical state of GSR upon impact, and to adjudicate whether present analytical techniques are sufficient for accurate residue identification and analysis. This was done by achieving the following aims:

1. Determine the distance range at which GSR is present and examine individual particle morphologies at each distance.

2. Determine the elemental composition for each particle morphology to establish whether different morphologies are due to varying elemental compositions.

3. Determine whether molten-looking particles are present due to the heat of combustion experienced during firing or due to the force of the impact onto the substrates.

Three different types of firearms were used to produce GSR and provide the samples required to achieve the first two aims listed above. In order to address the goals and determine whether the residues that appear to have molten morphologies are a cause of combustion heat or due to the force of impact, the two stage light gas gun (LGG) at the University of Kent was used to separate the two processes. Moreover, hydrocode modelling using Ansys' AUTODYN software was carried out to determine

whether there was any corroboration between the results obtained during the impact experiments on the LGG and computer simulations. SEM/EDX was used to analyse the samples obtained from all sets of experiments as it provided morphological information as well as elemental composition data for individual particles. A Raman spectrometer was also used to analyse the samples for some of the experiments in order to provide an insight into any organic variations between particles. In particular, this equipment was used to determine whether there were any identifiable differences in the organic composition between spheroidal and molten-looking, impacted particles.

1.1 Outline of Thesis

Chapter 2 provides a general introduction to GSR. It includes the history of GSR analyses and their evolution, as well as the importance of GSR detection. The aim of this chapter is to provide a background into the topics discussed and expanded upon later in this thesis.

Chapter 3 goes into detail regarding the equipment used during this investigation. This section focuses on the SEMs and corresponding EDX detectors, the Raman spectrometer and the University of Kent's light gas gun. Each section provides information on their construction, the theory behind their operating procedures (as well as any limitations) and how each piece of equipment was used for this concept.

Chapter 4 outlines the methodology and discussion for the first experiment, which examined the range that GSR can travel to under environmental conditions but in a closed room, and determine the elemental composition of particles using the automated software INCA GSR. For this experiment, a long rifle semi-automatic pistol along with rim-fire ammunition was used to produce the residues analysed. A description of the experimental set-up, sample acquisition prior to analysis, and preliminary results are given.

Chapter 5 provides the experimental set-up for the investigation into individual particle morphologies and elemental compositions, following on from the results obtained in Chapter 4. The organic variations between particles was also studied in this chapter using Raman spectroscopy. The work presented in this chapter is based on work published in Spathis V. (2017), included as Appendix 1. The substrates, analysis and results from this experiment are also included in this section, followed by a brief discussion.

Chapter 6 contains the experimental procedure and results for the samples acquired using two centre-fire firearm and ammunition combinations under environmental con-

ditions (indoor firing range), courtesy of Kent Police. The results obtained in this section proved largely inconclusive, but a brief discussion is included to elaborate on this.

Chapter 7 outlines the experiments carried out into particle formation and impact melting of the residues using the light gas gun using different gas and pressure environments, along with high velocity, two-stage shots and hydrocode modelling. In this chapter, the study into the two different processes is outlined and the versatility of the University of Kent's LGG is demonstrated. The work presented here is based on work published in Spathis V. & Price M.C. (2019), included as Appendix 2. The results obtained from each investigation are included alongside a discussion.

Chapter 8 involves the overall discussion and interpretation of the results acquired in the previous chapters. Here, the main findings from each section are summarised and combined, providing context and understanding into the research carried out and the results obtained.

Chapter 9 contains the conclusions drawn from the data obtained and their relevance with regards to the objectives set out above. This section includes the importance of the results obtained throughout this research and the sets up the scope for potential future work.

Chapter 2

Background

Since the 1893 Arthur Conan Doyle short story entitled "The Adventure of the Gloria Scott" the term "smoking gun" has been used to describe the strongest kind of circumstantial evidence (Panko B., 2017). Since then, the term "smoking gun" has gained increasing popularity, and became part of the American lexicon after the Watergate crisis in July 1974, when members of Congress were asking "Where's the smoking gun?" when considering the impeachment of President Richard Nixon. However, what is the smoke that comes out the barrel of a firearm, and why is it so important? The obvious answer here may be "because it indicates that the gun was just fired", but actually, that 'smoke' contains valuable evidence that can be analysed as part of a shooting investigation, known as GSR.

2.1 What is GSR?

Gunshot residue (GSR), also known as firearm discharge residue (FDR) (Flynn J. et al. (1998); Wallace J.S. (2008)) and cartridge discharge residue (CDR) (Wallace J.S. & McQuillan J., 1984), are particles that are produced when a cartridge-based weapon is discharged. Upon firing, burnt and unburnt particles are expelled from the muzzle. These particles primarily originate from the primer and propellant, but can also contain residues from the bullet, cartridge (Matty W. (1987); Bydal B.A. (1990); Wallace J.S.

(1990)), material in the barrel from previous firings or cleaning and lubrication, as well as traces from the firearm itself (Romolo F.S. & Margot P. (2001); Morales E.B. & Vasquez A.L.R. (2004)). As these particulates fly through the air, they mix with other discharged gases and vapours, and rapidly condense into droplets prior to solidifying into GSR particles (Basu S., 1982).

2.1.1 Identifying GSR

Due to the multiple constituents present in the ammunition, GSR consists of both organic and inorganic components. The propellant and firearm lubricants are the primary source of the organic GSR material (OGSR), and form unburnt and partially burnt gunpowder particles and hydrocarbons (Dalby O. et al., 2010). Conversely, the inorganic residues, such as metallic particles and nitrates, originate from both the primer and propellant, as well as the ammunition components (i.e. cartridge case, projectile jacket and core, as well as the firearm barrel itself) (Brożek-Mucha Z., 2007). However, it is the inorganic particles that are of particular interest as they form the formally recognised, 'characteristic' GSR (Wolten G.M. et al., 1977), as shown in Table 2.1, and Table 2.2 using the formally recognised American Society for Testing and Materials (ASTM) guidelines (American Society for Testing Materials, 2017). The ASTM guidelines get reviewed and updated periodically, so it is important to be aware of the newest standard practice and classification changes when undertaking GSR analyses.

Table 2.1: Table showing the GSR classifications designated by Wolten G.M. et al. (1977). 'Characteristic' elemental compositions have been observed only in gunshot residue, whereas 'consistent' compositions are consistent with GSR, but not unique.

Characteristic	Consistent
Pb, Sb, Ba	Pb, Sb
	Pb, Ba
Ba, Ca, Si, with a trace of S	Pb
	Ba if S is absent or only a trace
Sb, Ba	Sb (rare)

The classification system introduced by Wolten G.M. et al. (1977) (Table 2.1) came as a result of extensive firearm and ammunition tests. Following on from this work, Basu S. (1982) expanded the inorganic GSR classifications to incorporate internal particle composition (Table 2.3), and Wallace J.S. & McQuillan J. (1984) modified the original classification system discussed by Wolten G.M. et al. (1977) to that shown in Table 2.4.

Table 2.2: Table showing the GSR classifications designated by American Society for Testing Materials (2017). 'Characteristic' elemental compositions have been observed only in gunshot residue, whereas 'consistent' compositions are consistent with GSR, but not unique.

Characteristic	Consistent
Pb, Sb, Ba	Pb, Ba, Ca, Si Ba, Ca, Si Sb, Ba Pb, Sb Ba, Al Pb, Ba

In Table 2.4, 'unique' and 'indicative' are the equivalent of 'characteristic' and 'consistent' described by Wolten G.M. et al. (1977) (2.1). Furthermore, with regards to Table 2.4, *Major* level refers to any element whose main peak height is greater than one-third of the peak height of the strongest peak in the EDX spectrum, *Minor* level refers to any element whose main peak height is between one-tenth and one-third of the peak height of the strongest peak in the spectrum, and *Trace* levels correspond to any element whose main peak height is less than one-tenth of the peak height of the strongest peak.

Table 2.3: Table showing the GSR classifications based on the distribution of lead, antimony and barium in GSR cross-sections by Basu S. (1982).

Category	Type of Element Distribution
I	Uniform and concurrent (Pb, Sb, Ba)
II	Inhomogeneous and discontinuous distribution or both (Pb, Sb, Ba)
III	Distribution in layers (Pb around a Ba and Sb core)

In order for a particle to be considered to have originated from a firearm, and therefore be classified as GSR, there are two primary criteria that need to be fulfilled. Firstly, the particle must be of a spheroidal morphology. Previous research has shown that GSR particles are 70 - 100 % spheroidal, with occasional irregular particles also being observed (Wolten G.M. et al. (1977); Wallace J.S. (2008)). The second criterion for the identification of GSR is a discriminatory elemental composition of lead, antimony and barium. This elemental composition is not exclusive to GSR. In fact, residues produced upon the ignition of fireworks, and brake dust released during air bag deployment in the course of a motor vehicle collision, can produce particles of the same elemental composition, but of irregular morphologies (Wolten G. et al. (1979a);

Table 2.4: Table showing the GSR classifications modified by Wallace J.S. & McQuillan J. (1984), where the indicative particles are listed in the approximate order of decreasing significance.

Unique	Indicative
Pb, Sb, Ba	Ba, Ca and Si [1]
	Pb, Sb
Sb, Ba	Pb, Ba
	Sb (with S)
	Sb (without S)
	Ba [1]
	Pb
	Pb, Sb and Ba absent [2, 3]

[1] S absent or acceptable as trace only when Ba is present at a major level.

[2] Any of the above may also include some, or all, of the following: Al, Ca, S, Si at major, minor or trace level; Cl, Cu, Fe, K, Zn (only if Cu also present and Zn : Cu < 1) at minor or trace level; Mg, Na, P at trace level only.

[3] Particles containing no Pb, Sb or Ba may be considered indicative if they are composed entirely of the elements in '2' above and are accompanied by other types of indicative particles.

Wallace J.S. & McQuillan J. (1984), Garofano L. et al. (1999)). Despite the similar compositions between these particles, elemental compositions can be used to discern between GSR and non-GSR particles even if spheroidal morphologies are observed. For example, residues originating from vehicle brake mechanics contain additional elements that are not ordinarily associated, or encountered, with GSR, such as iron, zinc, phosphorus, bromine, chlorine and chromium (Wolten G.M. et al., 1977). These elemental composition combinations are not observed with GSR, but are highly characteristic of vehicle exhaust and gasoline residues (Wolten G.M. et al. (1977); Romolo F.S. & Margot P. (2001)). However, by considering both the elemental composition as well as the morphology of individual residues, GSR particles can be successfully identified from an array of aggregate particles.

The organic compounds that contribute to the formation of OGSR are predominantly attributed to the propellant powder and primer mixture, but may also originate from other parts of the ammunition used (Meng H.H. & Caddy B., 1997). However, OGSR consist of compounds whose use is not limited to the manufacture of ammunition, and are often too volatile to withstand recovery and analytical procedures (Persin B et al. (2007); Weyermann C. et al. (2009)). Consequently, special emphasis was placed in the analysis of the metallic, inorganic residues that have been shown to persist and be identified in samples years after they have been collected, and is the primary focus of this thesis. These metallic particles must be spheroidal and consist of three

distinct elements - lead (Pb), antimony (Sb) and barium (Ba), as mentioned previously (Wolten G.M. et al., 1977). Once these criteria have both been met, and a particle is spheroidal with the aforementioned elemental composition, a particle can be assumed to have been produced during the discharge of a firearm and can therefore be classified as 'characteristic' GSR. This thesis focuses on the identification and analysis of these residues, i.e. inorganic GSR.

2.2 Ammunition Components & Types

The modern, self-contained metallic cartridge was perfected approximately 134 years ago, with high-velocity, smokeless powder types not being developed until about 20 years later (Barnes F.C., 1976). Rim-fire cartridges, i.e. cartridges with a hollow rim to contain the primer in, were patented in 1846 by Houllier and developed by Flobert (Wallace J.S., 2008). However, it was Smith & Wesson who developed the design to hold a charge of gunpowder, which went on to become very popular as a number of rim-fire cartridges could be housed in a firearm's magazine.

After the development of the rim-fire cartridge, and subsequent firearm evolution, smaller ammunition with greater power and range were sought after. However, the thin metal base of the rim-fire cartridge could not withstand the higher pressures required, nor could it hold the increased amount of primer that would be required (Wallace J.S., 2008). This led to the development of the centre-fire cartridge, that was originally produced in 1808 but was perfected and patented by Smith & Wesson in 1854. The primary structural difference between a rim-fire and centre-fire cartridge is that centre-fire cartridges use primer caps to house the priming mixture in the centre of the cartridge case base, rather than on the rim (Rinker R.A., 2005). The differences between the three types of cartridges used (or modified) throughout this thesis can be seen in Figure 2.1.

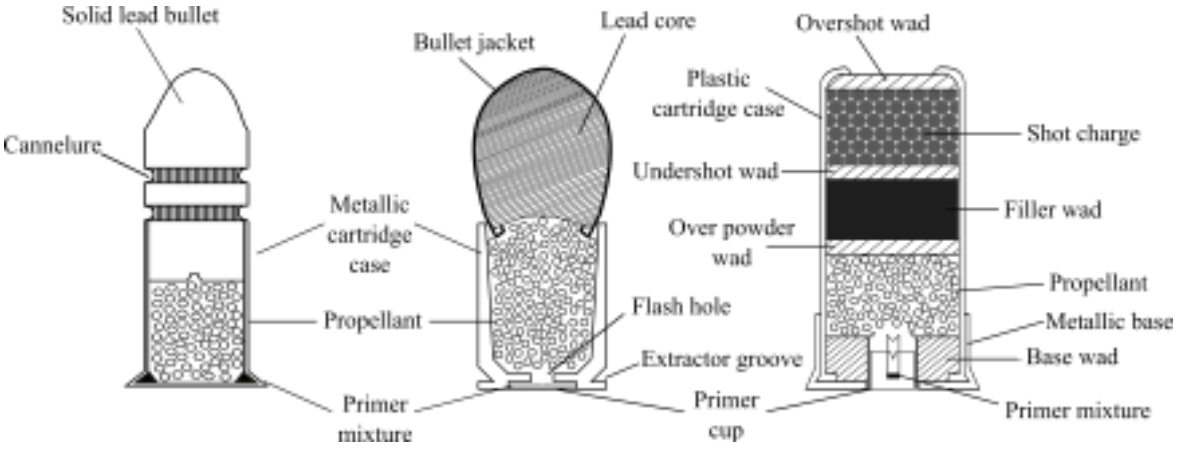

Figure 2.1: Schematic (not to scale) of the three main ammunition types used in this thesis. Left: rim-fire cartridge, middle: centre-fire cartridge, right: shotgun cartridge.

The production of jacketed bullets, whether semi-jacketed or full metal jacketed (FMJ) were important in the development of firearm projectiles. Previously, unjacketed lead bullets were unsuitable for higher-velocity firearms due to deformation of the lead projectile due to air friction, affecting accuracy and limiting unjacketed projectile use to $\sim 365\,\mathrm{m\,s^{-1}}$ (Wallace J.S., 2008). By adding a jacket to the projectile the twist rate can be substantially increased, thereby increasing the projectile velocity, which was previously hindered by the lead projectile deformation. Bullet jackets have been known to have been made of cupronickel (80% copper, 20% nickel) or gilding metal (90 - 95% copper, 10 - 5% zinc) amongst others (Wallace J.S., 2008), with the vast majority of modern bullet types being jacketed to some extent (whether fully or partially) with gilding metal.

Priming compositions (also referred to as primers) are mixtures that cause a sudden burst of flame when subjected to percussion, igniting the propellant. It is the subsequent ignition and combustion of the propellant that pushes the projectile down the barrel of the firearm. Therefore, primers have to be able to deliver a large volume of hot gases and solid particles without developing a detonating wave (Wallace J.S., 2008). This is achieved by creating a mixture of compounds that, although individually may not be explosive, as part of a mixture sensitize each other to ignition and rapid burning. These compounds are called sensitizers and binders, and essentially make primer compounds into high explosives that are sensitive enough to explode when struck by the firing pin (Meng H.H. & Lee H.C., 2007).

Small arms primers usually consist of four main components - the initiator, an oxidizer, a fuel and a frictionator (Wallace J.S., 2008). In modern primers, the initiator, which is essentially an explosive, consists of lead styphnate. Oxidizers consist of

barium nitrate and are used to increase the heat of ignition, and antimony sulphide is a commonly used fuel (Harrison H.C. & Gilroy R. (1959); Meng H.H. & Lee H.C. (2007)). Interestingly, antimony sulphide can also act as a frictionator, which is used to sensitize the mixture to percussion (Wallace J.S., 2008). From this, it can be seen where some of the elements responsible for the formation of GSR could originate. However, it is important to note that although these are popular primer mixtures, specific compositions vary depending on manufacturers' secret primer recipe modifications.

As this thesis focuses on the formation and analysis of inorganic GSR, little emphasis is placed on the development and research of OGSR. However, in the interest of understanding how firearm ammunition works as a whole, information on modern propellants is provided below.

In 1250, Roger Bacon produced the first (recorded) European firearm propellant recipe for black powder (Warlow T.A., 1996). Black powder was typically composed of 75% potassium nitrate, 10% sulphur and 15% charcoal (Meng H.H. & Caddy B. (1997); Wallace J.S. (1990)), but has since been replaced by smokeless powders. Smokeless powders can be categorised into single, double and triple base powders. Single base powders primarily use nitrocellulose as an explosive, double base powders use both nitrocellulose and nitroglycerine, and part of the nitrocellulose and nitroglycerine is replaced by nitroguanidine in triple base powders (Dalby O. et al. (2010); Meng H.H. & Caddy B. (1997)).

Smokeless powders make up the propellant, which in small arms ammunition is defined as "explosive materials which are formulated, designed, manufactured, and initiated in such a manner as to permit the generation of large volumes of hot gases at highly controlled, predetermined rates" (Kirk-Othmer R.E., 2000). Propellants need to be stable, easy to store and ignite, but still of a small enough size to fit in the primer cap, while at the same time being cheap to produce and contain its own oxygen supply, as combustion occurs in a confined space (Wallace J.S., 2008). Unsurprisingly, there is no single chemical compound that can fulfil all the requirements, so mixtures are used here as well.

The burning rate of the propellant is also an important factor to be considered, as if hot gases are released too quickly the propellant would detonate, causing injury and/or firearm damage. Conversely, if the propellant burns too slowly, it will be inefficient and not provide the bullet with sufficient velocity before exiting the muzzle (Rinker R.A., 2005). However, this can be controlled by the size and shape of the individual propellant granules (Wallace J.S., 2008), although the relationship between physical shape and burn rate is complex and dependent on many other factors, such as the characteristics of propellant surfaces and associated decomposition rates.

So, what happens when a firearm is discharged? Firstly, once the trigger is pulled, a spring mechanism hammers the metallic firing pin into the base of the cartridge. This rapidly ignites the primer, which in turn ignites the main explosive, i.e. the propellant. As the propellant mixture burns, it quickly generates gases that cause a sudden increase in pressure. This high pressure pushes the bullet out of the cartridge, forcing it down the barrel of the firearm at speeds $> 300\,\mathrm{m\,s^{-1}}$ (Woodford C. (2006/2018); Rinker R.A. (2005)). As the projectile leaves the muzzle, the hot plume comprising of discharge gases and particles (that ultimately form GSR and OGSR) are expelled from the barrel, while the cartridge remains in place and is ejected after firing.

2.3 Modern methods in GSR detection and analysis

Scanning Electron Microscopy with Energy Dispersive X-ray spectroscopy has been the primary analytical tool used in the analysis of GSR since it was first used for this purpose in 1968, as reported by Heard B.J. (1997) (Wolten G.M. et al. (1977); Dalby O. et al. (2010)). However, the ability for GSR to provide investigative leads is limited (Meng H.H. & Caddy B., 1997).

The detection and identification of GSR primarily pertains to determining whether a firearm has been discharged by a suspect, to ascertain a bullet hole entrance, or to estimate a firing distance (Lichtenberg W. (1990); Sellier K. (1991)). The evidential value of GSR has always been questioned as there has been some uncertainty as to how much GSR evidence, i.e. how many GSR particles found, is enough? In some laboratories, a minimum of two confirmed GSR particles are required (along with associated or indicative particles) to be considered the lowest limit for a positive result (Heard B.J., 2013). Case studies, such as the case of Jill Dando in 1999, have shown the difficulty in interpreting GSR evidence, as the suspect was initially convicted due to a single GSR particle found on their clothing, before being acquitted following two appeals. As a result of this ambiguity in interpreting evidence, probabilistic statistics have been developed to determine the likelihood that the observed GSR particles on a suspect are, or are not, as a result of being involved in a shooting (Biedermann A. et al. (2009); Biedermann A. et al. (2011)). However, a significant number of particles is required to perform reliable statistical analyses, which can often prove difficult due to the nature of GSR evidence.

As the identification of particles is incredibly time consuming due to the number of

residues that require analysis, automated analyses using SEM-EDX have been developed to assist with the particle identification of GSR. Computer-controlled analytical SEM parameters such as the minimum particle size, video threshold, digital electron beam point spacing, video dwell time, X-ray counting time, and analysis mode, affect the time and accuracy of automated GSR particle analysis (Germani M.S., 1991a). This often leads to inconsistency when it comes to reproducibility as some parameters cannot be controlled during a long run (such as SEM filament emission current and beam drift), and the settings required for successful automated analyses are fairly precise. Therefore, custom-written software has previously been employed over commercial packages (Germani M.S., 1991a) to develop standard procedures for the automated SEM/EDX GSR analyses.

Although automated techniques for the identification and analysis of GSR using SEM/EDX have been developed, there are still questions as to the reliability of such software. As a result, a significant amount of time is required to manually check the results produced and exclude any misidentified particles (see Chapter 4 for automated analyses using the automated INCA GSR software), with challenges moving from the analytical domain to the interpretation of the analytical results (Maitre M. et al., 2017).

Algorithms have recently been developed to improve the initial classification part of automated software (Mandel M. et al., 2018), and have been proven to reduce the time taken to analyse GSR data. Maitre M. et al. (2017) have demonstrated that GSR analyses are moving from the analytical domain to the interpretation of the analytical results, with the Bayesian network using a case-by-case approach, allowing for the evaluation of evidence with respect to activity-related questions, similar to those discussed by Biedermann A. et al. (2009) and Biedermann A. et al. (2011). This approach allows an evaluation of the evidence that is more closely aligned to judicial and investigative aims, however the introduction of lead-free ammunition will result in the types of particles traditionally used to identify GSR being absent (Maitre M. et al., 2017). Lead-free ammunition was produced to work in the same way as conventional ammunition but without producing a toxic product on discharge, i.e. lead. This lead to the production of the "lead-free" Sintox primers which were free of lead, antimony and barium, but rather consist of a totally jacketed bullet, diazodinitrophenol and tetracene as the 'explosive' ingredients, zinc peroxide as the oxidizer, titanium metal powder and nitrocellulose as the propellant powder (Gunaratnam L. & Himberg K., 1994).

GSR can provide important clues in recreating a shooting scene. Inorganic GSR is primarily used as an investigatory aide due to its discriminatory morphology and elemental composition, and has previously been used to determine the distance between

the shooter and target in question (Turillazi E. et al (2013); Brożek-Mucha Z. (2009); Fojtasek L. et al. (2003)). However, in court, GSR evidence is considered to be an investigatory tool that is used to corroborate or refute a narrative (Vachon C.R. & Martinez M.V., 2019). This demonstrates that the many aspects of GSR and its analysis as part of a criminal investigation, can only be utilized if the interpretation (and limitations) of GSR evidence is understood. Current research focuses on OGSR detection through the development of different analytical techniques (Dalby O. et al. (2010); Goudsmits E. et al. (2015); Romano S. et al. (2020); Dalby O. & Birkett J.W. (2010)), but a consistently reliable and efficient method for the analysis of OGSR has not been developed. However, when complemented by inorganic GSR analyses, the evidentiary value of GSR strengthens (Goudsmits E. et al., 2019) as the 'characteristic' elements associated with GSR can be identified. Often, multiple perspectives will come together to tell an overarching story. Similarly, GSR evidence should be used as an additional perspective that is useful in interpreting a larger evidential puzzle.

The next chapter describes some of the state-of-the-art instrumentation that was used in this thesis to perform these sorts of analyses.

Chapter 3

Materials & Instrumentation

The equipment and instrumentation used for sample acquisition and analysis are presented in this section. Scanning Electron Microscopy with Energy Dispersive X-ray Spectroscopy was the primary analytical technique that was used to analyse samples, whereas the light gas gun was used to produce an array of samples investigating in-flight cooling and impact melting, discussed in Chapter 7. Raman spectrometry was also used for part of the analyses and is also included in this section.

3.1 Scanning Electron Microscopy & Energy Dispersive X-ray Spectroscopy

Scanning Electron Microscopy with Energy Dispersive X-ray Spectroscopy was the primary technique used throughout this thesis. The ability to acquire information on both the morphological and elemental composition data, as well as the fact that this is a (mostly) non-destructive technique makes this an invaluable tool for inorganic GSR analyses. The two Scanning Electron Microscopes available at the University of Kent were used with their respective detectors: SEM/EDX refers to the Hitachi 3400N Scanning Electron Microscope with an Oxford Instruments 80 mm^2 *X-max* Energy Dispersive X-ray Spectrometer, whereas FEG-SEM/EDX refers to a Hitachi 4700 cold

field emission Scanning Electron Microscope with a Bruker *X-flash* Energy Dispersive X-ray Spectrometer.

3.1.1 Background

Since the development of the high resolution Scanning Electron Microscope (SEM) in 1937 (von Ardenne M., 1938), the observation and characterization of organic and inorganic materials has been made possible on a micrometre to nanometre scale (Goldstein J. et al., 2003). SEMs employ the use of a finely converged electron beam to scan a sample surface, providing information on the surface topography of a sample. SEMs have a depth of field over 200 times greater than an optical microscope (Romolo F.S. & Margot P., 2001), and can also be used to determine the elemental compositions of samples, when used in conjunction with Energy Dispersive X-ray spectroscopy (EDX).

Due to the information that SEM/EDX can provide with respects to both morphological and compositional sample data, SEMs have been used in a variety of disciplines. These range from identifying ancient Greek artefacts (Kylafi M. et al., 2017), to analysing residues contained within micron-scale craters in aluminium foil returned from NASA's "Stardust" mission (e.g. Stroud R.M. et al (2013)), and to correlate fluorescent proteins to cellular structures (Peddie C.J. et al., 2017).

The earliest research into the use of SEM/EDX for GSR analyses were reported in 1968 by the Metropolitan Police Forensic Laboratory, New Scotland Yard in England (Heard B.J., 1997), and soon after, in 1971, Boehm E. (1971) presented micro-graphs of GSR particles from "gun smoke deposits" around entrance gunshot wounds. These results generated interest, and a symposium on particulate GSR was held at The Aerospace Corporation in 1975, with Nesbitt R.S. et al. (1976) presenting a paper on GSR detection using SEM analyses in 1976. However, the most extensive work on the use of SEM/EDX for GSR analyses was carried out by Wolten G. et al. (1979b), where the characterisation and classification of GSR particles based on their elemental compositions was presented.

The use of SEM/EDX in sample analysis comes with many advantages. Firstly, SEM/EDX analyses are mostly non-destructive, which is particularly important when dealing with GSR evidence and other 'precious' samples. There is also very little sample preparation that is required prior to analysis. However, the most significant advantage of SEM/EDX analyses is that both images and compositional data can be acquired from the same area within a sample. This ability has made SEM/EDX the chosen technique for the identification of inorganic GSR particles, as both of the discriminating factors of GSR (spheroidal morphology and specific elemental composition) can be determined simultaneously.

3.1.2 SEM Fundamentals

There are two ways in which accelerated electrons from the electron beam interact with samples. Firstly, if the incident beam electrons are deflected off the specimen, they are referred to as backscatter electrons (BSE). Conversely, if the electrons from the incident beam dislodge electrons from the specimen, the ejected electrons are referred to as secondary electrons (SE). Elemental data can also be acquired when electrons in the sample are dislodged, but are replenished by electrons in the outer shells of the atom in the sample, generating X-rays of an energy characteristic to that element.

Images produced using BSE can show the relative composition of the sample as heavier elements appear brighter as they generate more BSE, and less dense elements appear dark. The nuclei of atoms within the sample deflect the incident electrons as they pass through the sample, and the angle of deflection, γ, is determined using Equation 3.1 (Reed S.J.B., 2005).

$$\tan\left(\frac{\gamma}{2}\right) = Z\,(1.4\rho E) \tag{3.1}$$

where,
Z = atomic weight,
ρ = minimum distance from the electron's unaltered path to the nucleus (nm)
E = energy of deflected electron (kV).

If an electron from the electron beam is deflected back at an angle which is greater than 90°, it is referred to as backscattered (Reed S.J.B., 2005). Elements with a higher Z value, and therefore heavier nuclei, are more likely to deflect electrons at angles greater than 90°, due to the increased number of electron shells making beam-electron and atomic-electron interactions more likely.

SEs are electrons that were originally part of the atoms in the sample but were dislodged by the incident beam. They generally tend to come from an area near the surface of the particle, and so provide higher resolution images or the sample topography (Vernon-Parry K.D., 2000). SEs have a lower energy than BSEs (Reed S.J.B., 2005), which assists in demonstrating a particle's surface morphology.

X-rays can be produced as a result of the interaction between beam electrons and a sample. These X-rays can either be continuous or characteristic (Reed S.J.B., 2005). The former are produced when an incident electron emits an X-ray photon as it drops to a lower energy state, due to its proximity to an atomic nucleus in a sample (Reed S.J.B., 2005). The X-rays produce a constant 'background' (Bremsstrahlung) that is detected using an EDX detector (Reed S.J.B. (2005); Zhou et al. (2007)). The latter type of X-rays are produced when an incident beam dislodges an electron from an

orbiting shells within an atom, which is then replaced by an outer shell electron. This results in an X-ray photon to be emitted, the energy of which depends on the element and electron shell that the replacement electron came from. The continuous X-rays produce the Bremsstrahlung background whereas the characteristic X-rays appear as peaks at the element-specific energies. Different elements will have multiple peaks as they show the transition of electrons from one shell to another (i.e. K_α, K_β, L_α, L_β, M_α or M_β), where each peak label indicates the initial shell from which the electron was knocked out.

3.1.3 SEM Construction

Figure 3.1 shows a schematic of an SEM which has four main components, an electron gun, an electron column, a specimen chamber and a computer output.

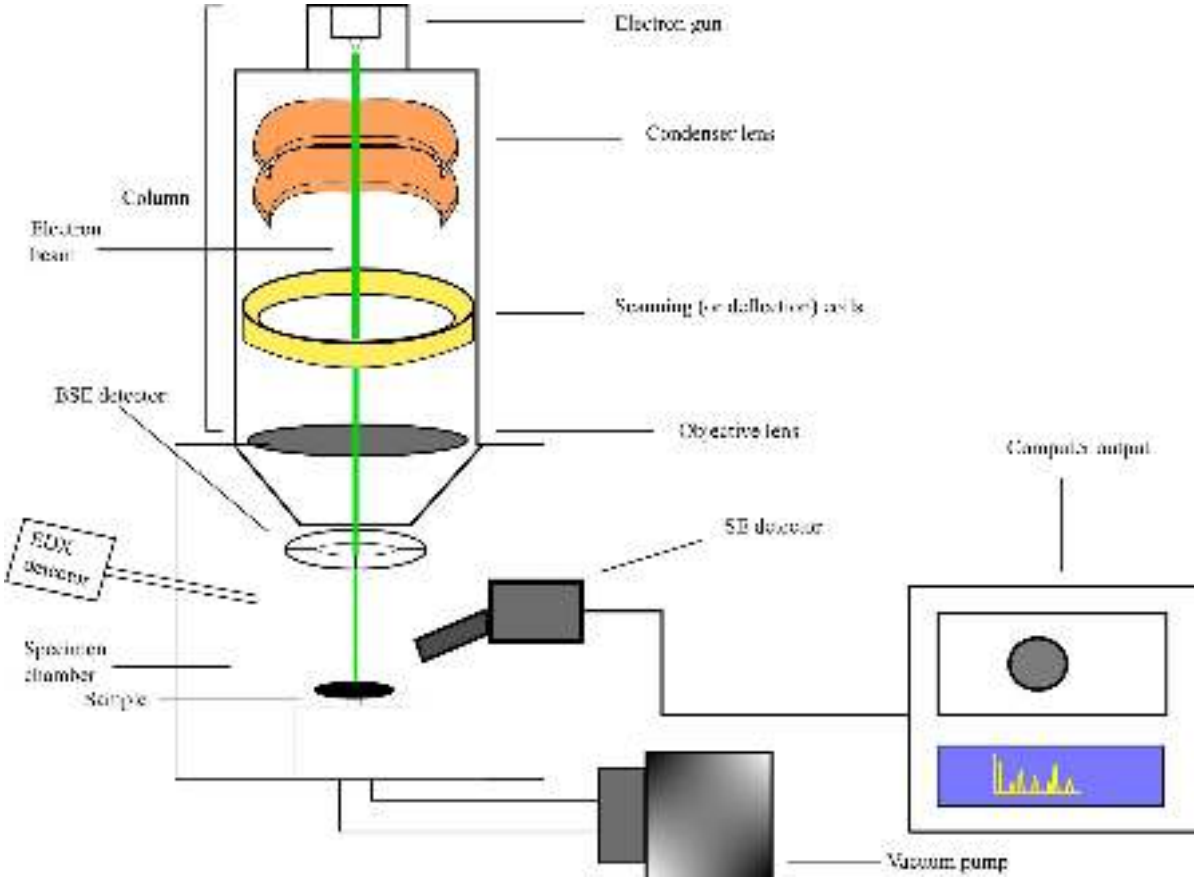

Figure 3.1: Schematic (not to scale) of the SEM/EDX used at the University of Kent.

The electron gun is used to emit electrons. This is often a tungsten wire/filament that is bent into a "V"-shape (SEM). The FEG-SEM at the University of Kent has a cold field emission gun which consists of a fine, sharp, single crystal tungsten tip.

This gives a more coherent beam, where electrons are emitted from a small area of a few nanometres (rather than micrometres), greatly improving the image quality. For wire/filament sources, at high temperatures, electrons in the filament have sufficient energy to be emitted from the source by thermionic emission (Goldstein J. et al., 1981). The "V"-shape of the filament assists in directing the electron beam through the aperture below the filament, and down the column. The penetration depth that the electron beam reaches on a solid sample, depending on the beam voltage, can be determined using the Vernon-Parry K.D. (1972) penetration depth equation:

$$R_{\mathrm{KO}} = \frac{0.0276A}{Z^{0.89}\rho} {E_0}^{1.67} \tag{3.2}$$

where,
A = atomic weight (g/mol)
Z = atomic number
ρ = density (g/cm^3)
$\mathrm{E_0}$ = beam energy (kV)
$\mathrm{R_{KO}}$ = calculated in µm.

Therefore, by using Equation 3.2, the penetration depths for lead using different kV can be determined (Figure 3.2). As it can be seen, the maximum penetration depth for lead would be 1.49 µm using 20 kV. However, 10 kV was primarily used throughout this thesis, indicating a beam penetration depth of 0.47 µm.

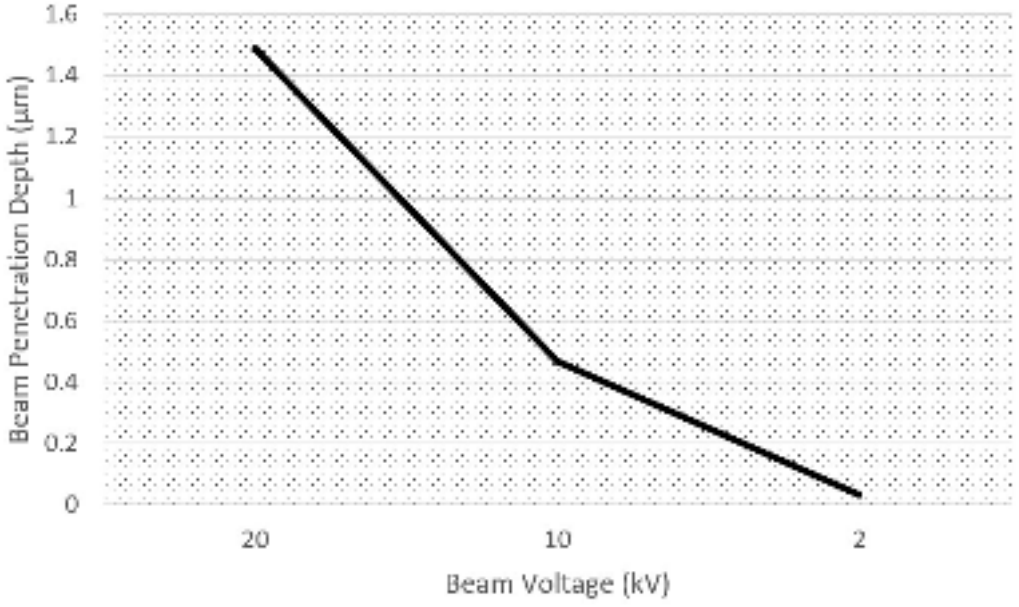

Figure 3.2: Graph showing the different penetration depths for a lead sample using Vernon-Parry K.D. (1972), Equation 3.2.

In the column, condenser lenses, made of coiled copper wire encased in an iron casing, are used to focus the electron beam as it travels down the column (Goldstein J. et al., 1981). A magnetic field is created when a current is passed through the copper wire, which can deflect the electron beam along the centre of the column (Reed S.J.B., 2005). Scanning (or deflection) coils are used to raster the beam over the sample. A difference in potential across the coils is created which can change the angle of the electron beam along the x and y axes (Zhou et al., 2007).

The objective lens is the final lens in the electron column, which uses an electromagnet to generate a magnetic field. This is used to focus the electron beam, similar to the condenser coils, before it reaches the specimen chamber.

The specimen chamber houses the three main detectors - an SE detector, a BSE detector and an EDX detector- and is normally kept under vacuum, except during sample exchange. A scintillator is used to detect SEs from the sample by converting electron strikes into flashes of light, after which a photomultiplier converts them to electrical signals (Reed S.J.B. (2005); Zhou et al. (2007)). A solid state detector (typically a silicon crystal) composed of four different segments with a hole in the centre for the electron beam to pass through is used to detect BSEs (see Chapter 4, Figure 4.5). The individual segments can be switched off independently, allowing for topographical information to also be generated from BSE (Reed S.J.B., 2005). EDX detectors convert X-ray photons into an electrical pulse. When an X-ray photon (or electron) interacts with a crystal of high purity, such as silicon or germanium, a small current is generated. The intensity of this current then provides information about the energy of the incoming X-ray, which can be used to discern a sample's elemental composition.

Finally, a computer output is used to control the set-up, including the magnification, stage movement and detector used, and displays the final images and spectra acquired.

3.1.4 Limitations

Although the use of SEM/EDX provides useful data, there are some limitations that can affect sample analysis. Firstly, there is the charge-up phenomenon (or "charging") that is observed in non-conductive samples. Charging can appear as uneven bright lines on a sample under SEM conditions, which leads to images appearing distorted during acquisition. This occurs due to the incoming electron flow from the electron beam onto the sample. If a sample is conductive, the incoming electron flow is complemented by an outgoing electron flow. However, when the sample is non-conductive, there is little outgoing electron flow, causing a cluster of electrons to remain on the sample surface, causing the charge-up phenomenon (Hitachi, 2013). Therefore, to prevent the

charge accumulation from happening, the remaining beam current has to flow from the specimen to the ground (Kirchoff's current law). The balance of the currents for a non-charging junction is given by Goldstein J. et al. (2018):

$$\sum i_{\text{in}} = \sum i_{\text{out}} \tag{3.3}$$

$$i_{\text{B}} = i_{\text{BSE}} + i_{\text{SE}} + i_{\text{SC}}$$

where,

i_{B} = beam current (nA)

i_{BSE} = current flowing out of the BSE junction as a result of the back-scattering of beam electrons (nA)

i_{SE} = current flowing out of the SE junction due to secondary electron emission (nA)

i_{SC} = the specimen current (nA).

There are several ways to counteract the charge-up phenomenon. Integrating multiple superimposed, rapid scan images can reduce the appearance of charging in the acquired images, but often this is not sufficient. The first technique that can be employed is the reduction of the accelerating voltage and/or the electron beam current. By reducing one (or both) of these parameters, the flow of electrons irradiating the sample is reduced, thereby diminishing the number of electrons available to cluster on the sample surface. Another technique used to counteract the charge-up phenomenon is the use of a metal coating, which was employed in Chapter 4, or carbon coating, which is often employed in GSR analyses. The use of a thin coating (such as C, Au or Pt) increases the sample's surface electrical conductivity, thereby enabling electrons to flow away from the surface of the sample. This can also be achieved through the use of metallic tape, such as copper. Finally, the BSE Variable Pressure (BSE-VP) operation mode can be used to prevent sample charging. The BSE-VP operation mode allows for the vacuum inside the specimen chamber to be controlled by letting in small amounts of air, which can carry away the excess electrons sitting on the sample surface. However, as the air that was leaked in to create the variable pressure can block some of the X-rays and cause electron scatter, the X-ray count rate drops, which can lead to smaller peaks going by undetected and an increase in X-rays detected from surfaces away from the sample. Additionally, only BSE imaging can be used and, when using BSE-VP mode, the atmosphere can cause beam scattering which can result in X-rays from places other than the intended location (e.g. the chamber or stub).

A significant disadvantage in the use of SEM for the detection of GSR particles is

that an excessive amount of time is required to search for, and locate, the particles of interest. This is due to the large sample area, the time spent examining, analysing and rejecting a large number of non-GSR particles, and the extraneous material (such as fibres and skin debris) which can make particles difficult to find, or conceal, them altogether (Romolo F.S. & Margot P., 2001). However, a range of automated GSR detection systems have been developed, using custom-written or commercial software, which can analyse and reject non-GSR particles, reducing the time spent examining a given sample area (Germani M.S. (1991b); Kee T.G. & Beck C. (1987); Tillman L. (1987); White R.S. & Owens D.A. (1987)). The choice of detector can be important when it comes to automated analyses due to shadowing. Detectors are often inclined to the side (such as with the Oxford Instruments' detectors) which can cause partial shadowing on particles. This can interfere with elemental identification and, as a consequence, particle classification. However, Bruker's *X-flash* detector sits around the pole piece on top of the sample, preventing shadowing and allowing a higher number of X-rays to be detected.

Despite these small disadvantages, SEM/EDX is still the 'go-to' instrument for inorganic GSR analyses.

3.2 Raman Spectrometry

Raman spectrometry is a minimally-invasive analytical technique that has been used in various scientific fields, such as forensic science (Salahioglu F. et al., 2013), radiopharmaceuticals (Brown O. et al., 2017), materials science (Das R.S. & Agrawal Y.K., 2011) and geology (McMillan P.F., 1989). With no sample preparation being required and the quick identification of samples, Raman spectrometry is generally a non-destructive technique which is often used for the analysis of organic samples. This made this analytical technique ideal to investigate any organic variations in GSR particles without destroying the sample.

3.2.1 Background

Raman spectrometry is a vibrational spectroscopy that examines molecular vibrations between the various atoms within the molecules of a sample, and it is these molecular vibrations that cause the scattering of light. A monochromatic light source is used to irradiate a sample, which affects the energy a molecule has. The incident photons cause the molecules' electron cloud to distort and thus vibrate, which results in the inelastic

scattering of light to different wavelengths. Raman scattering is caused when 0.0001% of light is inelastically scattered by the interaction between the incident light and the molecule, whereas the remaining 99.9999% of light is elastically scattered, known as Rayleigh scattering. A spectrum is acquired by plotting the difference in wavelength between the incident and scattered light as a function of intensity, where each peak represents a vibrational mode of a specific bond. By considering the relationship between energy and wavelength (Equation 3.4), the wavelength of the scattered light can be determined. This, in turn, determines if the light has been elastically or inelastically scattered (Rayleigh and Raman scattering respectively).

$$E_{\mathrm{p}} = \frac{hc}{\lambda} \tag{3.4}$$

where,
$\mathrm{E_p}$ = energy of the photon (J)
h = Planck's constant (6.62607×10^{-34} $\mathrm{J\,s^{-1}}$)
c = speed of light in a vacuum (2.998×10^{8} $\mathrm{m\,s^{-1}}$)
λ = wavelength (m).

If the bond within a simple two atom molecule is considered as a spring, the resulting oscillation produces harmonic motion over time, where both atoms are vibrating at the same frequency (Larkin P.J., 2011). The vibrational frequency of the bond is determined by the mass of the individual atoms and bond strength, with the vibration resulting in the molecule gaining energy that is proportional to the frequency. The natural frequency that the molecule vibrates at is the fixed frequency of shift that occurs when light is re-emitted. This means that for Raman shifted light the change in frequency is the same as the natural vibration of the bonded atoms.

The energy required for the oscillations within the molecule to occur comes as a result of incoming photos from the incident light that are absorbed by the molecule. This additional energy promotes an electron to a higher energy state, but the molecule can emit a photon when the electron relaxes back to a lower energy level. If the wavelength of the emitted light is different to that of the incident light, Raman scattering has occurred. If the scattered light has an energy that is less than the incident light, Stokes scattering occurs. Conversely, if the energy of the scattered light is greater than that of the incident light, anti-Stokes scattering occurs (Figure 3.3). Stokes scattering is considered the 'normal' type of Raman scattering, where the electron gains energy, exciting it from the ground energy level to a virtual electronic energy level, and then relaxes and falls to a higher energy level than it originally stated with.

Anti-Stokes scattering occurs when the electron is already at a higher energy level

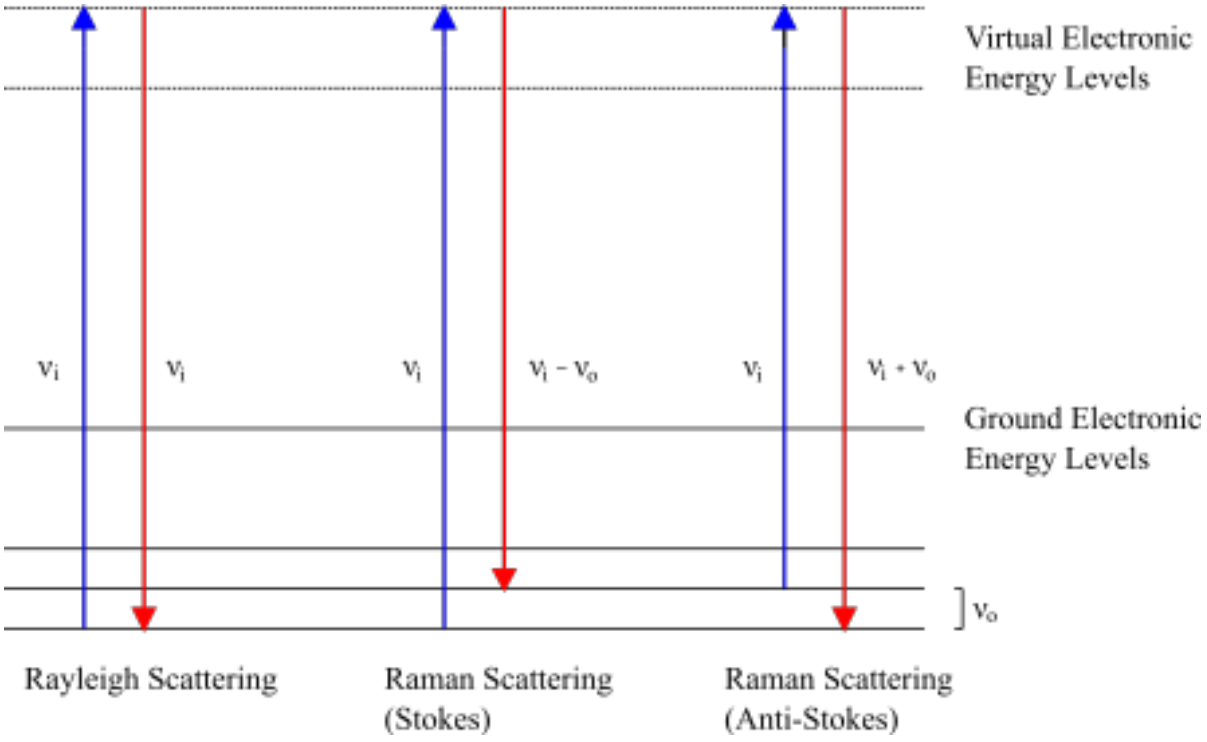

Figure 3.3: Energy level diagram showing the difference between Rayleigh scattering and the two types of Raman scattering.

before being excited to a higher energy level, and when it relaxes, it returns to an energy level lower than its starting energy level. This requires the electron to be at a higher energy level than the ground state, which occurs when some energy has already been absorbed by molecules from the environment (i.e. at increased temperature). By comparison, the number of photons experiencing Stokes shift are greater than those undergoing anti-Stokes shift. This is because fewer electrons are in higher electronic energy levels (rather than at ground state) when the sample is in thermal equilibrium at room temperature (Pask H.M., 2001).

3.2.2 Raman Spectrometer Construction

Modern Raman spectrometers have four major components - an excitation source (i.e. a high power laser), a light collection system, a monochromator and a detector (Zhu Q. et al., 2007).

The excitation source is typically a high power laser, as it provides a monochromatic light source. This is important in distinguishing between the excitation source and Raman scattered light. The wavelength of the lasers used range from ultraviolet to mid-infrared wavelengths (Ferraro J.R. et al., 2003), and a notch filter ensures only light with the wavelength of the laser reaches the sample. Therefore, it is impor-

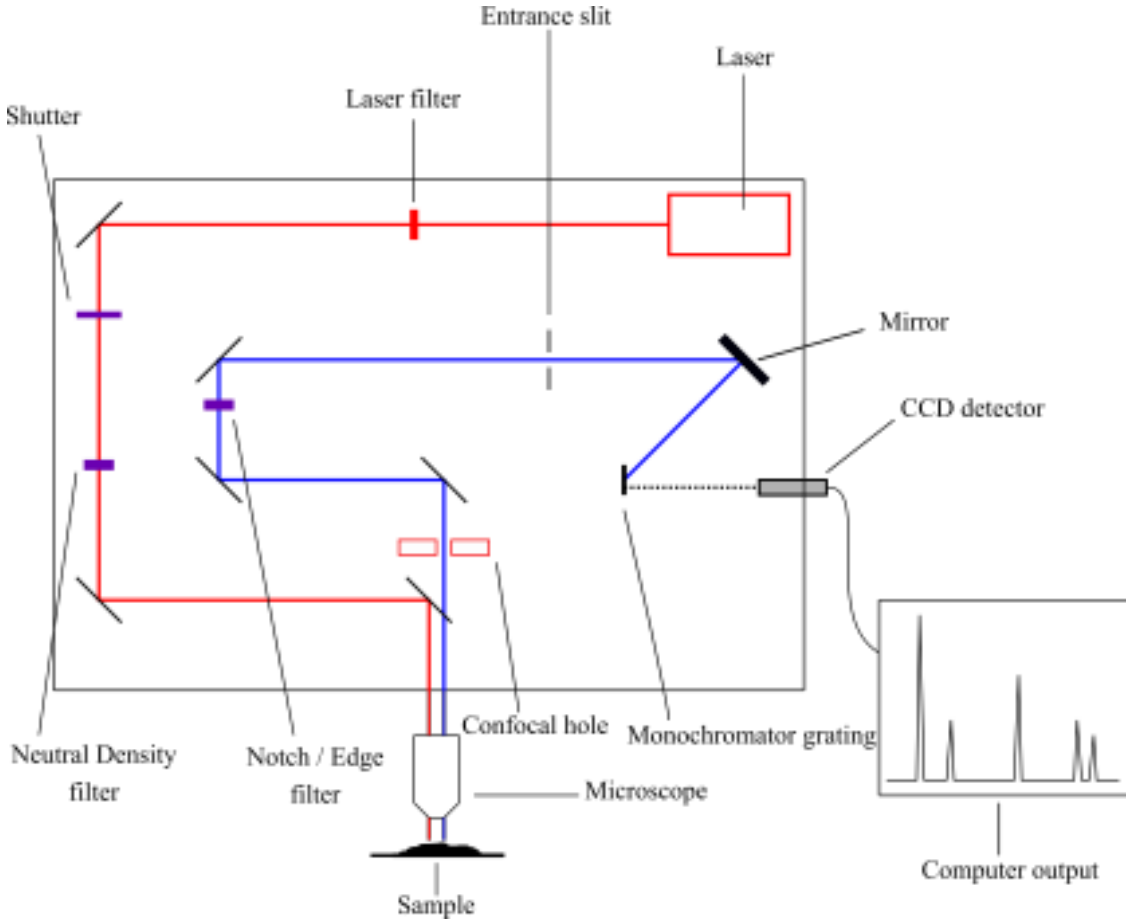

Figure 3.4: Schematic (not to scale) of the Raman spectrometer (a Horiba "LabRam-HR") used at the University of Kent. The red lines represent the path of the incident beam from the laser, whereas the blue lines demonstrate the path of the light after interacting with the sample.

tant that spectrometers are light tight, to minimise the likelihood of extraneous light contamination.

The laser passes through a notch filter before reaching the sample, so that only laser light reaches the sample itself. Raman spectrometers can be equipped with microscopes which can reduce the laser spot size from 1 – 2 μm with high power lens systems (Ferraro J.R. et al., 2003), and by using a microscope objective, the scattered light is collected more efficiently. This is because a microscope objective has a higher numerical aperture value than a simple lens (Hollricher O., 2010), which indicates the range of angles the emitted (Raman scattered) light can be collected from, and is related to the focal depth and physical size of the objective lens. Raman spectrometers can also achieve the greatest spatial resolution through the adjustment of a confocal hole (or "hole"). The hole can control the amount of light that passes through the spectrometer, and so can be used to prevent unfocused light from reaching the detector. However, limiting

the amount of light that reaches the detector can result in lower intensity spectra.

The second filter that the light passes through, after it has interacted with the sample, blocks any light that has been subjected to Rayleigh scattering, as well as any laser light that may have been reflected by the sample. The primary function of this filter is to prevent light from the excitation laser from reaching the detector, by blocking out a specific wavelength. This allows the remaining (Raman scattered) wavelengths to pass through. The two types of filters that can be used for this are "edge" or "notch". Edge filters allow for the transmission of wavelengths above, or below, a certain wavelength, and only transmit light that has experienced Stokes Raman shift, whereas notch filters block a range of wavelengths centred at the laser wavelength, with light at higher and lower frequencies being observed (Slater J.B. et al., 2001), and so can transmit both Stokes and anti-Stokes Raman shifted light. Edge filters are ordinarily used when conducting Raman analysis, including as part of this project, as a greater amount of photons are scattered through Stokes scattering.

After this, the light passes through an adjustable aperture ("entrance slit") and onto a mirror, where it is collimated, reducing any light dispersion as it reaches the spectrometer (Adar F., 2013). Finally, this mirror reflects the collimated light onto a monochromator grating, which splits the light up into its constituent wavelengths and onto the charged coupled device (CCD) detector. The detector consists of an array of light sensitive diodes connected to capacitors (Hollricher O., 2010), which temporarily store the electric charge created when a photon is detected. The information is then transferred to a computer where the data are normally displayed as a graph with the intensity (counts) plotted against Raman shift (cm^{-1}) or wavelength (nm).

3.2.3 Limitations

Generally, Raman analyses are considered non-destructive. However, intense laser power may damage delicate samples, such as biological samples, through laser heating. In order to avoid this, neutral density filters (N.D.) are used to reduce the amount of light that passes through the filter and reaches the sample.

Fluorescence is also an issue that can arise using Raman spectrometry. This can be discerned if the baseline of the spectra appear at higher intensities, rather than at ~ 0 counts, and is a result of impurities ("fluorophores") present within the sample, causing it to fluoresce (Sauer M. et al., 2011). To reduce the fluorescence, the impurities can be removed by using a solvent or creating a pure sample. The wavelength of the laser can also be adjusted to help with fluorescence, particularly for samples that can not be replicated or rinsed in solvent without being damaged, as wavelengths primarily in near-infrared and ultra-violet regions have been found to produce less fluorescence

than those in the visible region (Smith E. & Dent G., 2005). "Photo-bleaching" can also be used to reduce the effects of fluorescence, by irradiating the sample using the excitation laser for some time, effectively degrading and 'burning off' the fluorophores.

Raman spectroscopy is a complementary technique to SEM/EDX as it potentially allows for the identification of a substance, not just its elemental composition.

3.3 Two-Stage Light Gas Gun

The University of Kent's two-stage light gas gun (Burchell M.J. et al., 1999) was used as part of these experiments, to produce a selection of samples investigating in-flight particle cooling. For the detailed set-up used for each set of experiments, see Chapter 7.

3.3.1 Background

The development of light gas guns (LGG) commenced after the Second World War in order to study terminal ballistics (Crozier W.D. & Hume W., 1957). However, over the years, their unique abilities to create various shock environments and fire projectiles into the hyper-velocity range has increased their use in a range of diverse fields such as material science, planetary science, as well as the highly topical field of astronautics and evaluating the hazard of orbital debris to space assets.

Modern two-stage light gas guns allow for the firing of a variety of projectiles of different sizes and materials, at a range of velocities with the ability to accelerate projectiles up to $8\,\mathrm{km\,s^{-1}}$. In order to do this, they require the ignition of a propellant, which then pushes a piston to compress a column of light gas (or "driver gas"). The compressed gas is then rapidly released by the rupture of a burst disc, which accelerates the projectile to impact the target (Burchell M.J. et al., 1999).

3.3.2 Components of the Light Gas Gun

Figure 3.5 and Figure 3.6 show the different components and assembly of the LGG.

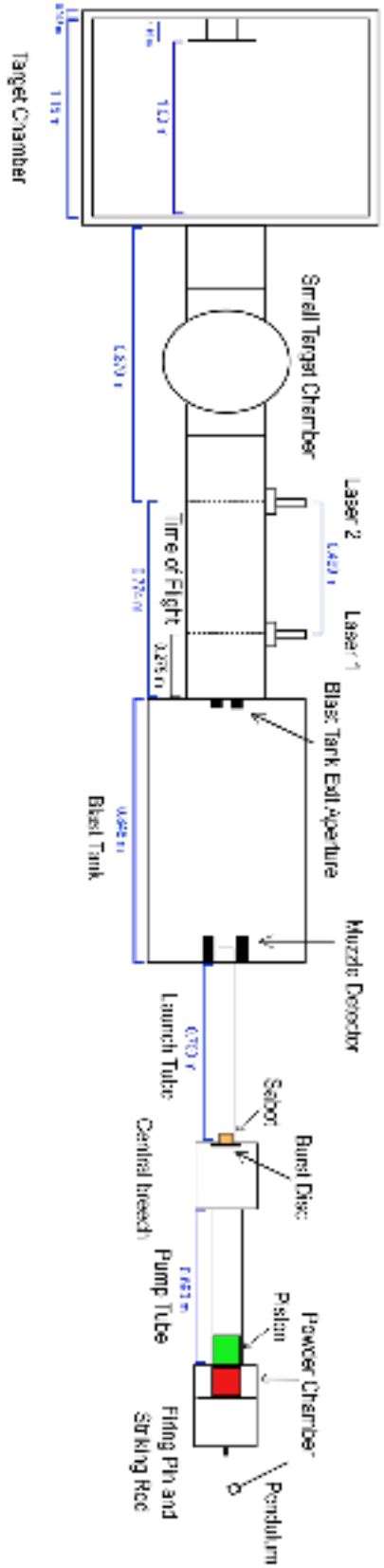

Figure 3.5: Schematic (not to scale) of the two-stage light gas gun used at the University of Kent.

Figure 3.6: Photograph of the University of Kent's light gas gun.

Prior to firing, a projectile is placed at the beginning of the launch tube and a shotgun cartridge is loaded into the powder chamber. A brass pendulum is used to hit the striking rod which pushes the firing pin onto the shotgun cartridge primer cap,

igniting the powder. The shotgun cartridges are filled with 8 - 12 g of rifle powder (depending on the speed required) and stuffed with wadding, after which they are sealed by crimping the cartridge.

The pump tube stores the driver gas prior to firing. A nylon piston inserted into the pump tube, creates a tight seal to ensure none of the driver gas can escape during the gas compression process. Once the powder has been ignited, the piston is pushed down the pump tube at a speed of approximately $1\,\mathrm{km\,s^{-1}}$, compressing the driver gas. This increases the temperature which, in turn, causes an increased projectile velocity. The piston also assists in maintaining the increased pressure generated behind the sabot after the burst disc has ruptured (Doulan C.J., 2001), conserving the acceleration of both the sabot and the projectile.

The central breech funnels the driver gas from the pump tube into the launch tube, and captures the piston prior to hitting the launch tube. An aluminium alloy disc (12.7 mm diameter) is used as a burst disc, which acts as a diaphragm by stopping the driver gas from moving down the launch tube prematurely. A sabot holds the projectile (such as the powders discussed in Chapter 7) and is pushed down the launch tube by the driving gas before reaching the blast tank. An aperture is located at the blast tank exit, allowing the projectile to pass through without the sabot. This happens by the launch tube imparting a spin on the sabot, allowing the four parts to spin off axis, which are then stopped by the stopper plate (with the projectile continuing down the original flight path). There is also a stop plate placed just before the aperture, which can prevent off-axis sabot sections from hitting the inside of the blast tank. The stop plate is also equipped with an impact sensor, which can determine the velocity that the sabot was travelling at to an accuracy of $\pm$ 4% (Burchell M.J. et al., 1999). When the sabot segments impact the stop plate, a shock wave is generated that is detected by the sensor and recorded by an oscilloscope. The time taken for the shock wave to travel can be determined by measuring the distance from the impact on the stop plate to the sensor, followed by the use of a muzzle detector located at the start of the blast tank, to determine the velocity of the sabot.

The speed of the projectile can also be determined using two laser curtains (Figure 3.7), 0.499 m apart. As the projectile passes through the laser curtains it creates a shadow (similar to the chronograph discussed in Chapter 6) which is recorded by a photo-diode connected to an oscilloscope. By using the distance between the lasers and dividing it by the time in-between the interruption of each laser curtain (obtained from the oscilloscope), the projectile velocity can be accurately determined.

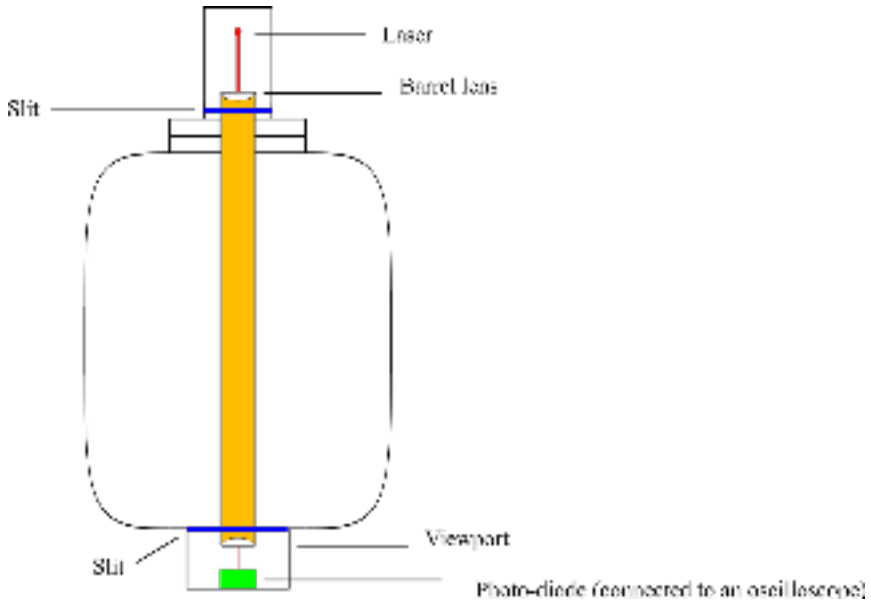

Figure 3.7: Schematic (not to scale) of the laser curtain used to determine projectile velocity on the two-stage light gas gun at the University of Kent. The photo-diode is connected to an oscilloscope and records any light changes as the projectile passes through.

The final component of the LGG is the target chamber. Targets are ordinarily mounted on the inside of the target chamber door, but can be placed free-standing in the centre of the main chamber, or in the blast tank aperture if needed. The main chamber also has a number of ports, allowing for observation or high speed recording of the target during impact.

These three pieces of equipment were the primary tools used to investigate the GSR samples described in this thesis.

Chapter 4

Experiment 1: Particle Identification and Classification using Oxford Instruments' automated INCA GSR software

The investigations into the identification and classification of GSR using a commercial, and widely used in the forensics industry, software package are presented in this chapter. These preliminary tests provided the foundations for the follow-up experiments presented in this thesis (Chapters 5, 6 and 7) and proved invaluable for the understanding of the automated INCA GSR software shortcomings.

4.1 Introduction

Previous research from Fojtasek L. et al. (2003) stated that the maximum number of GSR particles were observed at a distance of 200 cm - 400 cm from the discharged firearm, using 9 mm Lugar ammunition and a CZ 85 pistol (Figure 4.1). To investigate and verify this, 5.56 mm (376 $\mathrm{m\,s^{-1}}$) CCI Minimag FMJ rim-fire ammunition was used in conjunction with a 0.22″ Browning Buck Mark long rifle pistol (Table 4.2).

Table 4.1: Table showing the CZ 85 semi automatic pistol technical information (Ceska Zbrojovka).

Technical Data	CZ 85
General	
Calibre	9 x 19 mm
Operating Principle	Blowback
Magazine Capacity	16 rounds
Sights	Iron sights
Muzzle Velocity	360 ms^{-1}
Dimensions	
Length (min./max.)	Approx. 206 mm
Barrel Length	Approx. 120 mm
Weight	
Weapon (loaded)	Approx. 1000 g

Table 4.2: Table showing the 0.22″ Browning Buck Mark long rifle pistol technical information (Browning, 2015).

Technical Data	Browning Buck Mark Long Rifle Pistol
General	
Calibre	5.56 x 15 mm R
Operating Principle	Blowback
Magazine Capacity	10 rounds
Sights	Iron sights
Muzzle Velocity	382 ms^{-1}
Dimensions	
Length (min./max.)	Approx. 241 mm
Barrel Length	Approx. 140 mm
Weight	
Weapon (without magazine)	Approx. 964 g

Rim-fire ammunition releases less energy upon firing and teeters between subsonic (below $343\,\mathrm{m\,s^{-1}}$ and supersonic above $343\,\mathrm{m\,s^{-1}}$). As a result, rim-fire ammunition is considered 'weaker' than centre-fire ammunition (discussed in Chapter 2).

In this set of experiments, Oxford Instruments' automated software 'INCA GSR' (Oxford Instruments, 2004) was used for the detection and classification of GSR. This software distinguishes GSR from miscellaneous particulates in a sample by examining

a particle's brightness and contrast, along with elemental composition. To detect particles using brightness and contrast, INCA GSR has to operate under BSE conditions (see Chapter 3). Using BSE mode causes heavier, denser particles to shine brightly within a sample. As GSR particles primarily consist of heavy metals, they can be distinguished from the background and, lighter, less dense particles, by calibrating the BSE feature detection settings using a cobalt (Co), gold (Au) and rhodium (Rh) standard supplied by Oxford Instruments. However, as the automated feature detection process relies on the brightness and contrast to be maintained above this calibrated threshold, issues can arise if the number of counts per second fluctuate during analysis.

The first step of the automated analysis is a morphological filter categorising particles based on their morphologies (i.e. spheroidal or 'irregular'). Once a particle has been classified as spheroidal and is, as a consequence, a particle of interest, a rapid EDX scan follows to determine whether the elements of interest are present (i.e. Pb, Sb and Ba). If the particle does not contain any GSR-related elements (including those that could potentially be attributed to being from an environmental origin) then the particle is categorised as 'Unclassified'. However, if an element associated with GSR is identified, then a complete EDX scan is taken. This allows for a complete EDX elemental profile of the particle to be acquired which is then used to automatically classify the particle in one of three categories: 'Unique' (corresponds to 'characteristic' under ASTM guidelines), 'Indicative' (corresponds to 'consistent with GSR' under ASTM guidelines) or 'Environmental'. The morphological filter was disabled for the purpose of these analyses to ensure particles of all morphologies were investigated and categorised based solely on their elemental compositions. At the end of the run, INCA GSR produces an extensive spreadsheet with all the information acquired (e.g. number of particles, number of particles per classification, location on substrate, size, area, relative elemental composition etc.).

To determine the most suitable parameters for the automated feature detection, several calibrations were run. During these tests, the variations in the number of counts per second and features detected meant that the calibration instructions stated in Oxford Instruments (2004) did not produce consistent results. Therefore, to optimize the process and ensure the consistent detection of particles, the calibration thresholds were altered to no brightness (0%) and high contrast (100%) settings. In employing this calibration, a larger number of particles was detected due to the increased contrast. The morphological filter embedded in INCA GSR can be used to exclude particles of non-spheroidal morphologies. However, when INCA GSR has detected a potential GSR particle based on the morphological filter applied and a preliminary EDX scan, a second, thorough EDX spectrum is acquired for confirmation. Then, depending on their

relative elemental compositions, particles are classified accordingly. There are three key ranks for the classification of GSR in the INCA GSR software: unique (equivalent to 'characteristic'), indicative (equivalent to 'consistent') and environmental. The particles that contain all of the 'characteristic' GSR elements are ranked as 'unique', the ones with only some (two or more) of the elements present are ranked as 'indicative', and particles ranked as 'environmental' often comprise of one element (Table 4.3). An 'unclassified' rank is attributed to particles whose elemental composition does not consist of any of the elements associated with GSR. As this chapter pertains to the use of INCA GSR, the INCA GSR classification ranks are used to describe relative particle compositions (rather than 'characteristic' and 'consistent').

By combining the high contrast calibration setting with the EDX spectrum classifications, the automated INCA GSR software was able to yield consistent results for the experiments discussed in this section.

Table 4.3: Table showing the classification ranks for particles of GSR-associated elemental compositions using the automated INCA GSR software.

Rank		
Unique	*Indicative*	*Environmental*
SnSbBaPb	SbBa	Sb
SbBaPb	SbPb	Cu Zn
SbSnPb	BaPb	Ni
SbSnBa	SbSn	Pb
Ti Zn Cu	Sr	Sn
SnBaPb	Ti Zn	Au
Ti Zn Sn		lighter flint
		Fe
		Cu

4.2 Materials & Methodology

Two test firings were carried out as part of this investigation: Experiment 1.1 and Experiment 1.2. The first experiment (Experiment 1.1) was primarily used to determine whether residues were observed up to a distance of 200 cm, in accordance with the literature. However, once the data were examined (presented in Figure 4.4 in the Results section below), it was deemed worthy to investigate the existence of residues up to 400 cm from the firearm (Experiment 1.2).

The collection substrates for this experiment were 25 mm aluminium pin stubs with double-sided, adhesive carbon tape, typically used for SEM analyses. The substrates were placed in their individual containers and were only taken out for the test firing in a closed room using gloves to ensure that they remained as uncontaminated as possible.

4.2.1 Experimental Set-up

Figure 4.1 and Figure 4.2 show the set-up where aluminium pin substrates were set up on a long table, perpendicular to the firearm for maximum residue collection. This was done by employing the use of metal brackets with custom made holes near the top where the aluminium pin stubs were inserted and held in place using nuts, allowing the substrates to be at a consistent height. An additional collection of substrates was arranged horizontally in a straight line down the centre of the firing line to catch any falling residues. All results displayed in the Results section below combine the data from all three substrates at each distance.

The substrates were placed at 20 cm increments from the firearm, starting from 0 cm and up to 200 cm or 400 cm (Experiments 1.1 and 1.2 respectively). The first aluminium substrates at 0 cm from the firearm were placed directly under the muzzle at 6 cm apart from each other. The subsequent stubs were placed at a width of 15 cm apart which decreased by 5 mm at each interval up to the final distances tested (Figure 4.1).

To determine the appropriate firing height, an inclinometer and laser were used. As the test firing was carried out indoors, a bullet catcher had to be used at the end of the sampling range to collect the fired projectiles. Therefore, to confirm that the test firings would be safe, the firearm was set up on the stand used during firing to ensure the projectile flew over the substrates, and a laser was attached to the muzzle. Once the laser was pointed at the bullet catcher, an inclinometer was used to determine the angle from the horizontal (-8.1°). This translated to the substrate height at bench level being approximately 5 cm below the firing line shown by the laser (Figure 4.2).

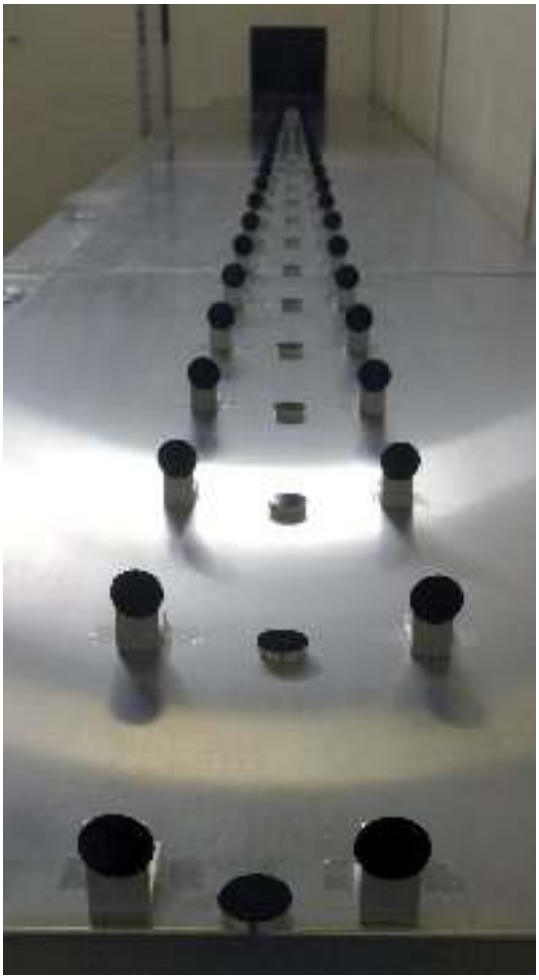

Figure 4.1: Photograph of the experimental set-up of Experiment 1.2 showing the decreasing sampling width along the entire 400 cm sampling range.

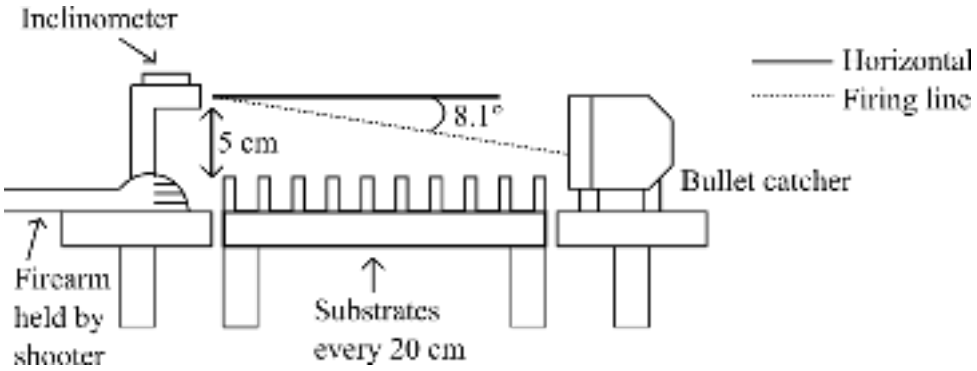

Figure 4.2: Diagram (not to scale) showing the firearm placement as part of the experimental set-up.

Three consecutive shots were fired using 5.56 mm 376 m s^{-1} CCI Minimag FMJ rim-fire ammunition with a Browning Buckmark long rifle pistol.

4.2.2 Analytical Methodology

Post firing, the substrates were packed in their individual boxes prior to being taken for SEM analysis using Oxford Instruments' automated INCA GSR software. However, despite the small size of the residues collected on the double-sided, carbon tapes, there was a significant amount of charging (see Chapter 3). The electron beam voltage was reduced from 20 kV to 10 kV in a attempt to prevent this, and although the charging effect on the samples was reduced, it still remained. Carbon coating is the standard forensic practice for coating samples (Gunshot Residue Subcommittee, 2020) but, unfortunately, the department did not have one at the time of these experiments. Therefore, to reduce the sample charging further, all of the 25 mm substrates were coated in a 15 nm layer of platinum (Pt) using a sputter coater (Figure 4.3). This led to slightly lower X-ray peak intensities but the successful identification of particles remained unaffected due to the 'saturated' acquisition settings.

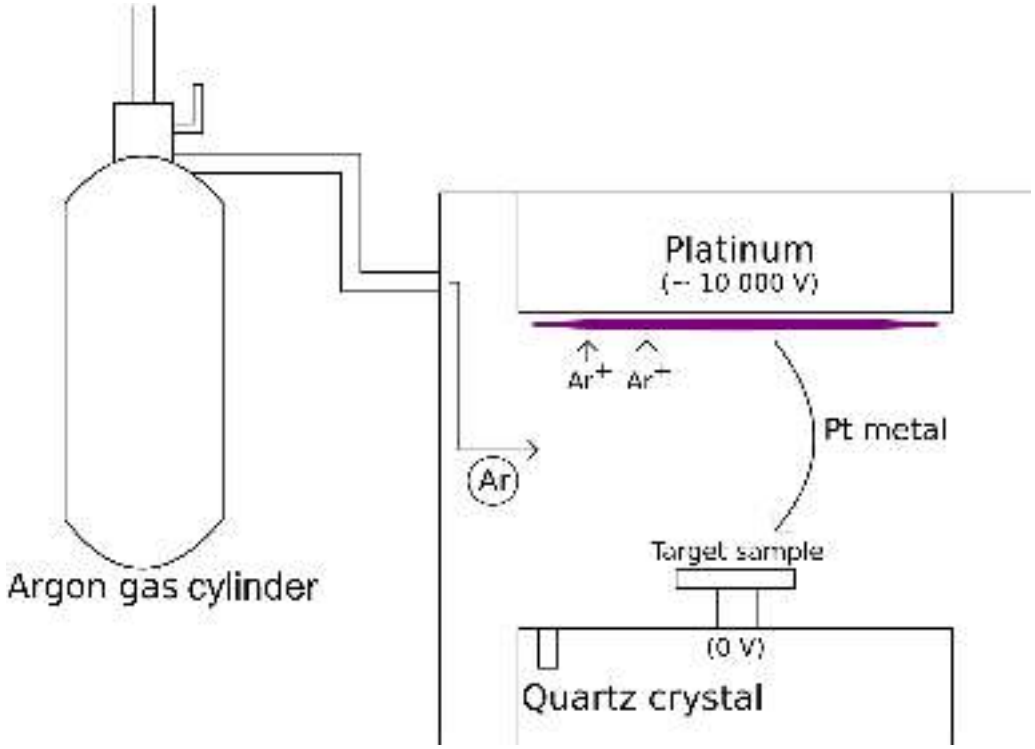

Figure 4.3: Diagram (not to scale) showing the operation of a platinum sputter coater.

The gas cylinder supplies argon (Ar) into the sputter coater vacuum chamber. In the sputter coater, there is a Pt target. The high operating voltage ($\sim 10\,000$ V) creates a plasma (shown in purple in Figure 4.3). As the target sample placed inside the sputter coater vacuum chamber is at 0 V, Pt metal ejected by the Ar plasma accelerates down and uniformly coats the sample surface (Figure 4.4). The quartz crystal near the

sample is sensitive to changes in mass and so detects the amount of metal deposited, which determines the coat thickness.

After confirming that the samples were no longer charging, INCA GSR was used to automatically identify and classify the particles. As mentioned in the introduction, after multiple tests to optimise the operation of the INCA GSR software, the BSE SEM operation mode was used. Under normal BSE settings, the detector gain value was on 3. However, at the time, the Kent SEM had a dead BSE detector segment (Figure 4.5, segment C). In order to avoid 'shadowing' on the sample due to the dead detector segment, its counterpart (Figure 4.5, segment A) was also switched off. This led to the samples appearing very dark and particles were indiscernible. As a result, the gain value was increased to 4 to allow for the particles to be detected and analysed.

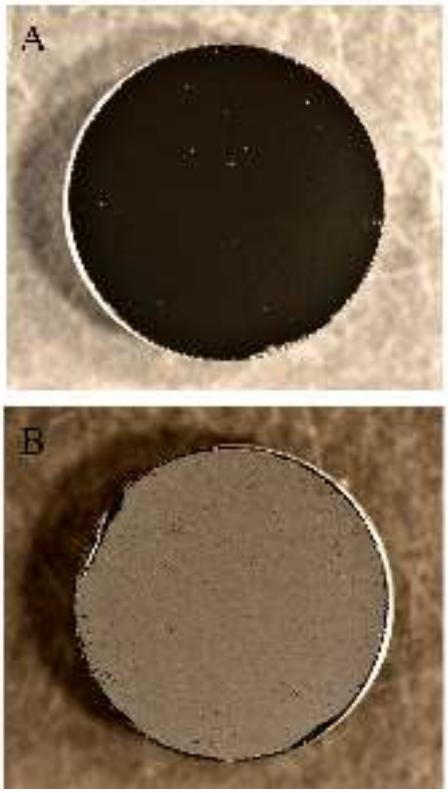

Figure 4.4: Pictures of two 25 mm aluminium stubs with double-sided, adhesive, carbon tape post firing showing the visual difference after applying a Pt coat using the sputter coater. A: no Pt coat, B: 15 nm Pt coat applied.

Due to the large substrate size, only 25% of the samples were analysed via a randomised field selection process selected by the INCA GSR software. This was due to the long run time for each sample (approximately 15 hours for 25 % substrate analysis) however, due to the high particle density on the substrates, sufficient residues were identified for each classification rank at each distance sampled. The aperture was

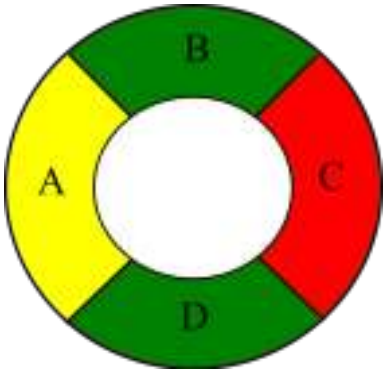

Figure 4.5: Diagram (not to scale) showing the operational BSE quadrants on the SEM at the University of Kent. Green: operational segments, red: non-operational segment, yellow: operational segment, but was switched off during data acquisition to avoid 'shadowing' of sample leading to undetected and misidentified particles.

taken all the way out, increasing the X-ray count (see Chapter 3) to boost the count threshold. The INCA GSR calibration manual stated that the count levels should be at approximately 3000 per second. However, as the filament producing the electron beam slowly erodes, the emission current fluctuates and can often drop below that threshold. By taking the aperture out, the counts were maximised, and any fluctuations, or dips, in the emission current would not impede the data acquisition process. Additionally, an electron beam voltage of 27 kV was used to ensure the counts stay above the 3000 threshold, even if the beam was to drift slightly, or the emission current was to fluctuate during the data acquisition process. This accelerating voltage also gave the highest count rate without any detectable charging. A magnification of $\times 600$ was used for each sample run, with the minimum particle size detected restricted to three pixels, equating to the smallest expected particle width being 1.67 µm at the 768×512 resolution used. The calibration settings that were used for consistency were- brightness on minimum (0%) and contrast on maximum (100%).

4.3 Results

Experiment 1.1 was primarily used to determine whether GSR particles were observed at 200 cm from the firearm. As this was a preliminary experiment, the samples between (and including) 40 cm and 180 cm were used for the optimisation of the INCA GSR software (Figure 4.6). These samples were, therefore, excluded from analysis due to varying amounts of beam damage and Pt coating experienced during the analysis

optimisation process. A comparison table for the particle data obtained at 20 cm and 200 cm from the firearm are displayed in Table 4.4.

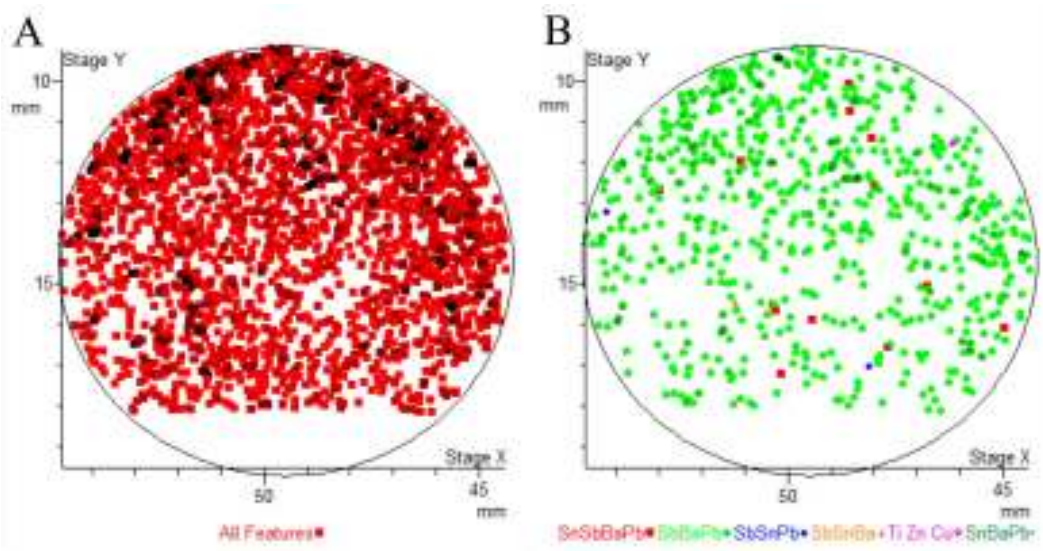

Figure 4.6: Picture of the 40 cm distance sample data obtained using the INCA GSR software. The beam drift led to an incomplete mapping of the sample, seen by the absence of particles on the bottom. The ranks allocated correspond to the INCA GSR default classification system. A: all features detected in the sample, B: only the features classified as 'unique' are displayed.

Table 4.4: Table comparing the 20 cm and 200 cm particle data for Experiment 1.1. The ranks allocated correspond to the INCA GSR default classification system.

Distance from Firearm (cm)	Total Number of Features Detected	Rank
20	6187	1053 Unique 3356 Indicative 1586 Environmental 192 Unclassified
200	7317	43 Unique 1474 Indicative 5790 Environmental 10 Unclassified

As there was a significant number of particles detected at 200 cm from the firearm, Experiment 1.2 was carried out to determine the distance at which the number of GSR particles collected diminished. Figure 4.7 shows the particle number and classification data for the samples investigated, up to 400 cm from the firearm.

The mean particle size as a function of distance per classification was also investigated (Figure 4.8), along with the relative elemental composition for the particles

classified as 'unique' (Figure 4.9). Due to the varied particle size distribution between the different samples, error bars could not be plotted on the graph without affecting the readability of Figure 4.8.

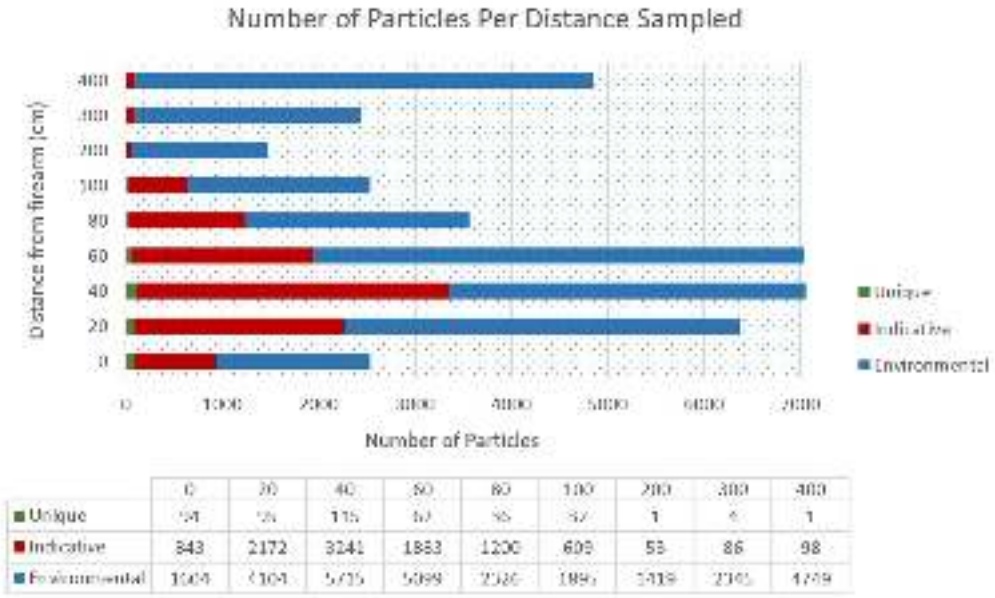

	0	20	40	60	80	100	200	300	400
Unique	94	58	115	67	95	57	1	4	1
Indicative	843	2172	3241	1863	1200	609	55	86	98
Environmental	1004	4104	5475	5099	2580	1895	2419	2745	4749

Figure 4.7: Graph comparing the number of classified particles per sampled distance for Experiment 1.2. The ranks allocated correspond to the INCA GSR default classification system.

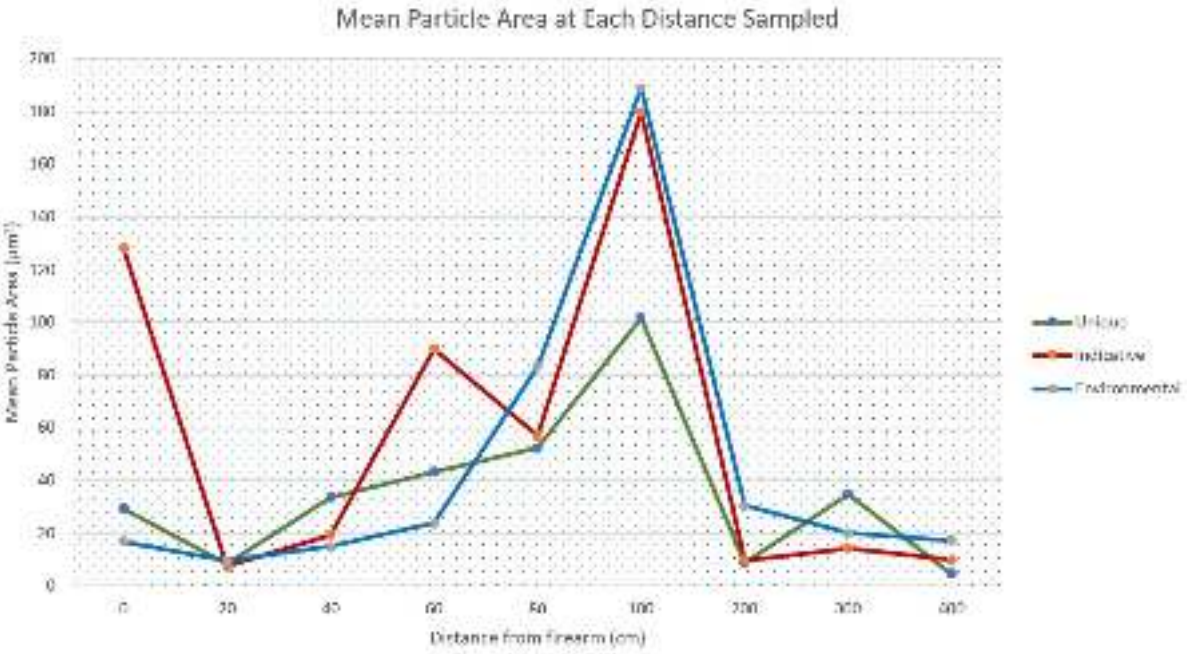

Figure 4.8: Graph comparing the mean particle area for each classification rank per sampled distance, ±1 standard deviation could not be plotted on the graph without affecting the readability. The values were determined by using the mean area value for each particle type provided by INCA GSR, and the ranks allocated also correspond to the INCA GSR default classification system.

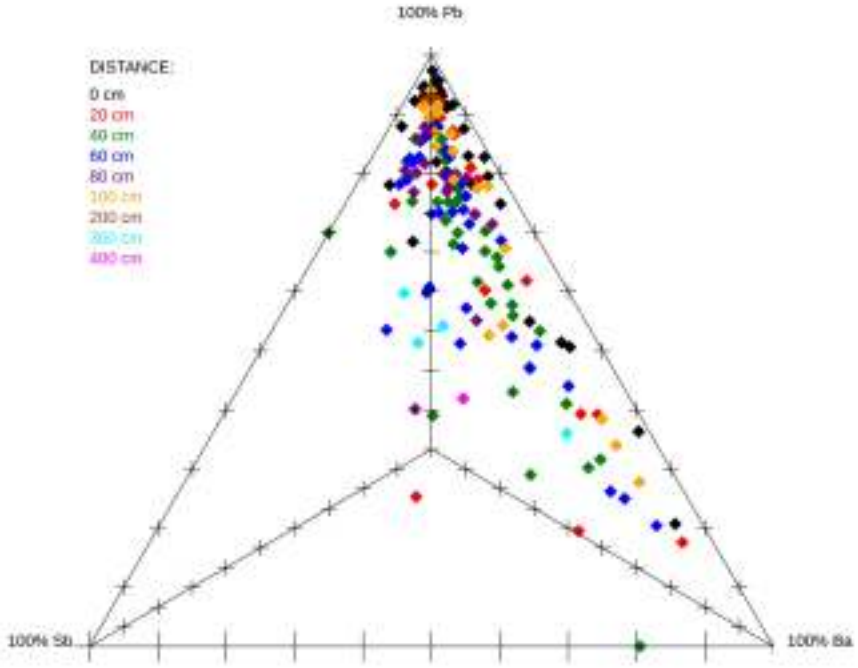

Figure 4.9: Ternary graph showing the relative elemental abundances of Pb, Sb and Ba for 'unique' particles over the distance range sampled.

4.4 Discussion

The results of Experiment 1.1, displayed in Table 4.4, indicate that a significant number of particles are identified both within 20 cm and 200 cm from the firearm. In fact, at 200 cm from the firearm there is a larger number of particles collected than at 20 cm, and with only 10 of those being identified as 'unclassified'. However, the number of 'unique' and 'indicative' particles are both significantly higher at 20 cm from the firearm. This raised the question as to whether the abundance of environmental particles at the distance farthest from the firearm was due to their size, or 'simpler' elemental composition, investigated in Experiment 1.2.

Examination of Figure 4.7, corresponding to the Experiment 1.2 data, suggests that the maximum number of residues collected peaks 40 cm and 60 cm from the firearm. This is observed for all three classification types, and is likely due to the firearm discharge plume reaching maximum dispersion at approximately 50 cm from the firearm (discussed in Chapter 6). However, the 'unique' number of particles are always the least abundant and drop significantly over the 400 cm sampling range.

The average particle size was also determined for particles of all classification types over the 400 cm range. This was done by using the mean area for each particle class at each distance. As it can be seen in Figure 4.8, the 'unique' particles are smallest, even at their peak, with 'environmental' particles being only slightly larger than those in the 'indicative' class. Interestingly, the maximum particle size for all three classifications is seen at 100 cm from the firearm, with 'unique' particles having a mean area of 102 μm^2, 'indicative' particles a mean area of 180 μm^2, and 'environmental' particles a mean area of 190 μm^2. The mean particle areas drop significantly after this peak, with only particles with an area less than 40 μm^2 making it to the 400 cm sampling range.

The particle sizes of the 'unique' GSR particles displayed in Figure 4.8 are also worth noting. The data suggests that the 'unique' particles largely tend to have an average area between 10 μm^2 and 100 μm^2. However, working backwards to determine the particle diameter from the area using Equation 4.1, it can be seen that the largest area of 100 μm^2 only gives a diameter of 11.28 μm.

$$A = \pi r^2 \tag{4.1}$$

This particle diameter is consistent with that of GSR particles, however the average diameter of GSR particles typically ranges from approximately 10 μm to sub-micron values, but can be found to exceed 50 μm and 100 μm (Basu S., 1982). Therefore,

for the largest 'unique' particles to have an average area of 100 µm^2, giving a diameter of only 11.28 µm, there must have been an intervening factor. In this case, the factor must be particle morphology. During the particle identification process, it was discerned that some of the residues were not spheroidal in morphology as expected, but rather appeared to indicate irregular morphological structures, potentially due to partial melting (Figure 4.10).

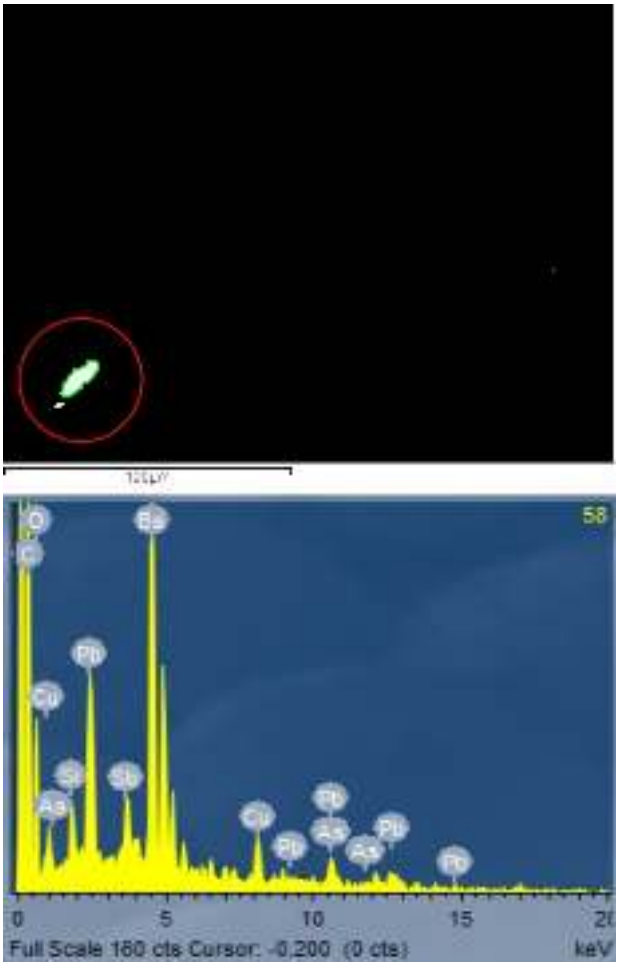

Figure 4.10: BSE SEM/EDX binary image and spectrum of a 'unique' GSR particle using the INCA GSR automated software, showing an example of the irregular, non-spheroidal morphologies encountered during the particle identification process. This particle is approximately 14 µm in diameter and was found 40 cm from the firearm. *HV:* 27 kV.

It was unclear as to whether the morphologies observed here were due to the heat of combustion, or the force of the impact the residues experienced upon hitting the substrates, so follow-up experiments were designed to investigate both hypotheses (see Chapter 7). However, INCA GSR's morphological filter was removed to prevent the exclusion of these non-spheroidal residues from further EDX analyses.

The relative elemental compositions of the 'unique' particles across the 400 cm range do not indicate an overall trend based on their distance from the firearm. However, a point of interest was the high levels of Cu seen in samples. INCA GSR only considers the existence of Cu in particles 'unique' to GSR if it is accompanied by titanium (Ti) and zinc (Zn) due to the composition of lead-free primers (Bauer F. et al., 2016). Otherwise, the existence of Cu is classified as 'environmental', even if it can originate from a brass cartridge or Cu-plated projectiles (such as the FMJ ammunition used in this set of experiments). Therefore, due to the abundance of Cu throughout the distances sampled, as well as it being a key component of the FMJ ammunition used, Cu was included while investigating the effects that elemental composition may have on morphology (see Chapter 5).

Oxford Instruments' INCA GSR was successfully used to identify 'unique' GSR particles at all the distances investigated, but it was found to be very sensitive to SEM set-up conditions and beam stability. The size of the GSR particles was found to drop off with distance, with a maximum at 100 cm from the firearm for this firearm and ammunition combination. The particle number distribution also changes with distance from the firearm, but 'unique' GSR particles were still detected at the maximum distance investigated, 400 cm from the firearm, corresponding to the findings presented by Fojtasek L. et al. (2003). Therefore, samples and swabs for trace GSR analyses should be taken at distances >2 m for any shooting event. Finally, the composition of GSR (i.e. the relative abundance of Pb, Sb and Ba) does not change significantly as a function of distance for this firearm and ammunition combination.

Although INCA GSR allowed for an overall elemental composition of the residues to be identified sufficiently to classify particles into their corresponding ranks, there was little information as to the distribution of those elements within the individual particles. Therefore, follow-up experiments were devised with the same firearm and ammunition combination to investigate further this.

Chapter 5

Experiment 2: Individual particle morphological and elemental composition analyses using FEG-SEM/EDX and Raman Spectrometry

The content in this Chapter is based on, and in areas reproduced from, Spathis V. (2017) entitled 'Impact-disrupted gunshot residue: a sub-micron analysis using a novel collection protocol'. The aforementioned paper was produced during this PhD, and is listed in the declarations for this thesis.

5.1 Introduction

In Chapter 4, the identification of GSR recovered from a distance of 2 m and 4 m (Experiments 1.1 and 1.2 respectively) was determined using the automated INCA GSR software. Although these analyses allowed for an overall elemental composition of

the residues to be identified, there was little information as to the distribution of those elements within the individual particles. Additionally, during the particle identification process, it was discerned that some of the residues were not spheroidal in morphology as expected, but rather showed irregular morphological structures potentially due to partial melting (Figure 4.10). Although the concept of coalescence of molten droplets to form GSR is not unknown (Basu S., 1982), it was unclear as to whether this was due to the heat of combustion, or the force of the impact of the residues onto the substrates. In order to investigate this further, the use of high purity silicon wafers as substrates were employed in an attempt to determine the velocity at which the residues hit the target over a 1 m range. The premise behind the use of these substrates was that the stress induced on the silicon upon impact would cause a shift in the silicon's distinctive Raman peak (at $520\,\mathrm{cm}^{-1}$) due to the strains induced within the crystal lattice (Peng C.Y. et al. (2009); Anastasakis E. et al. (1970); Price M.C. et al. (2014)), while at the same time capturing particles for individual morphological and elemental composition analyses using FEG-SEM/EDX.

In this experiment, an attempt was made to measure the velocity with which GSR particles travel through the air. Additionally, emphasis was placed in trying to determine the individual particle morphology and elemental composition of rim-fire ammunition GSR particles at the sub-micron level. The novel sampling and analytical techniques used in this experiment demonstrate that particles may not always have sufficient time to cool into spheroidal residues, particularly at low velocities.

5.2 Materials & Methodology

The collection substrates for this experiment were six 600 µm thick optically polished, high purity, silicon wafers, sized approximately 15 mm × 20 mm. These silicon wafers were spares of the solar cells from the Hubble Space Telescope that have previously been used for impact testing (Kearsley A.T. et al., 2007). Prior to the experiment, these silicon substrates were cleaned for 5 min in an ultrasonic bath using High Performance Liquid Chromatography (HPLC) grade acetone and left to dry, placed in their individual containers and were only taken out for the test firing in a closed room using gloves. This ensured that they remained as uncontaminated as possible, and residues found on them during the analytical process were a product of the test firing and not prior contaminants.

5.2.1 Experimental Set-up

The silicon substrates were set up perpendicular to the firearm and 7 cm below the firing line at bench level. They were kept upright and in place with the use of plastic bars that were fixed onto the bench, allowing the substrates to be at a consistent height and perpendicular to the firearm for maximum residue collection. The substrates were arranged in a straight line down the centre of the firing line at distances of 10 cm, 20 cm, 40 cm, 60 cm, 80 cm and 100 cm, as displayed on Figure 5.1 below. Three consecutive shots were fired using the same ammunition as in Chapter 4, 5.56 mm 376 m s^{-1} CCI Minimag FMJ rim-fire ammunition with a Browning Buckmark long rifle pistol in an attempt to get sufficient residues for analysis.

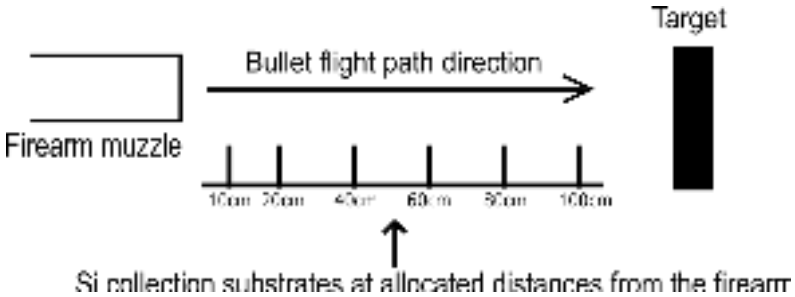

Figure 5.1: Diagram (not to scale) showing the experimental set-up of the silicon collection substrates during the test firing. The distances from the firearm for each substrate are 10 cm, 20 cm, 40 cm, 60 cm, 80 cm and 100 cm.

5.2.2 Analytical Methodology

The silicon wafers were collected immediately after the test firing and mounted on double-sided adhesive carbon tape on aluminium stubs, allowing for SEM analyses. The samples were firstly placed in the SEM where a topographical map of the entire substrate was produced to observe the particle frequency for each distance from the firearm. Subsequently, the samples were then analysed using the FEG-SEM/EDX which allowed for the examination of particle structural morphology (Figure 5.2) and elemental composition (Figure 5.3) at the sub-micron level. This was done by taking the area that was mapped on the SEM (i.e. the entire substrate), increasing the magnification to ×800 and moving systematically through the sample from top left to bottom right. Every three frames at ×800 magnification, the magnification was reduced to ×600 (which was the magnification of the SEM topographical maps) and any particles within that site of interest were analysed.

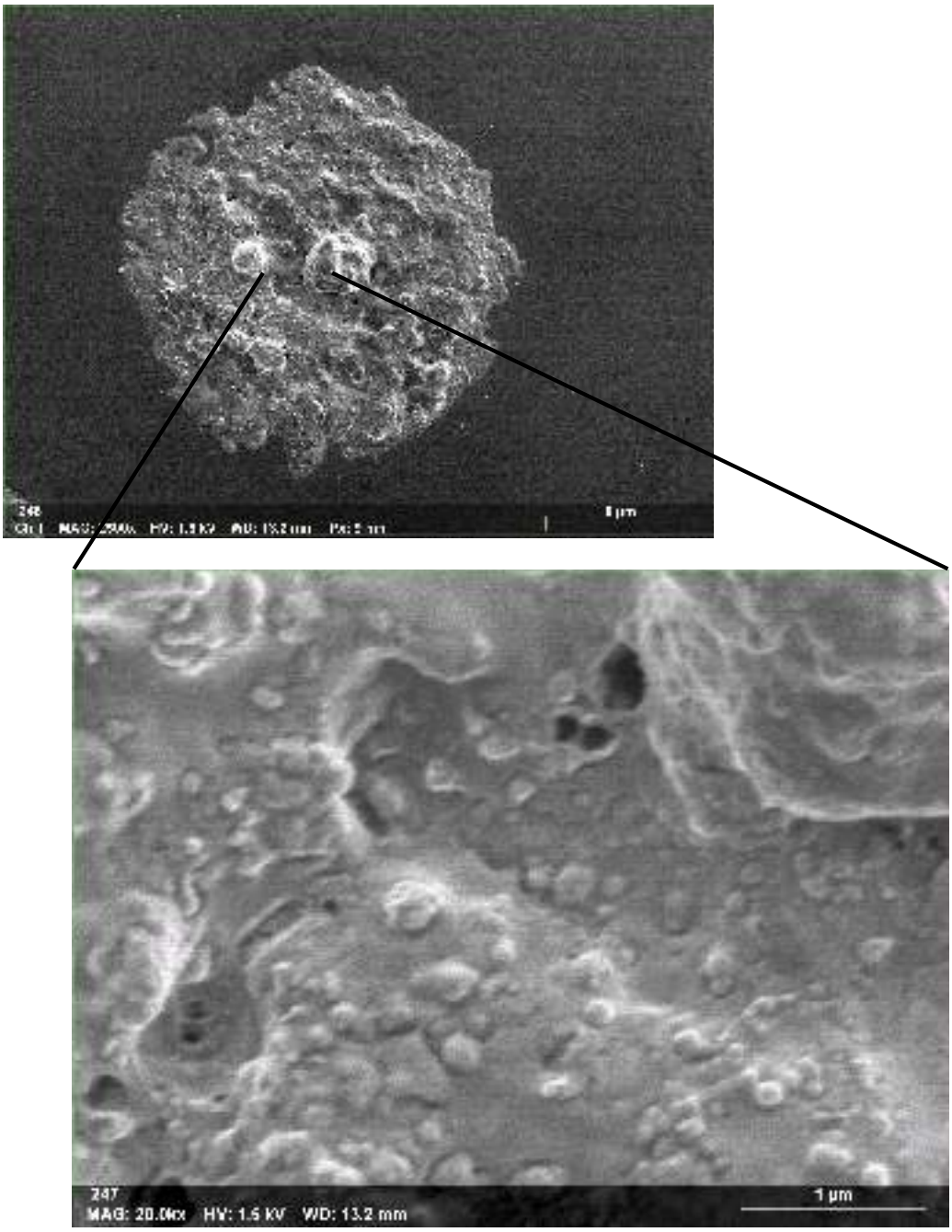

Figure 5.2: FEG-SEM secondary electron image of impact-disrupted GSR showing the imaging capabilities of a cold field emission SEM. Scale on original image: 8 µm, on zoomed in image: 1 µm. *HV* 1.5 kV.

The morphology of the particles was examined using an accelerating voltage of 1.5 kV, which provided a more detailed insight into the surface topography of each particle, as the electron beam does not penetrate deep into the sample, as stated in Chapter 3 (Goldstein J. et al., 2003). However, during the elemental composition acquisition process, the voltage was changed to 10 kV. This gave a poorer image of

the particle as the electron beam is more penetrating and thus surface features are rendered invisible, but the higher accelerating voltage is required to stimulate X-ray emission from metallic elements within the particle. The placement of Bruker's *X-flash* detector around the pole piece prevents particle shadowing (discussed in Chapter 3) which is of particular importance in GSR analysis. Figure 5.3 demonstrates that particle composition can vary within an individual GSR particle. Therefore, if particle shadowing is caused by the detector placement, elements present within that region can remain undetected, leading to misclassification of valuable evidence.

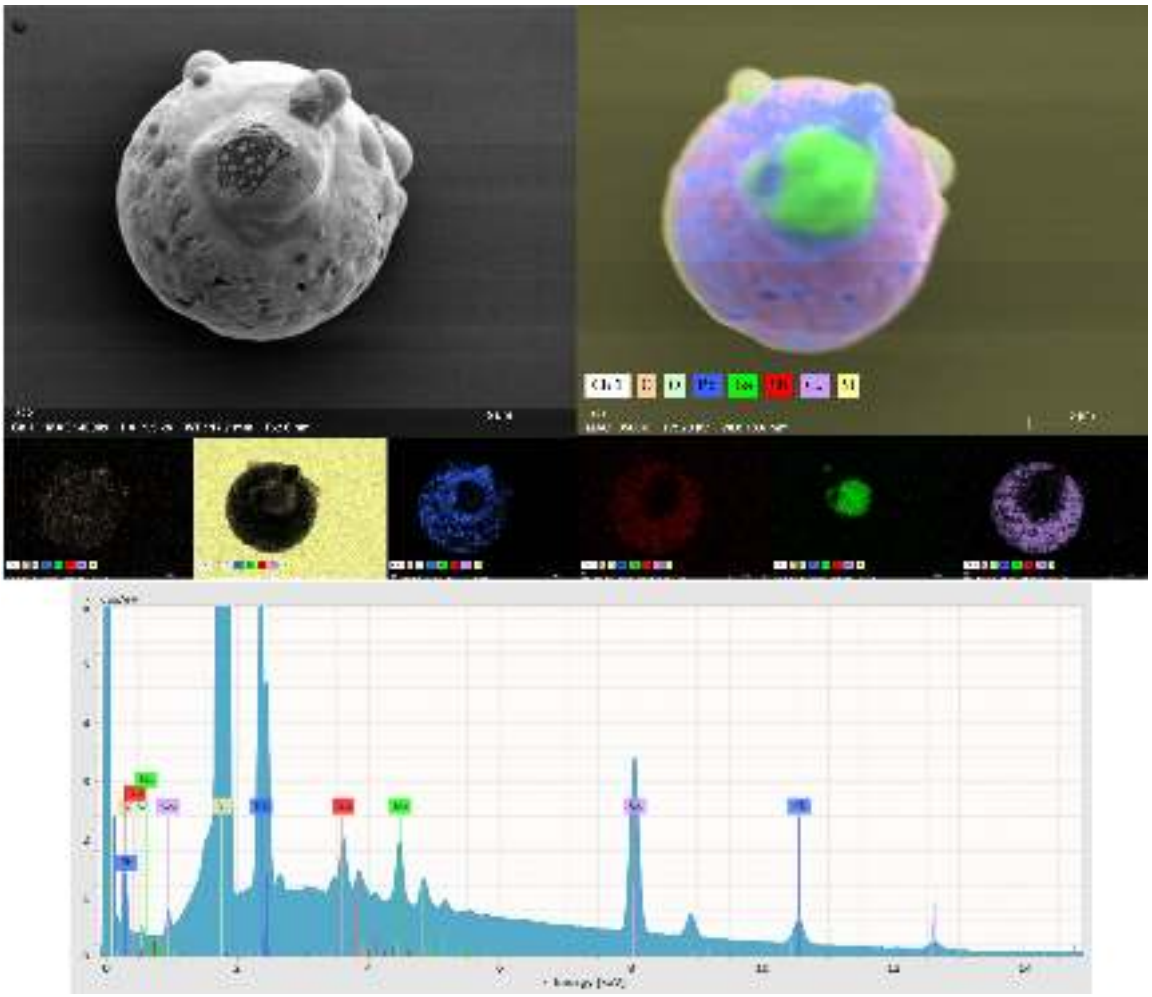

Figure 5.3: FEG-SEM image of a 'characteristic', spheroidal GSR particle, found at 40 cm from the firearm, showing the sub-micron elemental distribution using the Bruker *X-flash* 5060f flat quad EDX detector. Scale on image: 5 µm. Image: *HV* 1.5 keV, elemental maps: *HV* 20 kV.

5.3 Results

The particle distribution across the 1 m range was determined by running image acquisition maps on the SEM. By examining these maps it was apparent that the particle distribution varied across the different distances. Figure 5.4 shows that close to the firearm there is a significant number of small particles distributed throughout the substrate ($\approx 147\,\mathrm{mm}^{-2}$ particle density, Figure 5.4: silicon 1). However, at 60 cm from the firearm the number of particles increases, along with their size ($\approx 451\,\mathrm{mm}^{-2}$ particle density, Figure 5.4: silicon 4), after which the particle frequency decreases ($\approx 72\,\mathrm{mm}^{-2}$ particle density, Figure 5.4: silicon 6).

The few particles that are captured at the 100 cm silicon target appear to be larger in size than those encountered at the previous distances while the highest particle frequency was observed at the 40 cm range. At this distance, the substrate was covered in particles of varying sizes. Figure 5.5 shows the distribution of these particles across the silicon 3 substrate using both BSE and SE SEM conditions.

Upon FEG-SEM analysis of the samples, using a random selection process, it appeared that the frequency at which particles were present on each silicon substrate varied significantly. It was determined that the majority of the residues collected had an irregular morphology rather than their frequently encountered spheroidal shape. These molten-looking, disaggregated GSR particles were named impact-disrupted GSR (IDGSR). Within these particles, there were two populations distinguished, normal incidence and angled IDGSR (Figure 5.6). Consequent to further analysis, this selection of particles could be divided further into several subcategories (Figure 5.7 and Figure 5.8).

A class of particles, shown in Figure 5.10, was also encountered throughout all of the samples. However, as they primarily consisted of organic material with only small amounts of the inorganic 'characteristic' GSR elements, they were excluded from the classification process. The rest of the particles that were identified to consist of primarily inorganic components, were then classified using the IDGSR classification diagram and archetypes mentioned in Figure 5.7 and Figure 5.8. The results are displayed in Table 5.1.

A selection of IDGSRs from each class were also analysed using EDX (Table 5.2). The relative proportions of the 'characteristic' GSR elements in each class were also plotted to show relative elemental composition changes as a function of class over the 100 cm firing rage (Figure 5.9). Although copper does not come under the ASTM guide for characteristic GSR elements (American Society for Testing Materials, 2017), it was

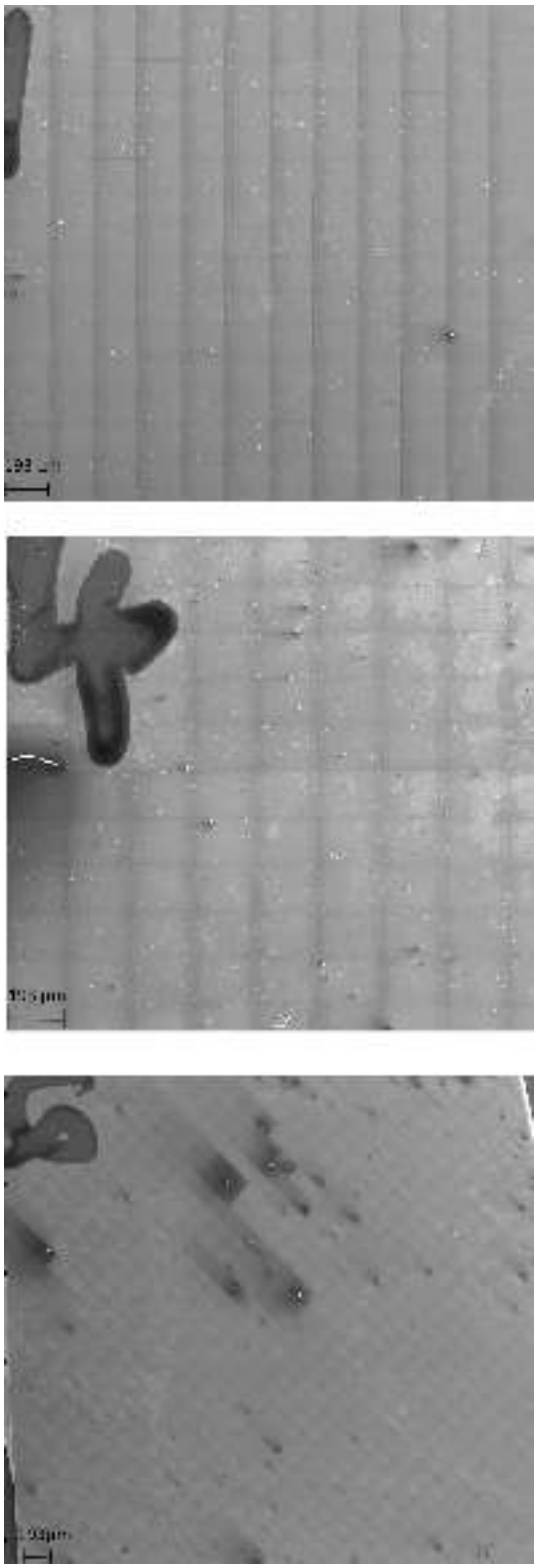

Figure 5.4: SEM secondary electron montage images of three silicon targets showing the particle distribution along the 1 m range. Silicon 1 (top): 10 cm from the firearm, silicon 4 (middle): 60 cm from the firearm, silicon 6 (bottom): 100 cm from the firearm. HV 10 kV.

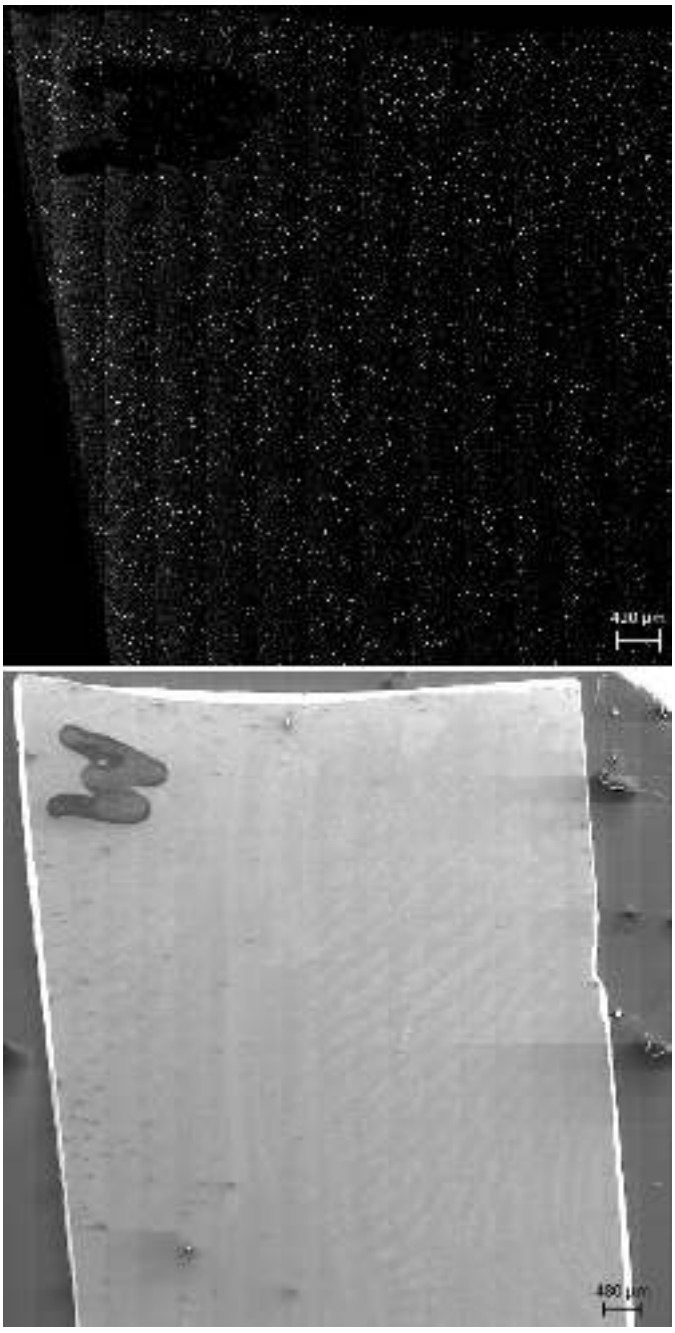

Figure 5.5: SEM montage images of the silicon 3 target (40 cm from the firearm) showing the particle visibility under different SEM conditions. Top: back scatter electron image, bottom: secondary electron image. HV 10 kV. High contrast and low brightness settings were required for the acquisition of the back scatter electron image, therefore the black parts of the image represent the target substrate and the white pixels that appear as noise are actually the high-contrast particles detected.

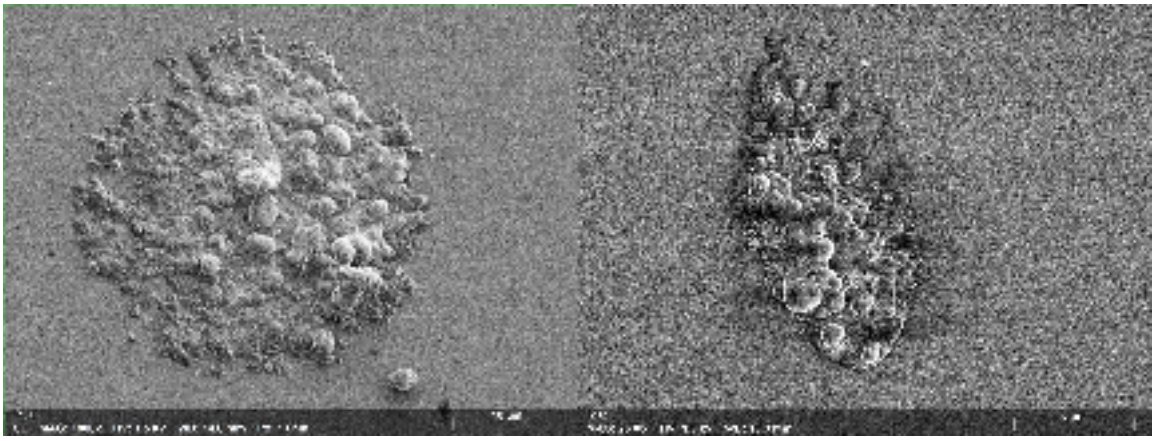

Figure 5.6: FEG-SEM images of two different impact disrupted GSR populations. Left: normal incidence IDGSR, scale on image: 10 µm. Right: angled IDGSR, scale on image: 8 µm. *HV* 1.5 kV.

present in the vast majority of particles analysed (in conjunction with Pb, Sb and Ba) and was therefore included to ensure more accurate relative particle compositions.

Table 5.1: Table showing the percentage of GSR particles per class over the 100 cm sampling range.

Silicon substrate number	Distance from firearm (cm)	Number of particles per class (%)								Total number of particles examined
		Class 0	*Class 1*	*Class 2*	*Class 3*	*Class 4*	*Class 5*	*Class 6*	*Class 7*	
1	10	0.9	1.7	41.9	0.9	0.0	35.9	12.0	0.9	117
2	20	0.0	7.5	40.0	13.3	4.2	22.5	10.0	0.0	120
3	40	3.7	50.0	4.0	17.3	9.3	8.7	0.7	4.7	150
4	60	2.9	5.9	3.9	24.5	23.5	23.5	9.8	2.9	102
5	80	0	2.5	0.8	13.9	22.1	35.2	21.3	4.1	122
6	100	0	3	8.9	3.6	12.5	50.9	10.7	8.0	112

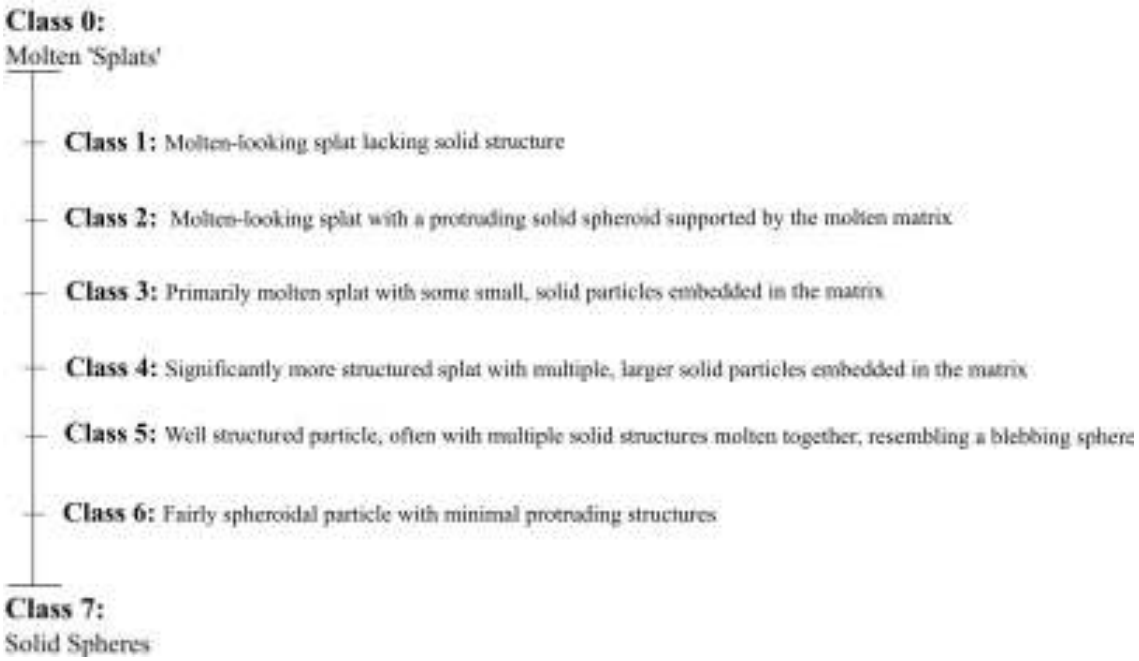

Figure 5.7: Diagram describing the different impact-disrupted GSR classifications, corresponding to the classification images in Figure 5.8. The term 'splat' is used to describe the more molten-looking residues that 'splattered' onto the target substrates.

Table 5.2: Table showing the relative proportions of 'characteristic' elements present in GSR particles ± 1 standard deviation. Values for classes 5 and above show a high standard deviation for % Pb and % Ba as a number of particles of these classes consisted primarily of those elements.

Class Number	Relative particle compositions of 'characteristic' GSR elements (%)			
	Pb	*Sb*	*Ba*	*Cu*
0	78.26 ± 6.33	4.92 ± 0.70	7.70 ± 5.42	9.12 ± 0.60
1	83.03 ± 3.85	2.71 ± 0.91	9.81 ± 3.02	4.44 ± 1.50
2	88.44 ± 2.51	4.30 ± 0.89	3.48 ± 1.54	3.78 ± 1.33
3	82.83 ± 3.17	2.87 ± 1.90	10.87 ± 3.02	3.43 ± 0.78
4	84.65 ± 3.84	2.62 ± 0.68	8.73 ± 1.73	4.01 ± 1.89
5	80.55 ± 21.60	1.79 ± 0.60	13.97 ± 21.99	3.69 ± 0.94
6	75.72 ± 35.96	2.02 ± 0.98	18.53 ± 37.60	3.73 ± 1.76
7	78.11 ± 32.84	2.90 ± 1.89	16.90 ± 33.23	2.09 ± 1.13

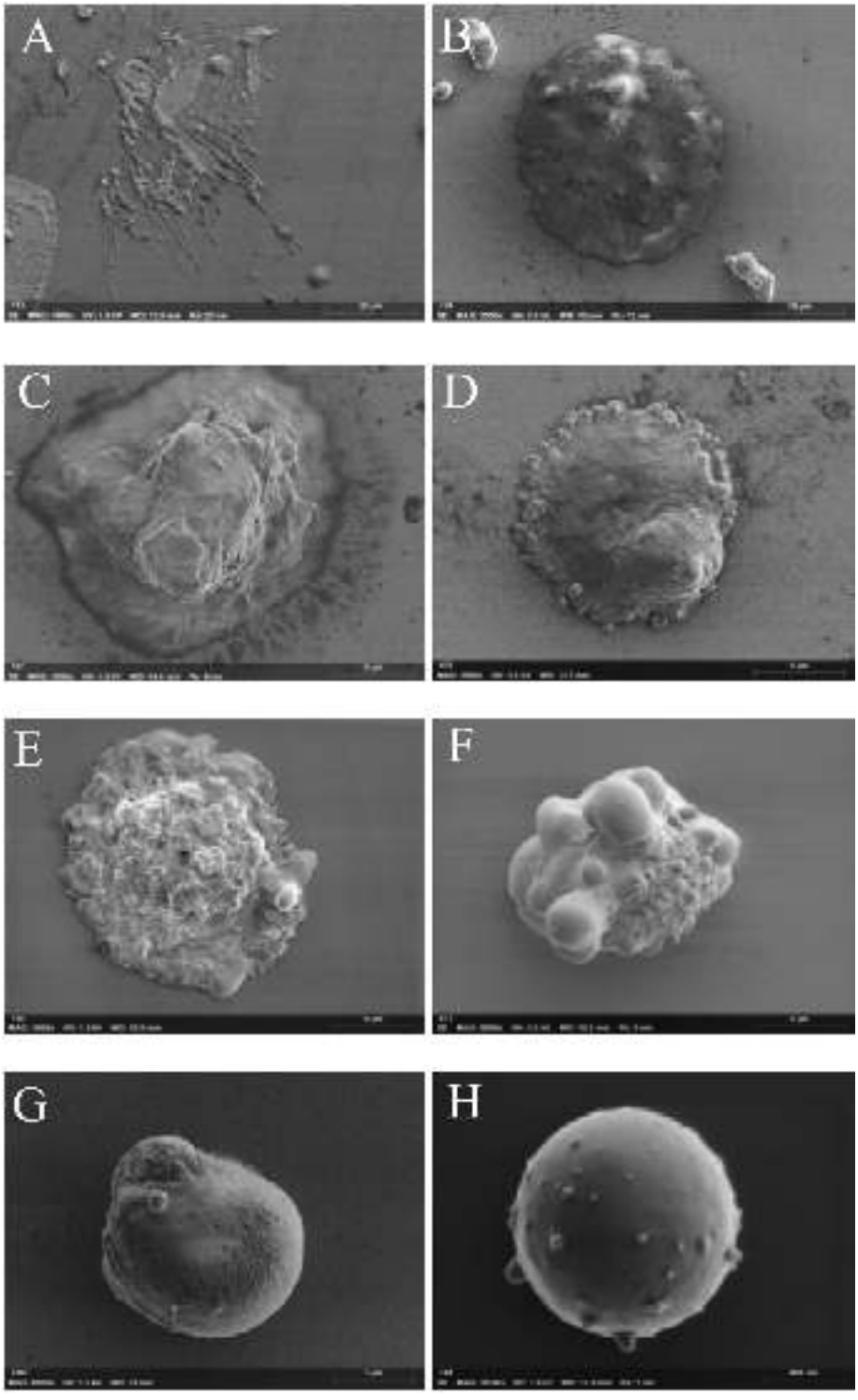

Figure 5.8: FEG-SEM images of archetype impact-disrupted GSR populations over 100 cm range. A: Class 0 (scale on image: 20 µm), B: Class 1 (scale on image: 50 µm), C: Class 2 (scale on image: 6 µm), D: Class 3 (scale on image: 8 µm), E: Class 4 (scale on image: 6 µm), F: Class 5 (scale on image: 4 µm), G: Class 6 (scale on image: 3 µm), H: Class 7 (scale on image: 600 nm). *HV 1.5kV.*

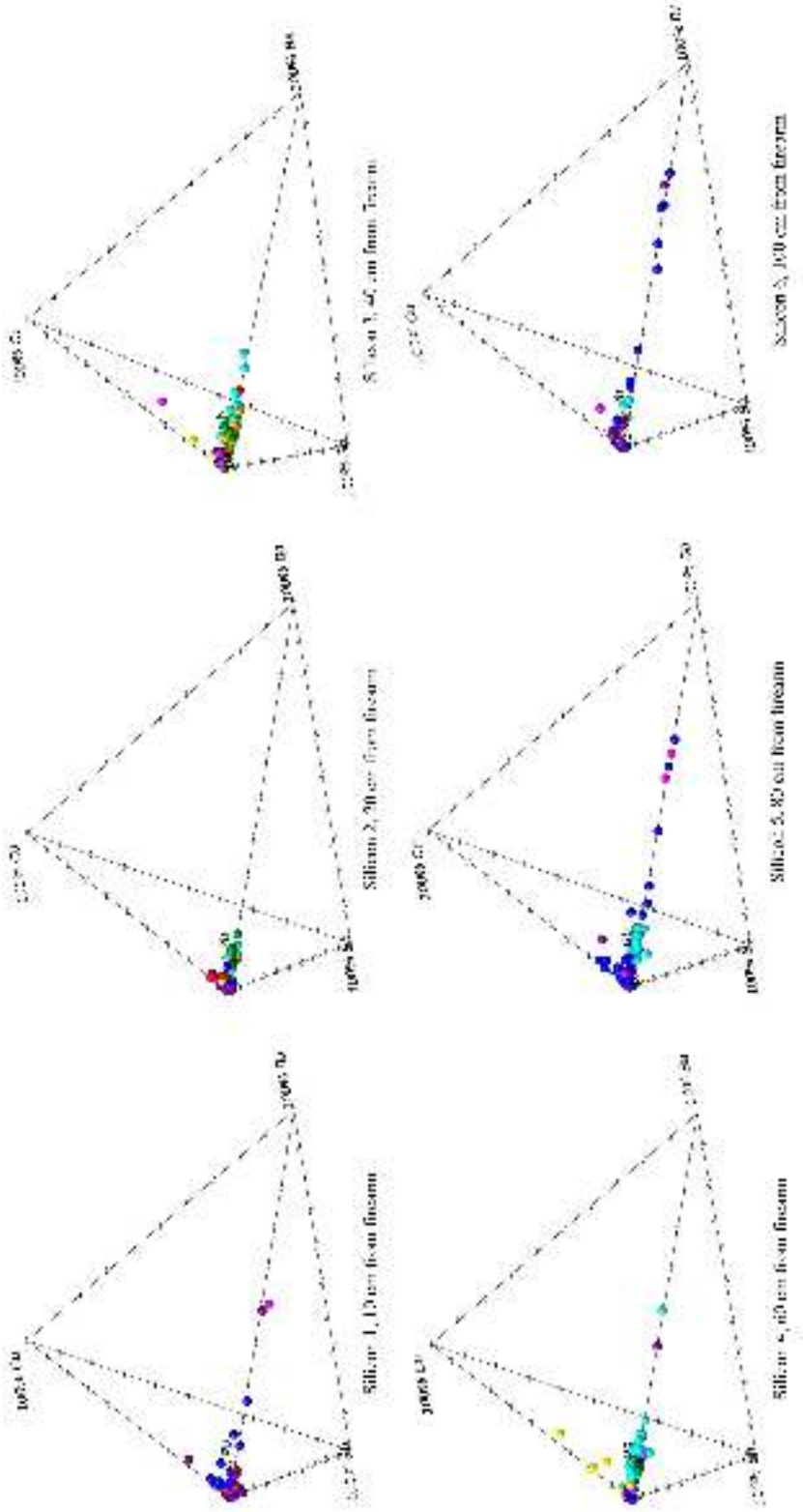

Figure 5.9: A collection of tetrahedral plots showing the relative elemental compositions of individual GSR particles per silicon substrate over the 100 cm range. The IDL code for the tetrahedral plots was written by Dr M. C. Price using the work of Shimura T. & Kemp A. (2015). The corresponding colours for each class are- class 0: yellow, class 1: orange, class 2: red, class 3: green, class 4: cyan, class 5: blue, class 6: purple, class 7: magenta.

Figure 5.10: FEG-SEM image of image of a primarily organic particle. Due to the lack of inorganic, 'characteristic' GSR elements, this population of residues was excluded from IDGSR classification. Scale on image: 5 µm, HV 1.5 kV.

5.4 Discussion

5.4.1 Morphological Analysis

The results from the morphological examination of the impact-disrupted GSRs indicate that there is a clear pattern in class type as a function of distance. As it can be seen from Table 5.1, at the distance closest to the firearm, a high number of Class 2 and Class 5 particles are observed, with minor contributions to the other classes. However, around the centre of the sampling range, at approximately 40 cm from the firearm, the residues analysed primarily fall within Classes 1, 3 and 4. This corresponds to the molten residue 'splattering' observed by Burnett B. (1989) at approximately 30 cm from the firearm, using a 9 mm semi-automatic pistol as well as Ueyama R.L. et al. (1980) who found irregular GSR particles to "appear only rarely at target distances of 12" [$\sim$ 30.5 cm] and beyond". These data suggest that although these residues appear further away from the firearm, they have not had sufficient time to cool in-flight, resulting in their liquid and molten forms (i.e. Classes 1, 3 and 4). However, the residues closer to the firearm exhibit a more solid structure despite being only 10 cm or 20 cm away. Therefore, this suggests that there are two different populations in the firearm discharge plume, each of which may be subject to a different temperature or velocity.

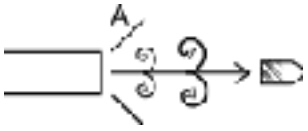

Figure 5.11: Diagram (not to scale) showing the firearm discharge plume expansion as the projectile leaves the firearm.

As is demonstrated in Figure 5.11, when the projectile leaves the barrel, it creates an expanding vortex behind it. The vortex keeps expanding until it reaches maximum dispersion, after which it starts to diminish. However, although the particles get trapped in that vortex, the majority of them still do not have sufficient time to cool despite the increased flight time. This suggests that the residues found at distances around 50 cm from the firearm are either experiencing a higher temperature effect or are travelling at a higher velocity than the particles found closer to the firearm, and therefore do not have sufficient time to cool prior to hitting the substrates. The travelling of particles in the firearm discharge plume is also responsible for the different splat angles seen in Figure 5.6. Although some particles maintain a fairly straight flight path resulting in normal incidence splats, others get trapped in the vortex that is created, resulting in a change in their directionality, and therefore impacting the substrate at an angle. Moreover, the spherical particles that were found at these distances were smaller than 3 µm, which supports the aforementioned hypothesis as small, spheroidal particles would have had the chance to cool because of their small volume. To first order, the relative particle cooling time is a function of the volume of a particle, and thus is 8 times faster for a particle with half the diameter (see Chapter 8 for detailed analysis of in-flight cooling times). On the other hand, the larger particles would not have had the chance to cool because of their added size, resulting in their disruption upon impact.

The residues found closest to the firearm also consist of smaller particles in comparison to those further down the firing range. It is postulated that the residues present here are as a result of a high velocity stream of particles that leaves the muzzle, labelled 'A' in Figure 5.11. Upon the bullet exiting the barrel, small, high velocity particles burst out the muzzle due to the build-up of pressure that the ignition process created. Despite their small size, not all of the particles have had sufficient time to cool prior to reaching the first substrates at 10 cm and 20 cm due to the speed at which they are travelling at. As a result, the particles closest to the firearm either have not had enough time to cool (hence the abundance of class 2 molten-like residues at these distances) or they have had adequate time to cool, but the insufficient flight time has not allowed them to develop into spheres, resulting in the high number of irregular, class 5 IDGSR particles (Table 5.1). This is further reinforced by the fact that at the

distances farthest from the firearm, there is a gradual increase in more semi-congealed and solidified residues, as well as the characteristic spherical GSR.

5.4.2 Elemental Composition Analysis

Upon examination of the elemental composition of the different particle classes, it can be seen that the more liquid the appearance of the particle, the higher the lead content of said particle appears to be, with a smaller standard deviation (Table 5.2). Conversely, the barium content seems to increase as the particles become more solidified. Antimony and copper both show a slight decrease as the residues become more structured and solid. However, as multiple particles throughout the sampling range were analysed, it appeared that these particles were all fairly antimony-poor. Upon EDX analysis of the cartridge case and primer, it was determined that the primer mixture itself contained no antimony. In fact, the presence of antimony in the samples was due to the projectile itself. Rather than just lead, the core of the projectile actually consisted of 'hardened' lead, which is achieved by doping lead with antimony, and so the trace amounts of antimony identified actually originated from there.

It would appear that some anomalous particles have influenced these results, leading to larger than average error. This is due to particles with high concentrations of a particular element (usually lead) skewing the results. Nevertheless, a change in the compositional ratios in these particles could influence their structural morphology, therefore, suggesting that the ratio of the elemental composition may also influence a particle's structure, in conjunction with in-flight cooling time. Although Burnett B. (1989) does not provide detailed information regarding the elemental composition of the 'splattered' morphologies observed, Ilker K. et al. (2015) suggests that elemental composition is highly influential on the morphology of particles. However, looking at the elemental composition results displayed in the tetrahedral plots in Figure 5.9, it appears that there is very little variation in the individual particle morphologies, with very few particles deviating from the 100 % lead corner. This could suggest that the primary difference for the differing morphologies may lie within the internal structure of particles or incomplete in-flight cooling.

5.5 Investigating organic composition variations on individual particle populations using Raman spectrometry

After the examination of individual GSR particles using FEG-SEM/EDX, a range of morphologies was observed. To further understand these morphological variations, the organic content of different splat populations was investigated. By studying variations in particles' organic compositions, it could possibly determine whether the organic content of the particles could influence the different morphologies observed (i.e. does a molten class 0 IDGSR have a higher organic content than a class 7 sphere?). To investigate this, Raman spectrometry was used as metals do not generally give Raman signals, and so the organic content can be investigated without interference. Dalby O. et al. (2010) produced a comprehensive list of organic compounds associated with smokeless powder and GSR that has been expanded on over the years (Taudte R.V. et al. (2014); O'Mahony A.M. & Wang J. (2013)). Goudsmits E. et al. (2015) compared the compounds listed in the literature against several experimental studies of OGSR and found 136 organic compounds that could be associated with GSR.

Raman spectroscopy was first reported to be used for OGSR analysis in 2012, where it successfully detected several OGSR components, including as methyl centralite, ethyl centralite, dinitrotoluene, diphenylamine and its nitration products (Lopez-Lopez M. et al. (2012); Bueno J. et al. (2012)). By employing the use of Raman spectroscopy, OGSR spectra have been reported to closely resemble those of unfired ammunition, enabling OGSR to be traced back to the ammunition used (Lopez-Lopez M. et al. (2012); Bueno J. et al. (2012), Bueno J. et al. (2013)), as shown in Figure 5.12. Additionally, materials that may be mistaken for OGSR (such as sand or black ballpoint ink) could also be distinguished, further reinforcing the capabilities of Raman analyses (Lopez-Lopez M. et al., 2012).

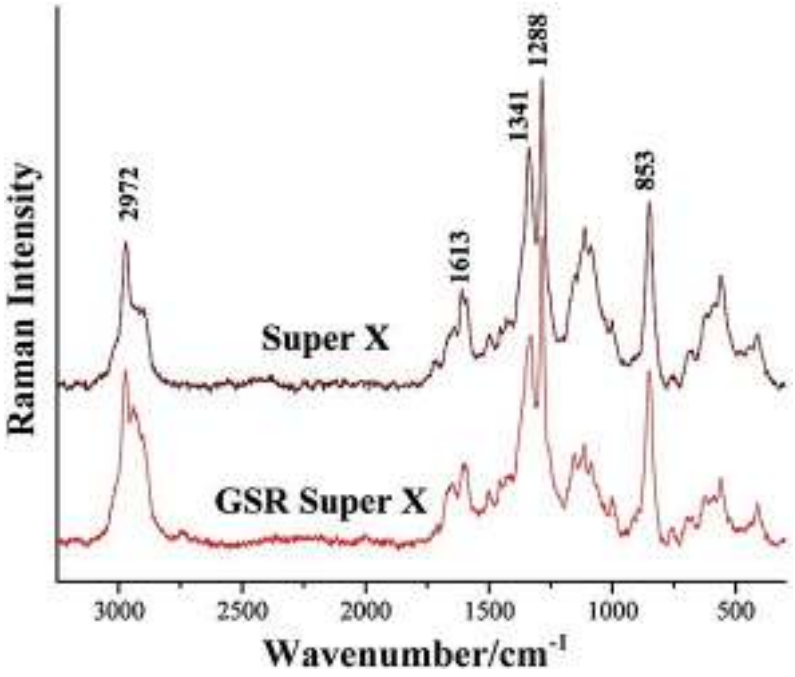

Figure 5.12: Raman spectra of a propellant and its respective GSR from an unfired cartridge by Lopez-Lopez M. et al. (2012) showing the close resemblance between the two spectra which allows for links between OGSR and the ammunition it originated from to be determined using Raman spectroscopy.

There are many advantages to using Raman spectroscopy to investigate OGSR. The first, and arguably the most important when dealing with forensic evidence, advantage is the (mostly) non-destructive nature of Raman analyses where only a small sample size is required. Moreover, little sample preparation is required prior to analysis, which is also reasonably quick to do, depending on whether GSR particle identification is carried out manually using an optical microscope, or through the development of automated image-recognition software (Abrego Z. et al. (2014); Goudsmits E. et al. (2015)) and automated Raman mapping (Bueno J. & Lednev I.K., 2014).

Overall, a standard methodology for the collection, extraction and analysis of OGSR has not yet been established (Goudsmits E. et al., 2015), and despite further development needed to optimise OGSR analyses, Raman spectroscopy can still be used as a confirmatory technique. Raman spectroscopy can be used to distinguish between different chemical and/or molecular compositions by visual, statistical or spectral library comparisons (Doty K.C. et al., 2016). Statistical treatment of GSR analytical data is increasingly being employed (Bueno J. & Lednev I.K. (2013); Lopez-Lopez M. et al. (2012); Bueno J. et al. (2012)), and has provided highly accurate identifications for firearm and ammunition combinations. However, Raman spectroscopy was only touched upon during this thesis as this investigation primarily focuses on inorganic GSR analyses. After successfully discriminating between two ammuntion types based

on their stabilizers, Lopez-Lopez M. et al. (2012) demonstrated the potential of Raman spectroscopy as a complementary analytical technique to SEM/EDX for the forensic analysis of GSR. By employing Raman spectroscopy as a supplementary technique, the premise was to determine whether any substantial organic variations can be discerned between spheroidal and IDGSR particles.

Prior to Raman analysis of the samples, the appropriate laser for the analysis of these specific samples needed to be determined. To investigate this, a class 3 IDGSR particle was chosen and a spectrum was taken using the four available lasers: red (633 nm), blue (473 nm), green (532 nm) and infrared (784 nm). The results are displayed in Figure 5.13.

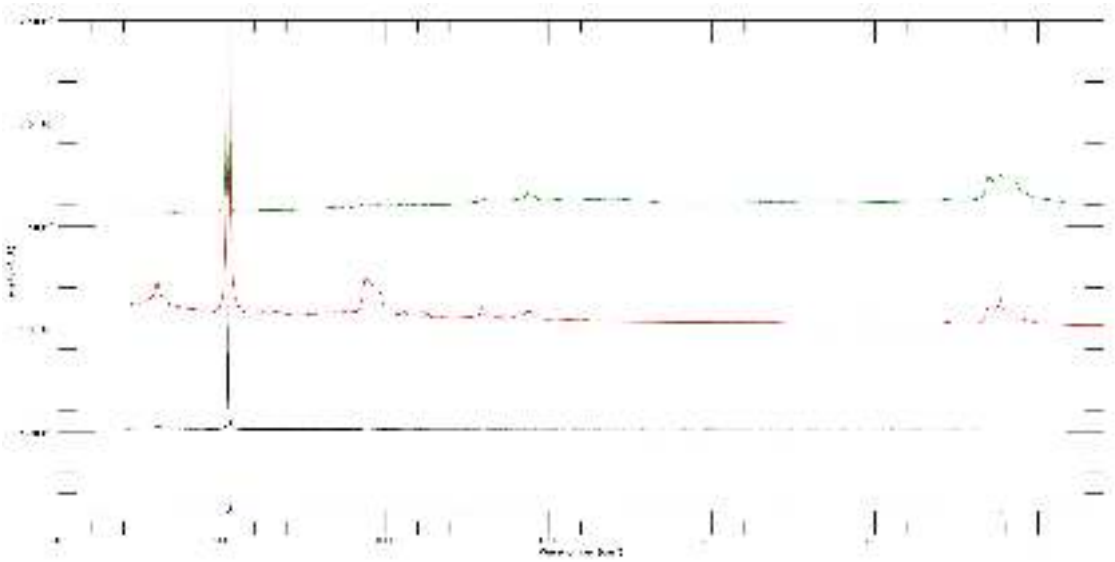

Figure 5.13: Raman spectra of the same IDGSR particle on the silicon 3 substrate demonstrating the variation in peak detection. The four lasers used were blue (shown as blue), infrared (shown as black), red (shown as red) and green (shown as green). Note: the CCD on the Raman spectrometer is insensitive to $> 2800\,\text{cm}^{-1}$ when the infrared laser is used.

As it can be seen in Figure 5.13, the red laser provided the most detailed spectrum with clearly distinguishable peaks. Therefore, this was chosen as the laser to be used for the analysis of these samples.

5.6 Materials & Methodology

To determine whether there was any variation in the organic content of GSR particles, silicon-3 (40 cm from the firearm) was used. This sample contained a large number

of particles, therefore it was easy to obtain a range of data from residues of varying morphologies. A fragment of a high grade, optically polished, silicon wafer was used to calibrate the Raman prior to analysis due to its strong Raman peak at 520.6 cm^{-1}. As the substrates were also optically polished silicon wafers, the samples could be placed directly into the Raman chamber for analysis. The Raman spectrometer that was used for the analyses of the samples was a Horiba LabRam-HR in conjunction with the LabSpec-6 software.

5.6.1 Analytical Methodology

An area of the silicon 3 sample was set up to be mapped using the ×10 magnification objective, the area of which is shown in Figure 5.14. A selection of spheroidal, disaggregated, and molten-looking particles were randomly selected from the list of particles that were previously examined using FEG-SEM/EDX.

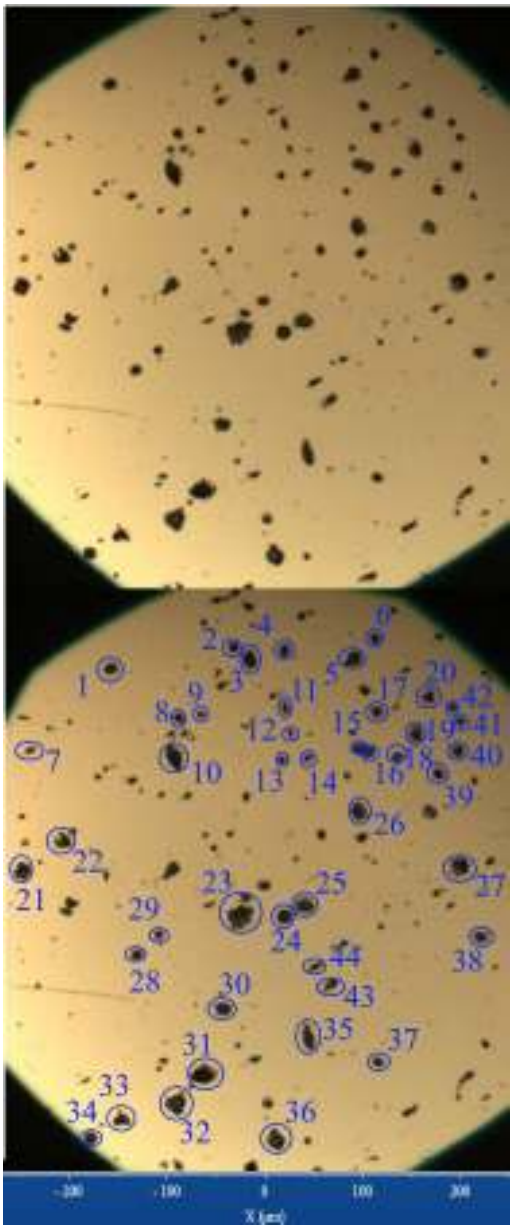

Figure 5.14: Picture of the silicon 3 area that was mapped using the Raman Spectrometer using a ×10 magnification objective. The numbers attached to each particle represent the order in which they were analysed and correspond to the relevant spectrum.

5.7 Results

The results for the overall spectrum of the silicon-3 area map are shown below in Figure 5.15. Table 5.3 presents the same map data in tabular form, specifying the morphology of the residues examined, along with whether any organic signatures were present. The

particles that display any peaks other than the background silicon peaks are displayed in Figure 5.16.

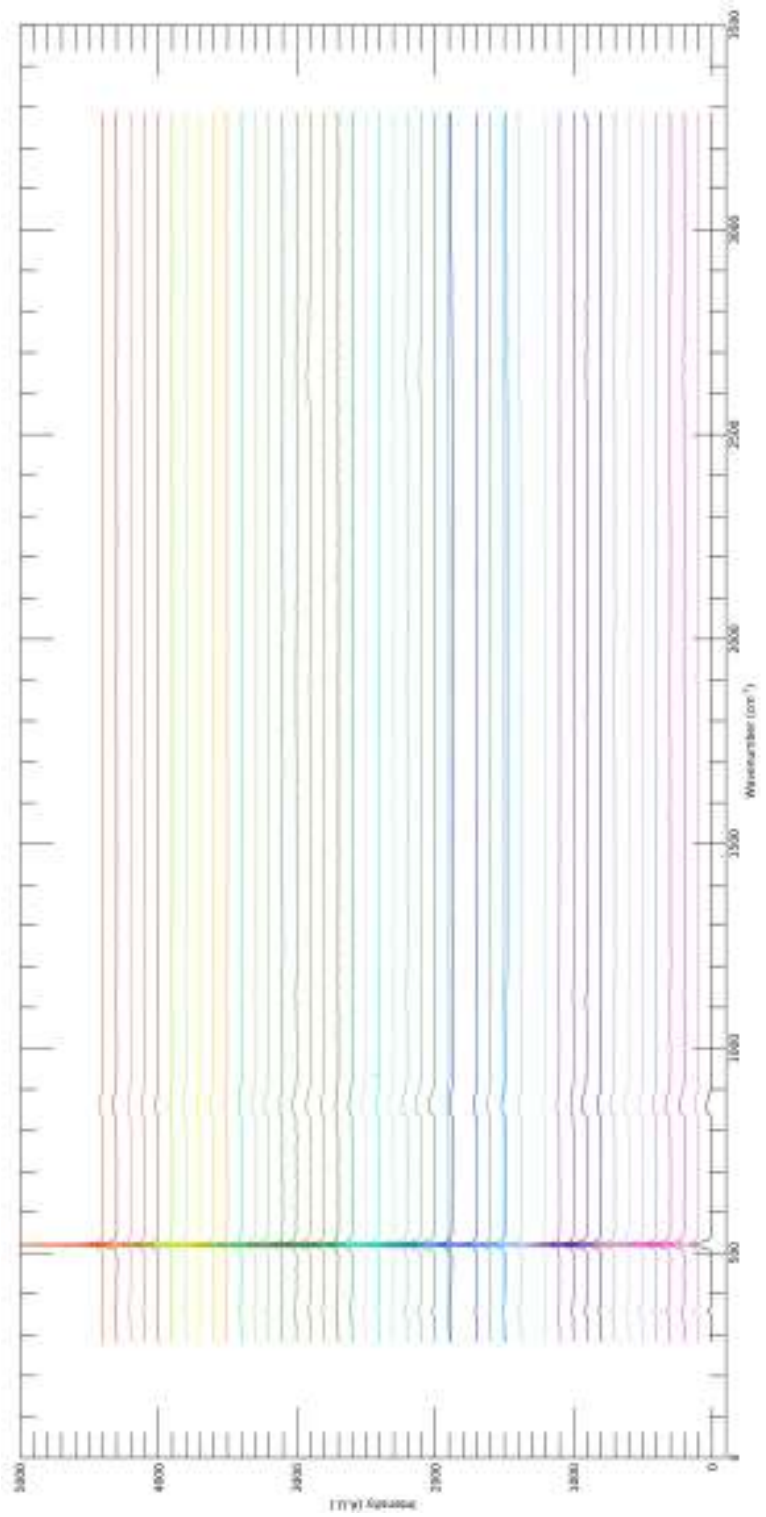

Figure 5.15: Raman spectra of the individual residues from the silicon 3 map. The spectra are in increasing number - with particle 1 being at the bottom and particle 44 being the top spectrum.

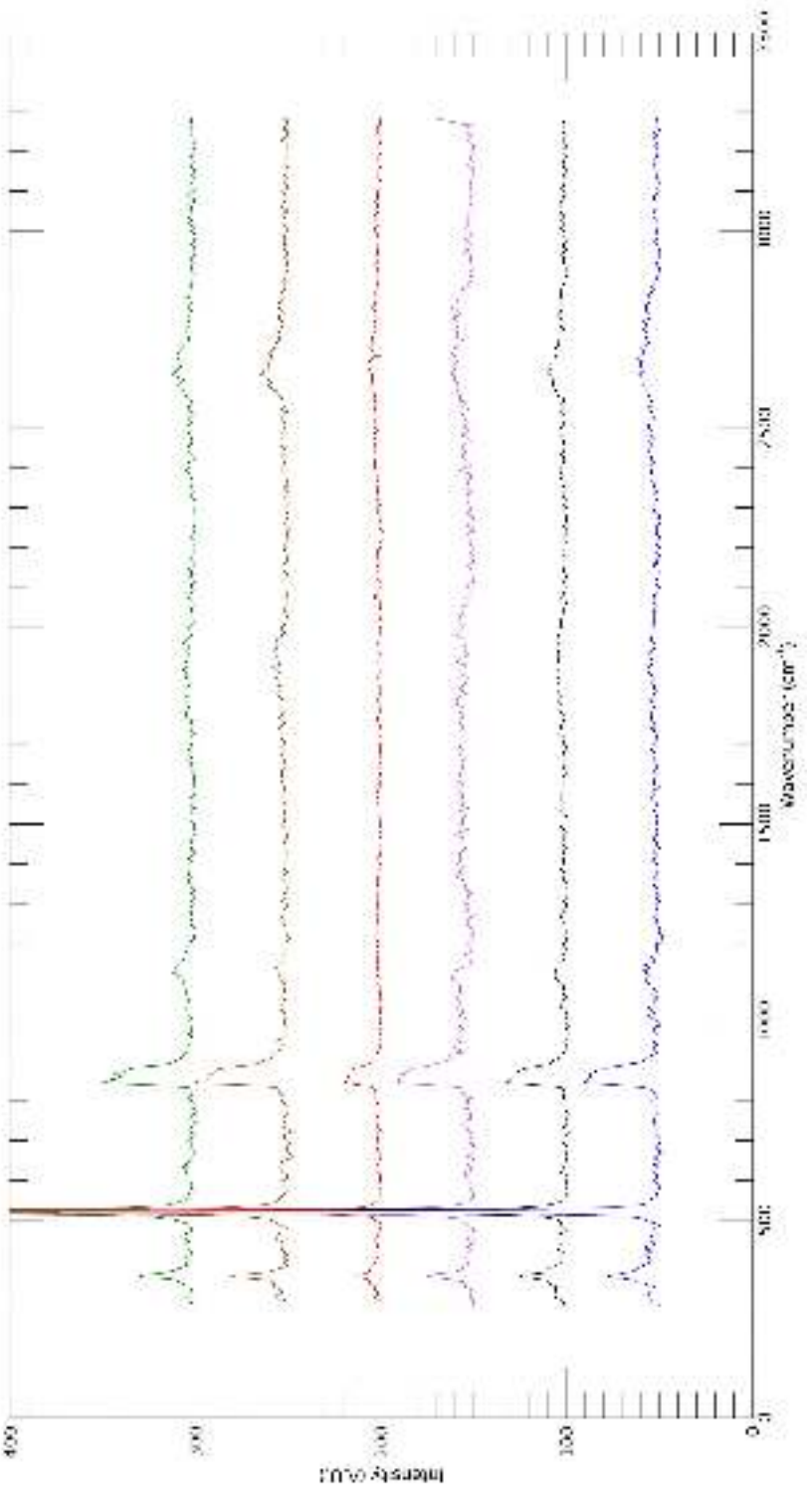

Figure 5.16: Raman spectra of the individual residues showing the organic C-H bump at $\sim 2800\,\mathrm{cm}^{-1}$ - $3500\,\mathrm{cm}^{-1}$. The particles whose spectra are displayed here are (bottom to top): particle 4, particle 6, particle 10, particle 20, particle 21 and particle 22.

Table 5.3: Table showing the results obtained from the silicon 3 area map using the Raman spectrometer. The 'particle number' corresponds to the appropriately labelled particle in Figure 5.14 and 'organic signature' refers to whether the C-H bump at $\sim$ 2800 cm^{-1} - 3500 cm^{-1} is present in each individual particle spectrum. Due to the low magnification objectives used and resolution of the Raman Spectrometer, the extent of melting could not be sufficiently discerned to classify the particles into their appropriate classes. Instead, two general classes were adopted for this section. Sphere: spheroidal particles that showed no melting, IDGSR: particles that have disaggregated on impact or show partial melting at $\times$50 magnification.

Particle Number	Morphology	Organic Signature
1	IDGSR	No
2	Sphere	No
3	IDGSR	No
4	IDGSR	Yes
5	IDGSR	No
6	Sphere	Yes
7	IDGSR	Yes
8	IDGSR	Yes
9	Sphere	No
10	IDGSR	Yes
11	IDGSR	No
12	IDGSR	No
13	Sphere	No
14	IDGSR	No
15	IDGSR	No
16	IDGSR	No
17	IDGSR	No
18	IDGSR	No
19	IDGSR	No
20	IDGSR	Yes
21	IDGSR	Yes
22	IDGSR	Yes
23	IDGSR	Yes
24	Sphere	Yes
25	IDGSR	No
26	IDGSR	No
27	IDGSR	No
28	IDGSR	No
29	Sphere	Yes
30	IDGSR	No
31	IDGSR	No
32	IDGSR	Yes
33	IDGSR	No
34	Sphere	No
35	IDGSR	No
36	IDGSR	No
37	IDGSR	No
38	IDGSR	No
39	Sphere	No
40	Sphere	No
41	Sphere	No
42	Sphere	No
43	IDGSR	Yes
44	IDGSR	No

Upon acquiring the spectrum of each particle during the mapping process, it was clear that the multitude of peaks observed during the laser tests were not seen in the map spectra. A hypothesis for the absence of these peaks was the fact that the $\times$10 objective was used. Due to the low magnification and the small size of the particles,

it is possible that the signal-to-noise ratio for the peaks corresponding to the residues was too low and so were swamped by the background. In order to test this, an IDGSR particle was analysed using both the ×10 and ×50 objective. The results are displayed in Figure 5.17.

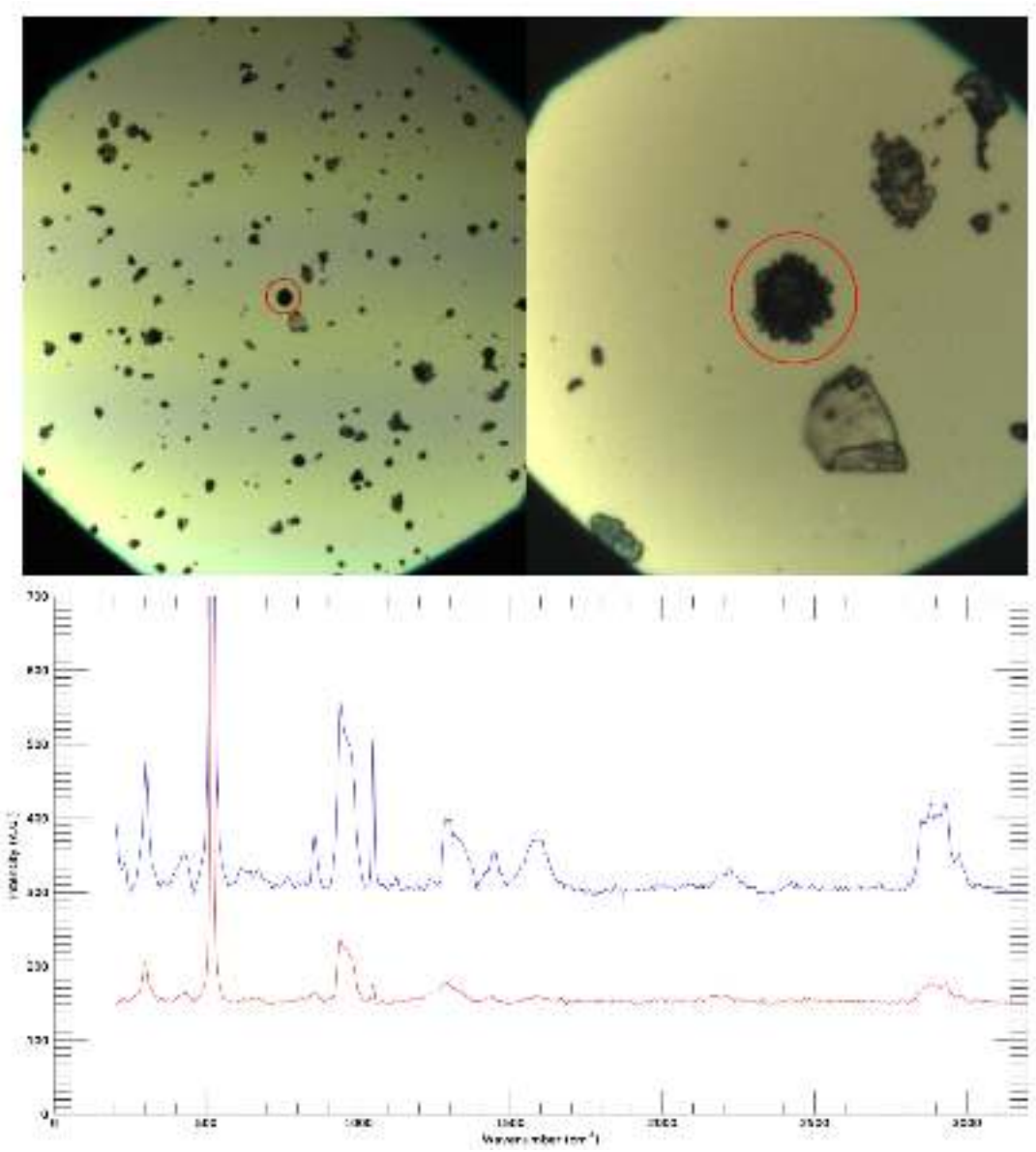

Figure 5.17: Raman spectra of an IDGSR particle using both the × 10 objective (left) and × 50 objective (right). The red spectrum corresponds to the × 10 objective and the blue corresponds to the × 50 objective.

As it can be seen in Figure 5.17, the spectrum with the ×10 objective varies significantly to the one acquired using the ×50 objective. Therefore, a selection of particles consisting of both IDGSR splats and spheres were analysed using the ×50 objective, thereby focusing better on the residues and reducing the effect the background has on

the spectra. The resulting spectra are displayed in Figure 5.18.

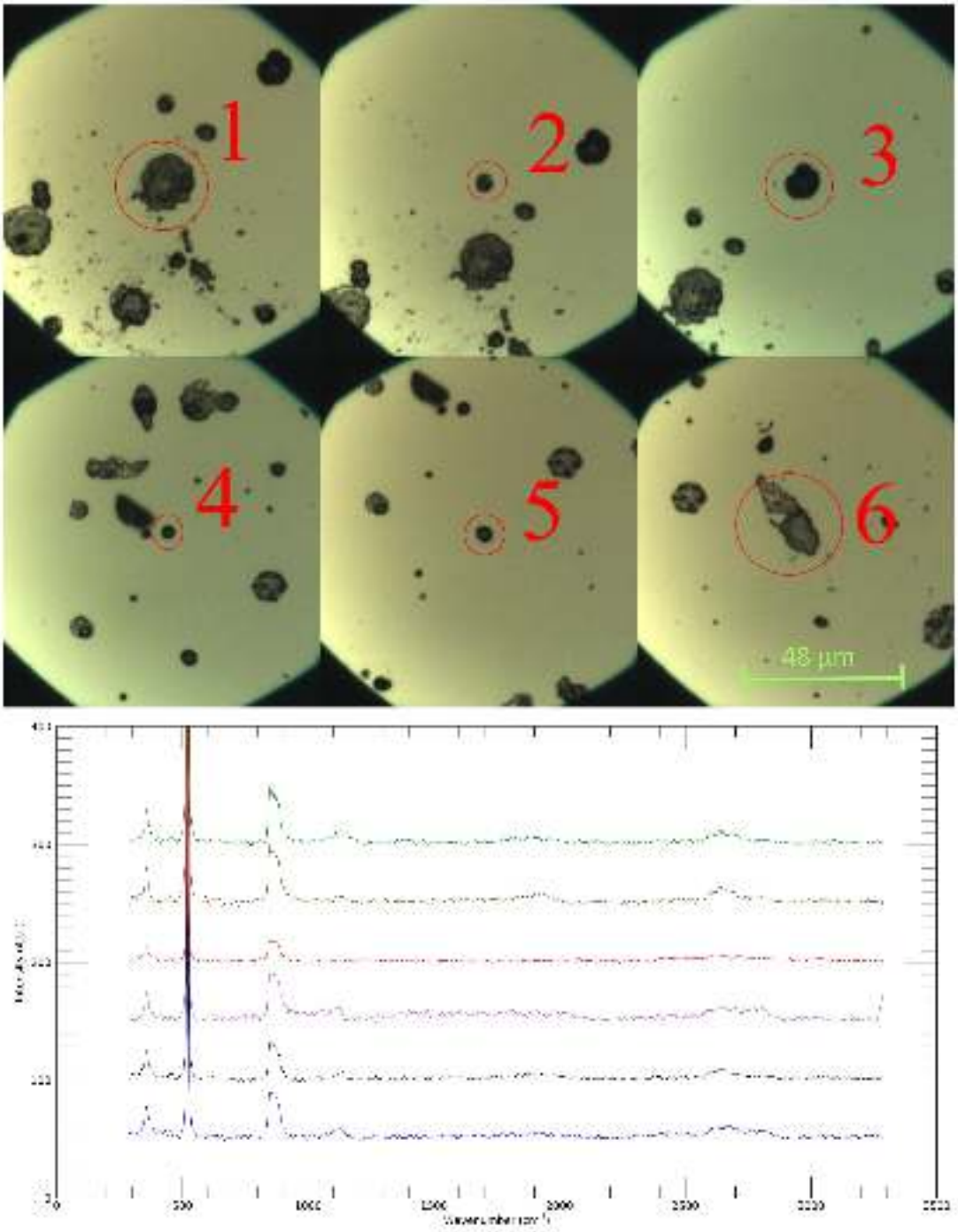

Figure 5.18: Raman spectra of the individual residues using the ×50 objective, showing that a larger number of peaks are visible, along with the organic C-H bump at $\sim 2800\,\mathrm{cm}^{-1}$. The spectra corresponding to each particle are (bottom to top): particle 1, particle 2, particle 3, particle 4, particle 5 and particle 6. The scale on the bottom right applies to all six particles.

A line map across an individual IDGSR particle was also acquired to determine

whether the organic content varies, or is maintained consistently throughout the particle (Figure 5.19).

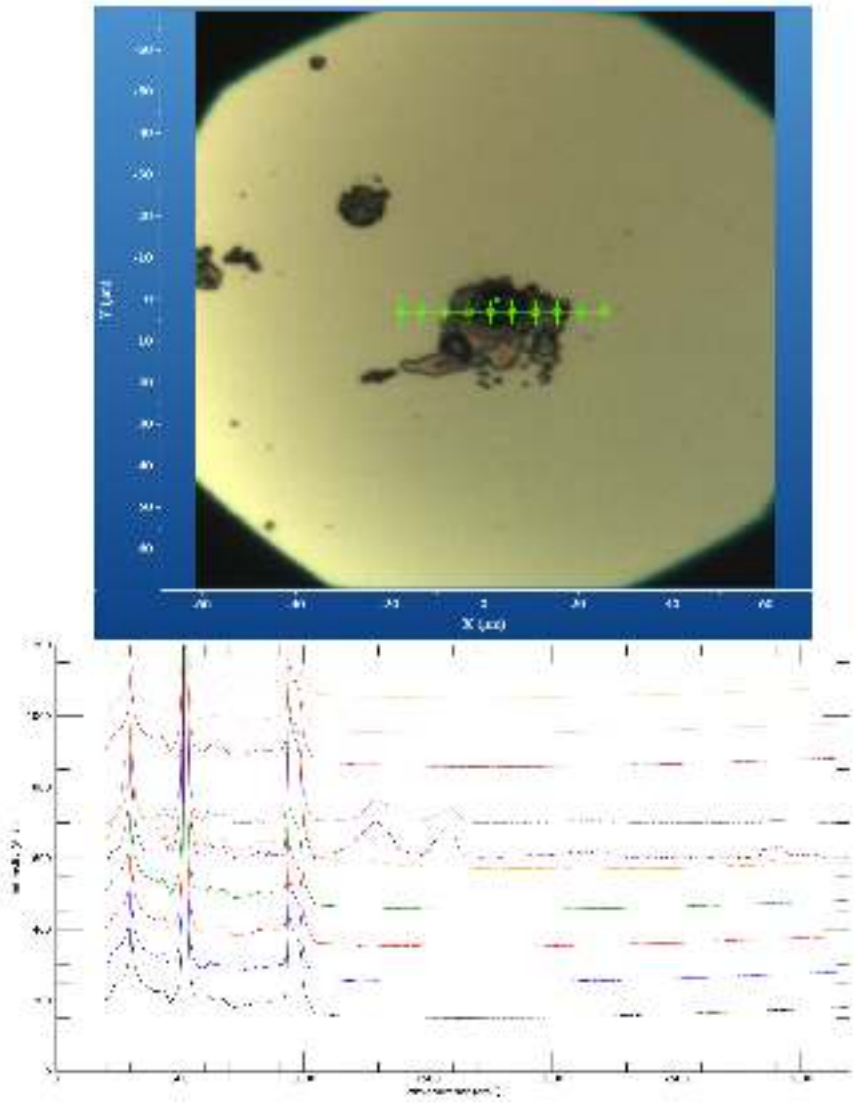

Figure 5.19: Raman spectra of an IDGSR particle using the ×50 objective, showing the variations in organic content along the green line. The step between each point of acquisition was 4.8 µm. The bottom spectrum is the left, moving right across the particle.

5.8 Discussion

As it can be seen from the results presented in this section, despite these residues consisting of primarily inorganic, metallic residues, organic signatures were also iden-

tified using Raman spectrometry. The characteristic C-H bond can be seen in the $\sim$ 2800 cm^{-1} region (or 2972 cm^{-1} in Figure 5.12), along with the prominent lead sulphate ($PbSO_4$) peak at $\sim$ 983 cm^{-1}, originating from the primer (Doty K.C. & Lednev I.K., 2018). In comparing these spectra to those obtained by Lopez-Lopez M. et al. (2012), it can be seen that the band at 1342 cm^{-1} is characteristic of gunpowders with diphenylamine as part of their primary composition.

Looking at the results in Table 5.3, it can be seen that the morphology of the particle (i.e. sphere vs. IDGSR splat) is not definitive as to whether organic signatures will be identified in the residues. However, looking at Figure 5.18 and Figure 5.19, it is made apparent that organic signatures are identified when a particle (be it spheroidal or splat-like) appears darker, or more dense. The reason for this is probably due to the Raman itself. As the IDGSR residues often have very thin, film-like morphologies, the laser often penetrates through them, thereby overlooking potential organic signatures. However, some parts of IDGSR particles (as well as spheres) are more 'dense' and therefore the laser can pick up more spectral signals. This is made clear in Figure 5.19 where, although the majority of the points at which spectra were acquired from are on the IDGSR particle itself, it is not until the laser reaches the darker 'clump' in the centre that a detailed spectrum is produced.

Another point of consideration is the magnification at which maps and spectra are obtained. Figure 5.16 shows rather small C-H bumps at $\sim$ 2800 cm^{-1}, largely due to the $\times$10 objective. Upon using a higher magnification objective (Figure 5.18) it can be seen that a number of peaks that previously went unidentified are now clearly discerned from the background.

Raman spectroscopy clearly has great potential to enhance the analyses of GSR, particularly with regards to organic compounds. These analyses showed that the chemical signature of a particle can vary across it primarily due to residue thickness and composition. A complementary Raman and SEM/EDX approach would be a useful tool as organic compounds and inorganic residues could be detected from the same particles within the same sample. However, as no clear difference in the organic content of molten-like residues and spheroidal particles was discerned, no further organic analyses were undertaken.

Chapter 6

Experiment 3: Investigating GSRs From Centre-fire Ammunition

After the successful collection, identification and sub-micron analyses of GSR particles using rim-fire ammunition, the investigation progressed into determining whether the phenomena encountered in Chapter 4 were also observed using centre-fire ammunition. This investigation was made possible by the gentlemen of Kent Police, Maidstone, who spent a day carrying out test firings in the name of science.

6.1 Introduction

Centre-fire ammunition, as discussed in Chapter 2, is when a cartridge has the primer located in the centre of its base rather than around the rim (Figure 2.1). Due to the higher amount of energy that centre-fire ammunition produces, its primary uses pertain to defence and big game hunting (Simmons M., 2020). It is therefore unsurprising that this type of ammunition (in accordance with the appropriate firearm) would be the choice for heavy duty police defence weaponry. Both firearms that were used in this set of experiments were standard issued firearms used by Kent Police armed forces.

The first firearm to be used was the Heckler & Koch G36 Carbine firearm (henceforth referred to as 'G36C') with 5.56 mm Federal Premium tactical bonded FMJ am-

munition (Figure 6.1). This assault rifle is the primary weapon choice for law enforcement and military agencies in over 40 countries, including the United Kingdom. The use of this firearm and ammunition combination was employed for Experiment 3.1.

The second firearm to be used was the Accuracy International AX308 firearm (henceforth referred to as 'AX308') with 7.62 mm Federal tactical bonded semi-jacketed ammunition (Figure 6.2). This sniper rifle is a popular choice amongst special forces worldwide, including the United Kingdom. The use of this firearm and ammunition combination was employed for Experiment 3.2. Table 6.1 displays the specifications of both firearms.

Table 6.1: Table comparing the Heckler & Koch G36 Carbine (Heckler & Koch GmbH) and Accuracy International AX308 Accuracy International Ltd firearms that were used as part of Experiments 3.1 and 3.2 respectively.

Technical Data	Heckler & Koch G36 Carbine	Accuracy International AX308
General		
Calibre	5.56 x 45 mm NATO	7.62 x 51 mm NATO
Operating Principle	Gas-operated	Bolt-action
Magazine Capacity	30 rounds	10 rounds
Modes of Fire	0-1-2-D	Single shot
Sights	Mechanical by default but various sights can be mounted	None, accessory rail provided for various sight mounting
Buttstock	Foldable	Foldable
Muzzle Velocity	722 ms^{-1}	783 ms^{-1}
Dimensions		
Length (min./max.)	Approx. 500/716 mm	Approx. 940/1155 mm
Width	Approx. 63 mm	Approx. 180 mm
Height	Approx. 277 mm	Approx. 100 mm
Barrel Length	Approx. 228 mm	Approx. 610 mm
Weight		
Weapon (without magazine)	Approx. 2988 g	Approx. 6200 g
Magazine (empty magazine)	Approx. 140 g	Approx. 236 g

The AX308 is originally chambered to use .308 Winchester ammunition (named after its calibre, and henceforth referred to as 308Winchester) rather than the 7.62 $\times$ 51 mm NATO ammunition used by Kent Police. The 308Winchester cartridge is a smokeless powder, rimless, bottlenecked, rifle cartridge housing a bullet with a 0.308″(308 cal, 7.8 mm) diameter (Figure 6.3). In 1952, Winchester introduced this ammunition as a civilian model of the late T65 series designs (Hildebrand G., 2005) due to demand in the commercial hunting market. Since its release it has become the most popular short-action, big-game hunting cartridge worldwide (Simpson L., 2000). Two years later, the T65E5 experimental cartridge iteration was adopted by NATO, under the 7.62 $\times$ 51 mm NATO designation, as a standard for small arms amongst NATO countries. Although these two models are similar (as seen in Figure 6.3), they are not

Figure 6.1: Annotated picture of the 5.56 mm Heckler & Koch G36 Carbine assault rifle, courtesy of Kent Police. Full specifications for this firearm can be found in Table 6.1.

Figure 6.2: Annotated picture of the 7.62 mm Accuracy International AX308 sniper rifle, courtesy of Kent Police. Full specifications for this firearm can be found in Table 6.1.

identical, with the 7.62 × 51 mm NATO cartridge often having a thicker cartridge wall (Redgwell S., 2001). Moreover, the 308Winchester cartridges are typically loaded to higher pressures, with the North American Sporting Arms and Ammunition Manufacturers' Institute (SAAMI) maximum pressure for the 308Winchester being 427.47 MPa (Sporting Arms and Ammunition Manufacturers' Institute Inc, 2013). In C.I.P. regulated countries (Commission Internationale Permanente pour l'Epreuve des Armes à Feu Portatives, i.e. Permanent International Commission for the Proof of Small Arms), of which the United Kingdom is a member state, every rifle and cartridge combination has to be proofed at 125% of the maximum pressure to certify for sale, meaning the 308Winchester chambered firearms within the C.I.P. member states are proof tested at 519 MPa. This varies significantly from the 7.62 × 51 mm NATO cartridge whose maximum pressure does not exceed 415 MPa (Ministry of Defence United Kingdom, 2005). However, despite these minor differences, they can be loaded into rifles chambered for the other round and their interchange is considered safe by SAAMI (Sporting Arms and Ammunition Manufacturers' Institute Inc, 2012). Therefore, the use of a 7.62 × 51 mm NATO cartridge in a firearm chambered for .308 Winchester cartridges is effectively safe.

Figure 6.3: Picture (courtesy of Rated Red, Nashville) of a 308Winchester (right) and 7.62 × 51 mm NATO designated cartridge (left). Due to their very slight differences, these cartridges are difficult to differentiate based solely on their appearance.

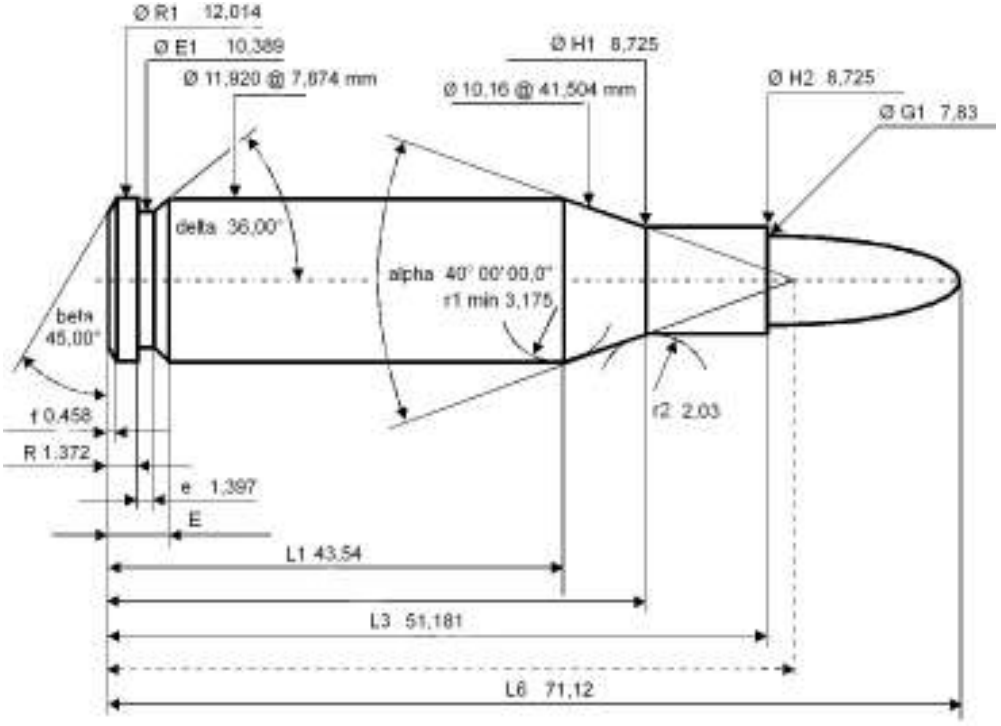

7.62×51mm NATO cartridge dimensions

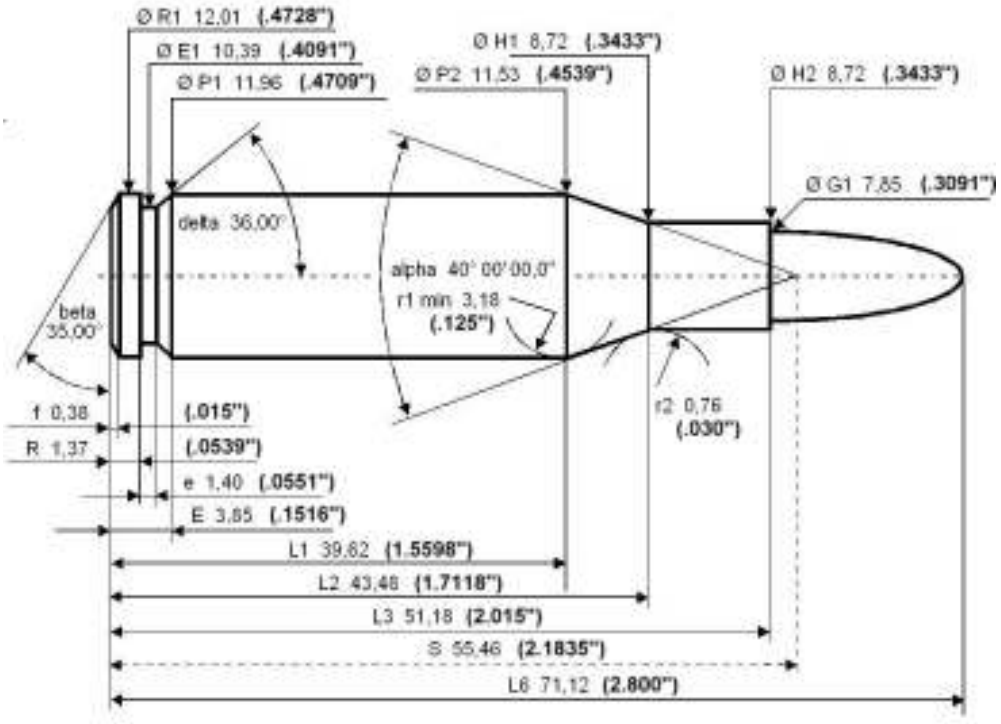

.308 Winchester maximum C.I.P. cartridge dimensions

Figure 6.4: Annotated diagrams (courtesy of Francis Flinch using the information provided by EOD (1966)) of a 308Winchester (right) and 7.62 × 51 mm NATO designated cartridge (left). All dimensions are in millimetres, with inches included for the .308 Winchester cartridge.

The muzzle velocities for both firearms were investigated as part of these experiments and compared to the literature values stated in Table 6.1.

6.2 Materials & Methodology

In order to make accurate comparisons between the effects of rim-fire and centre-fire ammunition, both Experiments 1 and 2 were replicated with the centre-fire firearm and ammunition combinations. Firstly, the carbon double-sided adhesive tape collection substrates were used to collect particles for automated and individual particle analyses, while the high purity, silicon wafer targets were mainly used in an attempt to ascertain the velocities at which the particles may have been travelling at once they were expelled from the muzzle of the firearm.

6.2.1 Experimental Set-up

A range of distances were sampled, starting at 0 cm from the firearm and reaching up to a distance of 400 cm, increasing in 25 cm increments. At 0 cm from the firearm the substrates were directly adjacent to one another, whereas at 25 cm they were 12 cm apart. At each sampling distance after this, the spacing between the targets was decreased by 1 cm. The rationale behind this set-up was that closest to the firearm the discharge plume expelled upon firing would be at its maximum before tunnelling down the centre of the firing range. Therefore, as the residues fly down the trajectory path, by setting the targets slightly off-centre at each distance, it prevented a shielding effect. For this part of the experiment, double-sided carbon adhesive tape on aluminium stubs were used. As seen in Figure 6.5, one stub was placed horizontally down the centre of the firing range whereas the other substrates were attached to metal brackets mounted onto a metal bar for stability. This allowed for a perpendicular sampling angle for maximum residue collection. Three consecutive shots were taken per firearm-ammunition combination.

In the second part of the test firing, silicon substrates sized approximately 15 mm $\times$ 20 mm were placed down the centre of the firing line at 0 cm, 20 cm, 40 cm, 60 cm, 80 cm, 100 cm, 125 cm, 150 cm, 200 cm, 300 cm and 400 cm from the firearm (Figure 6.6). The height of the firearm was maintained at approximately 20 cm from the base of the table for both experiments.

A Shooting Chrony M1 chronograph (Figure 6.7) was used to determine the velocity at which the projectiles were travelling through the air for each firearm. The

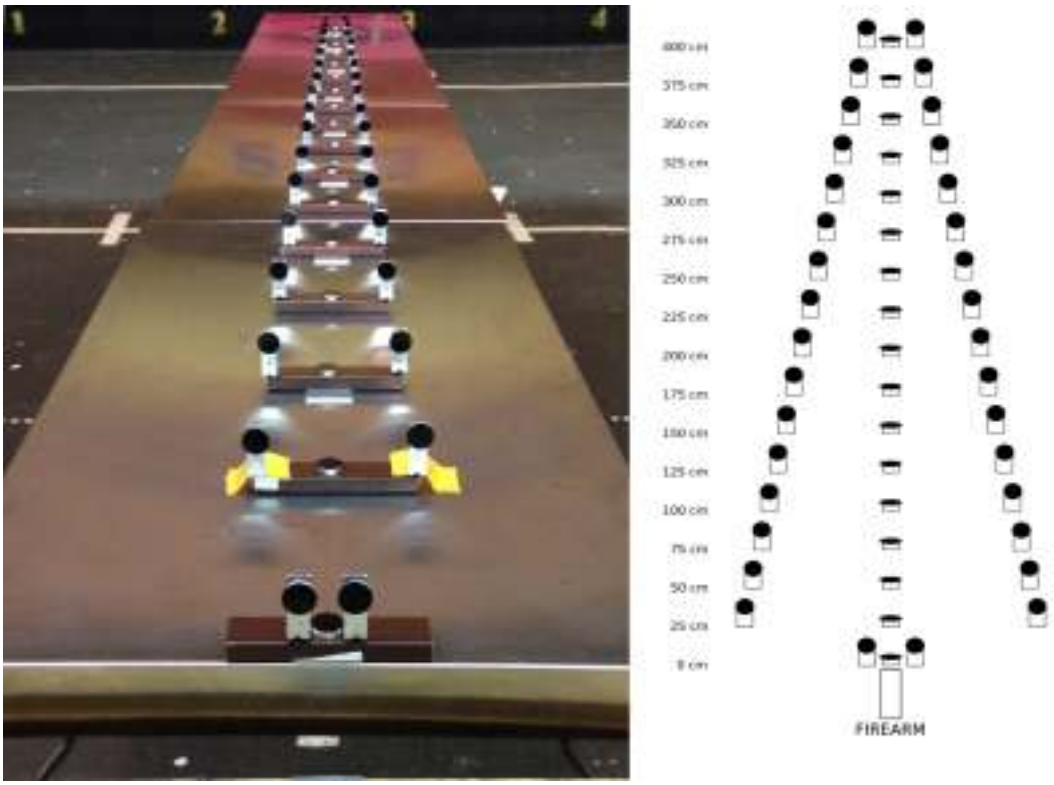

Figure 6.5: Picture and diagram (not to scale) showing the set up of the aluminium stub targets for the test firings carried out by Kent Police using both centre-fire weapon and ammunition combinations. At each distance from 25 cm onwards the spacing between the outer aluminium substrates was decreased by 1 cm, 0.5 cm from each side.

Figure 6.6: Diagram (not to scale) showing a side-view schematic of the polished silicon wafer targets for the centre-fire test firings carried out by Kent Police using both centre-fire weapon and ammunition combinations.

chronograph was set up at approximately 1 m away from the firearms and three shots were fired with each weapon.

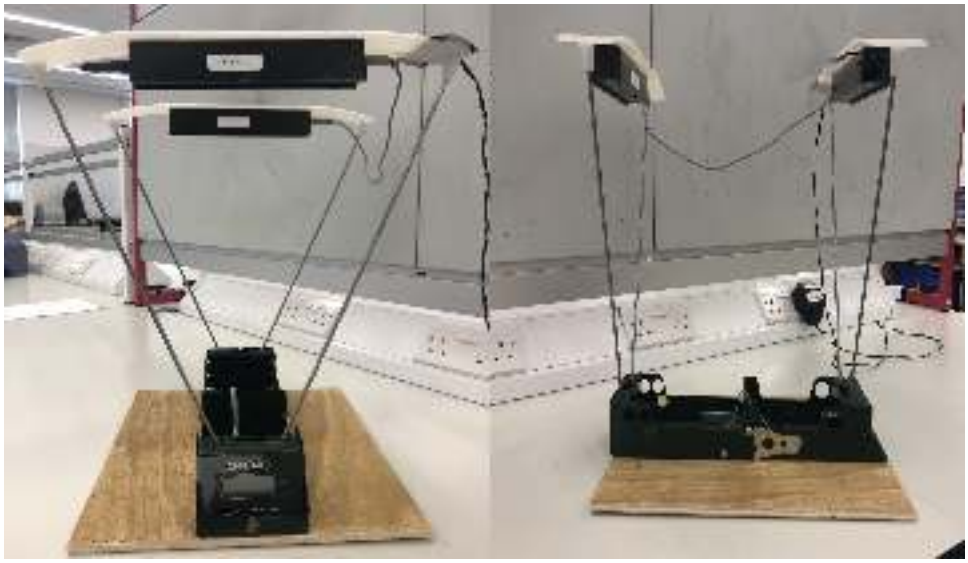

Figure 6.7: Picture of the Shooting Chrony M1 chronograph used during the test firings. It was used to determine the velocity which the projectiles were travelling at from their respective firearms.

6.2.2 Analytical Methodology

Pictures of all the targets were taken using a Nikon D3000 camera. The carbon adhesive tape targets were analysed using the INCA GSR automated software on the SEM/EDX, whereas for individual particle analyses, both the carbon adhesive tape and silicon targets were examined under the FEG-SEM/EDX (see Chapter 4). A random selection process was adopted for the individual particle identification and analysis which encompassed the entire sample to ensure a representative examination of each substrate.

6.3 Results

Upon initial examination of the carbon adhesive tape substrates, there appeared to be clear heat damage (Figure 6.8). The damage can be seen with both firearms across the entire sampling range, but began to decrease approximately after the 250 cm mark. Despite the damage being consistently present with both firearms, it appeared to be more extensive when using the AX308.

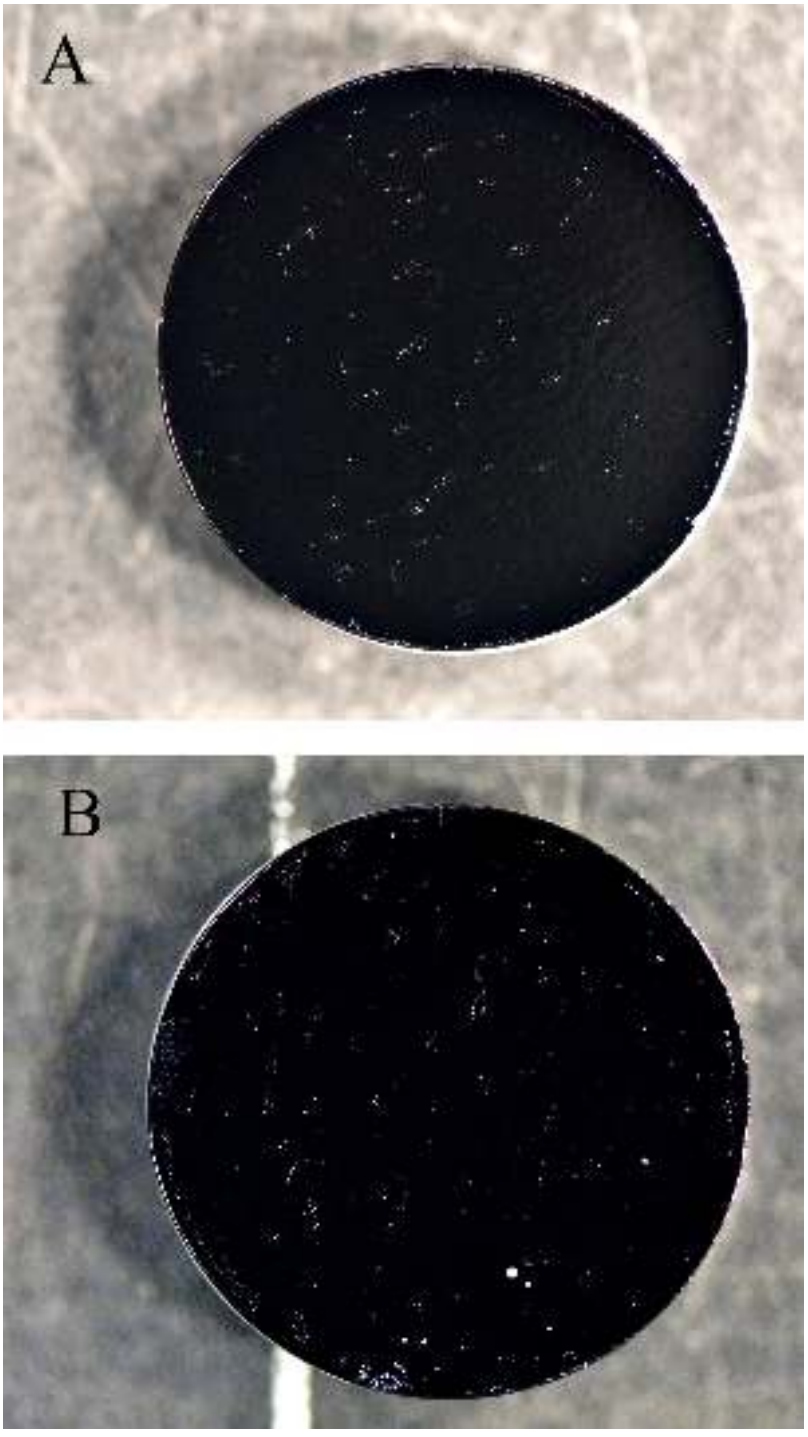

Figure 6.8: Pictures of the heat damage experienced by the carbon adhesive tape substrates using the two different centre-fire firearm and ammunition combinations. The heat damage looks like angular tears and bubbles (circular tears) on the carbon adhesive tape which allow for the Al stub to shine through. Both of these samples were at 150 cm from the firearm where the highest amount of damage was observed. A: Heckler & Koch G36C firearm with 5.56 mm Federal Premium tactical bonded FMJ ammunition, B: Accuracy International AX308 with 7.62 mm Federal tactical bonded semi-jacketed ammunition.

Following the examination of the carbon adhesive tape substrates using the SEM/EDX, very few particles were discerned, with less than ten being identified as containing 'characteristic' GSR elements along the 400 cm range (Figure 6.9, Figure 6.10). The same analytical protocol used in Chapter 5 was used for the examination of these samples, including the same magnification, area covered and automated analysis set up. The small number of particles collected was likely due to the use of firearm accessories and/or the shooting environment as, during the test firing, the firearm discharge plume appeared to veer off to the side rather than down the firing line where the collection substrates were placed. This could be as a result of the associated muzzle brakes and flash suppressors used with the firearms which allow gas and particulates formed during the discharge of a firearm to escape through holes near the muzzle (Figure 6.15). However, the directionality of the firearm discharge plume could have also been affected by the shooting environment; although the test firings were carried out in Kent Police's indoor shooting range in Maidstone, the doors were left open for ventilation, and thus we cannot discount the influence of draft on the dispersion of particles.

A very small number of particles (≤ 0.008 particles per mm^2) was found throughout the distance sampled. Figures 6.11 and 6.12 display the relative elemental compositions for the particles found in relation to the distance from the firearm from which they were retrieved. As it can be seen from Tables 6.2 and 6.3, and presented in Figures 6.11 and 6.12, a significant number of the particles identified contained appreciable amounts of potassium (K) over Cu, and, in the case of the AX308 firearm, no Cu was observed. The 'fluff' observed when using both firearms (Figure 6.9 and Figure 6.10) was identified as Al which was likely to have originated from the firearms, muzzle attachments or centre fire ammunition as these types of residues were not identified when using rim-fire ammunition (Chapter 4 and Chapter 5).

At the immediate sampling distance below the firearms (0 cm) the silicon wafer fragments were blasted into shards and dust by the force of the firearm discharge plume and were unsalvageable. The rest of the samples were collected and analysed using FEG-SEM/EDX to investigate the individual particle morphology (Figure 6.9 and Figure 6.10) and elemental compositions (Table 6.2 and Table 6.3).

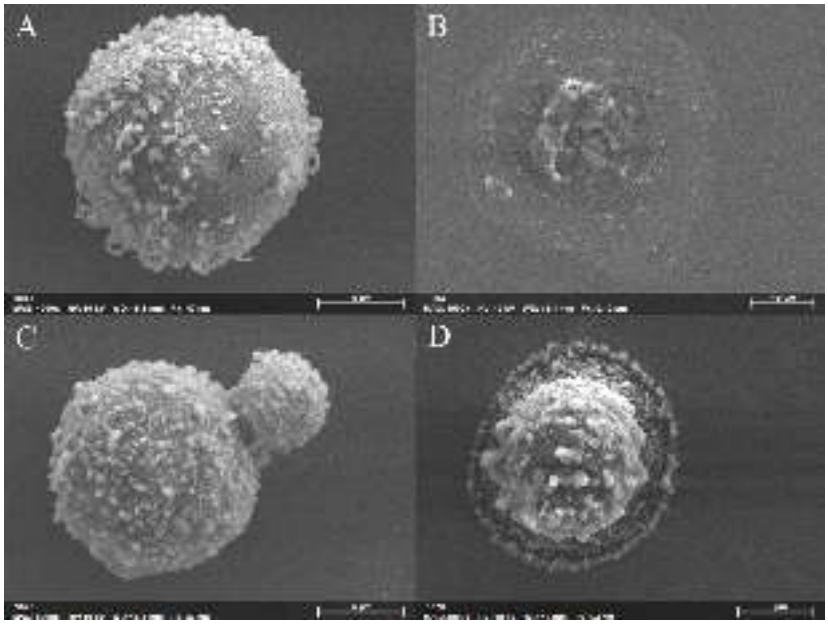

Figure 6.9: FEG-SEM images of GSR particles on the silicon substrates produced using the AX308 firearm. A: 80 cm from the firearm (Table 6.2, particle 17), B: 100 cm from the firearm (Table 6.2, particle 24), C: 100 cm from the firearm (Table 6.2, particle 19), D: 125 cm from the firearm (Table 6.2, particle 29). *HV:* 10 kV.

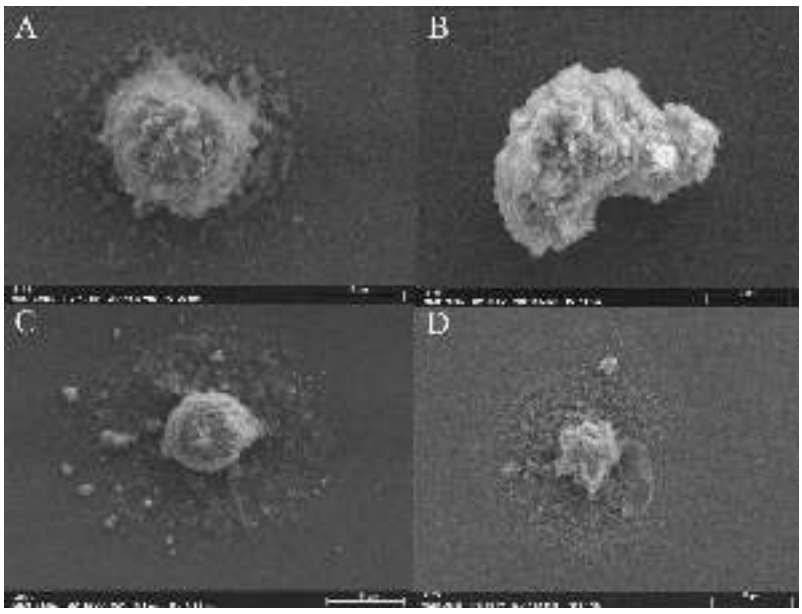

Figure 6.10: FEG-SEM images of GSR particles on the silicon substrates produced using the G36C firearm. A: 40 cm from the firearm (Table 6.3, particle 1), B: 40 cm from the firearm (Table 6.3, particle 2), C: 100 cm from the firearm (Table 6.3, particle 8), D: 40 cm from the firearm (Table 6.3, particle 3). *HV:* 10 kV.

Table 6.2: Table showing the relative elemental compositions of GSR particles found in Experiment 3.2 using the AX308 firearm. Class number as described in Chapter 5.

Particle Number	Class Number	Relative particle elemental compositions using the AX308 firearm (%)			
		% Pb	*% Sb*	*% Ba*	*% K*
1	5	61.98	0	3.72	34.30
2	6	75.81	7.11	14.52	2.57
3	5	56.89	0	32.23	10.87
4	5	64.40	0	35.60	0
5	7	55.22	0	37.91	6.86
6	6	78.22	0	16.95	4.83
7	8	69.18	0	0	30.82
8	5	62.16	0	25.94	11.90
9	8	66.35	0	0	33.65
10	8	68.36	0	0	31.64
11	8	66.49	0	0	28.69
12	8	60.04	0	0	39.96
13	5	51.92	0	40.90	7.18
14	6	64.99	0	0	35.01
15	8	73.62	0	2.44	23.94
16	7	44.16	4.3	49.62	1.92
17	5	54.06	0	43.82	2.12
18	7	55.18	38.4	4.17	2.26
19	7	52.61	7.71	36.28	3.14
20	6	71.85	6.53	17.8	3.82
21	8	78.76	0	0	21.24
22	8	89.22	0	0	10.78
23	8	57.40	0	8.63	33.97
24	8	70.18	0	0	29.82
25	8	68.99	0	0	31.01
26	8	73.76	0	15.17	11.07
27	8	76.55	0	0	23.45
28	8	69.47	0	0	30.53
29	8	57.93	0	20.31	21.76
30	8	60.39	0	9.13	30.48
31	5	62.29	0	24.83	12.88
32	5	72.58	0	0	27.42
33	5	96.11	0	0	3.89

Table 6.3: Table showing the relative elemental compositions of GSR particles found in Experiment 3.1 using the G36C firearm. Class number as described in Chapter 5.

Particle Number	Class Number	Relative particle elemental compositions using the G36C firearm (%)							
		% Pb	% Sb	% Ba	% Cu	% Pb	% Sb	% Ba	% K
1	4	-	-	-	-	60.62	0	12.27	27.11
2	5	-	-	-	-	65.41	0	30.79	3.8
3	6	-	-	-	-	76.23	0	0	23.77
4	5	57.73	40.93	0	1.35	-	-	-	-
5	5	-	-	-	-	68.49	0	11.39	20.12
6	5	-	-	-	-	59.92	0	12.75	27.34
7	7	65.50	1.09	33.31	0	-	-	-	-
8	8	61.41	28.75	4.57	5.27	-	-	-	-
9	8	70.52	20.61	4.51	4.35	-	-	-	-
10	8	87.67	8.58	1.75	2	-	-	-	-
11	2	29.26	15.43	55.31	0	-	-	-	-
12	3	-	-	-	-	28.20	6.03	62.86	2.3
13	2	41.19	20.33	28.48	0	-	-	-	-
14	2	34.28	12.06	51.69	1.97	-	-	-	-
15	8	67.16	4.19	28.65	0	-	-	-	-
16	2	-	-	-	-	51.79	13.93	6.89	27.4
17	2	39.38	13.84	43.54	3.24	-	-	-	-
18	2	45.35	22.14	30.03	2.48	-	-	-	-
19	3	26.5	9.2	63.07	1.23	-	-	-	-
20	2	26.5	21.1	52.41	0	-	-	-	-
21	2	23.46	12.06	64.48	0	-	-	-	-
22	6	26.43	10.32	63.25	0	-	-	-	-
23	5	-	-	-	-	51.83	19.80	26.67	1.7

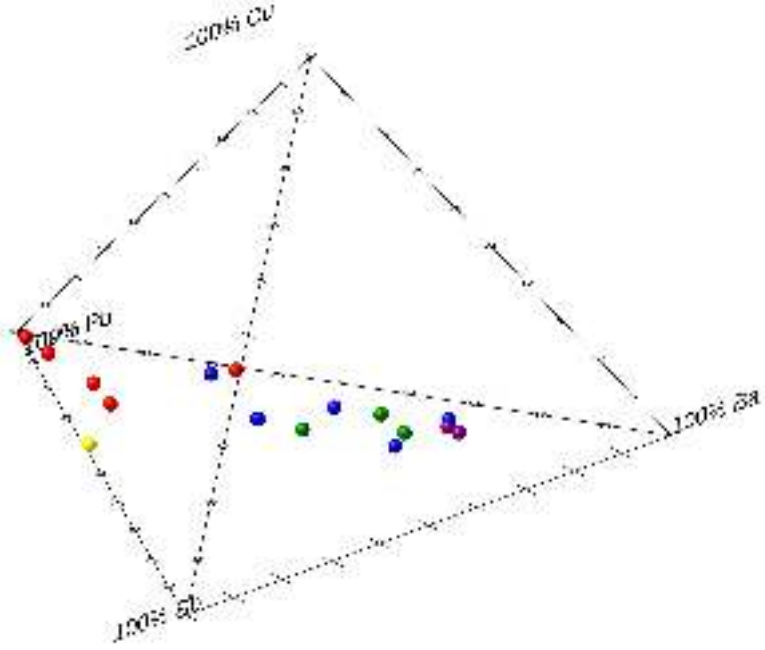

Figure 6.11: Tetrahedral plot showing the relative elemental compositions of GSR particles containing Cu in relation to their distance from the G36C firearm. Yellow: 60 cm from the firearm, red: 100 cm from the firearm, green: 125 cm from the firearm, blue: 150 cm from the firearm, purple: 175 cm from the firearm.

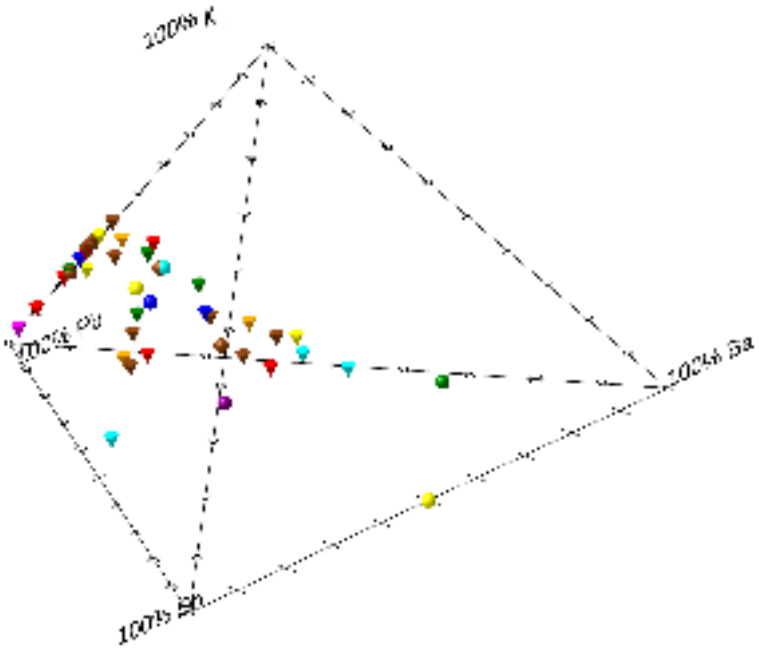

Figure 6.12: Tetrahedral plot showing the relative elemental compositions of GSR particles containing K in relation to their distance from the firearms. Orbs relate to the G36C data whereas the cones represent the AX308 particle data. Orange: 20 cm from the firearm, brown: 40 cm from the firearm, yellow: 60 cm from the firearm, cyan: 80 cm from the firearm, red: 100 cm from the firearm, green: 125 cm from the firearm, blue: 150 cm from the firearm, purple: 175 cm from the firearm, magenta: 200 cm from the firearm.

Two distinct populations of residues were also observed with the G36C firearm. These consisted of a solid, spheroidal particle surrounded by 'halo'-like spread (Figure 6.13) as well as circular, 'crystallised' residues (Figure 6.14). However, as can be seen by the spectrum presented in Figure 6.14, these particle structures do not consist of the 'characteristic' GSR elements but rather consist of sodium chloride (NaCl). This was likely due to the presence of skin salts which can arise from use and wear of the gun (Wolten G.M. et al., 1977) or due to chemical suppressors, expanded upon in the Discussion section below.

Finally, the results from the chronograph tests where the muzzle velocities were measured and compared to the literature values in Table 6.1 are displayed in Table 6.4.

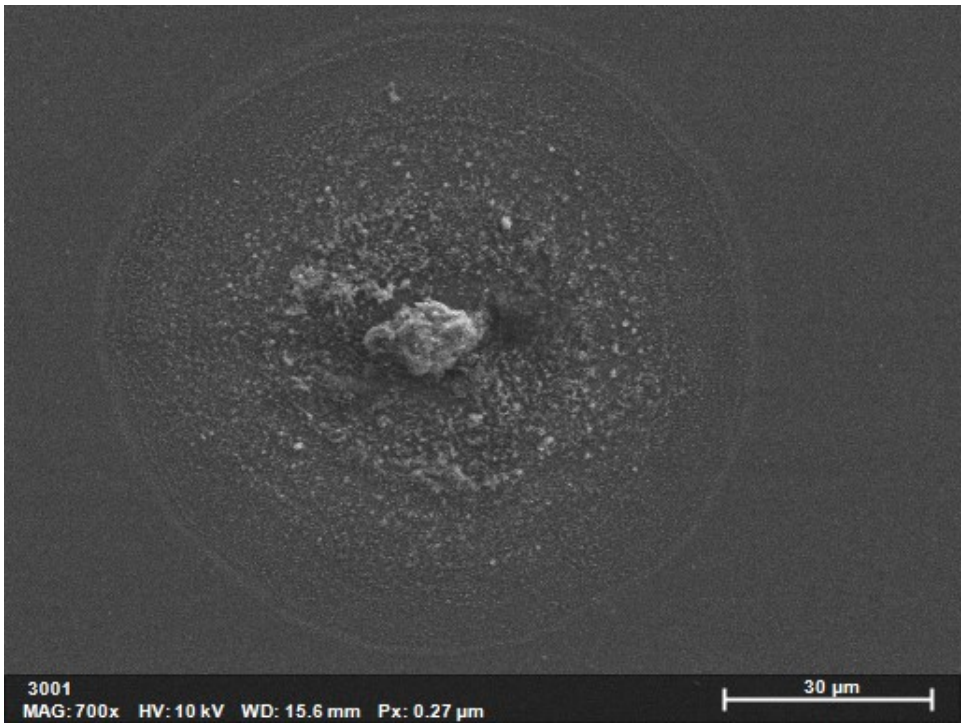

Figure 6.13: FEG-SEM image of a GSR particle surrounded by 'halo'-like spread using the G36C firearm. This population of particles was observed at a distance of 100 cm from the firearm. *HV:* 10 kV.

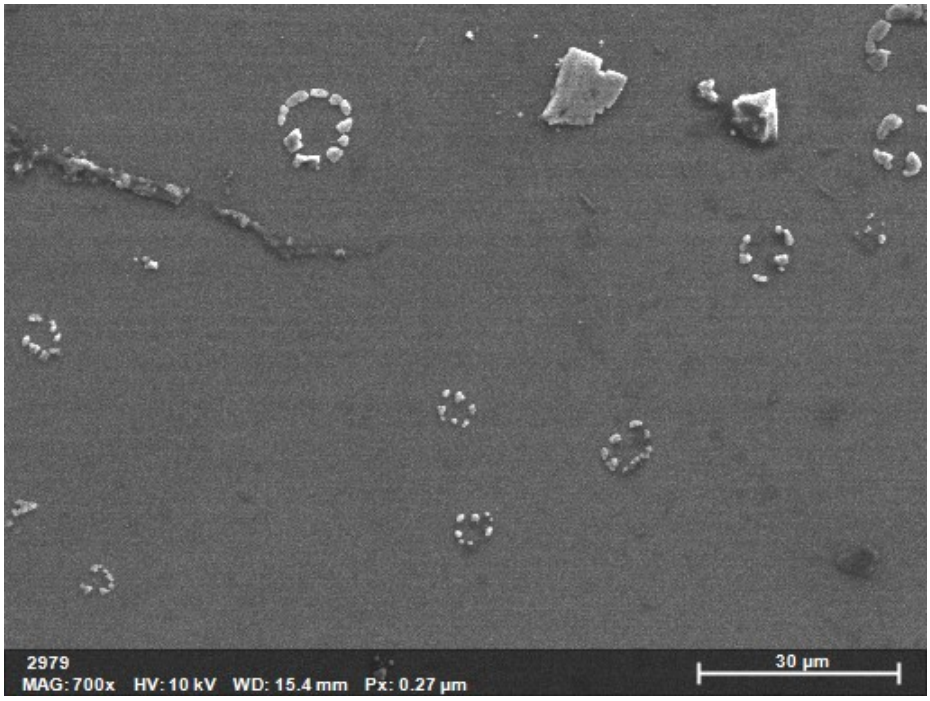

Figure 6.14: FEG-SEM/EDX image and spectrum of circular, 'crystallised' particles using the G36C firearm, consisting of NaCl. This population of particles was observed at a distance of 60 cm from the firearm. *HV:* 10 kV.

Table 6.4: Table comparing the muzzle velocities for the Heckler & Koch G36 Carbine and Accuracy International AX308 firearms. Measured muzzle velocities refer to those measured during the test firings with a chronograph and the literature values are those presented in Table 6.1. The accuracy of each measured muzzle velocity is $\pm 0.05\,\mathrm{m\,s^{-1}}$.

Firearm	Measured Muzzle Velocity (ms^{-1})	Average Measured Muzzle Velocity (ms^{-1})	Average Literature Muzzle Velocity (ms^{-1})
Heckler & Koch G36C	558.3	678.2	722
	740.4		
	706.0		
Accuracy International AX308	787.3	791.3	788
	792.9		
	793.6		

6.4 Discussion

The preliminary hypothesis for the heat damage observed in Figure 6.8, in conjunction with the low number of GSR particles observed on the carbon adhesive tape substrates, was that perhaps the GSR particles that were travelling within the discharge plume were hot. As a result, they would effectively 'melt' the adhesive layer on the carbon substrates and so without the adhesive coat, the residues would be unable to stick to the surface of the substrates. However, as no lead (or any other) residues were observed around the perforations on the carbon, it can be suggested that the residues were not in fact responsible for the damage witnessed on these samples. Due to the lack of material around the holes created by the heat damage, it would appear more likely that the cause of these perforations are due to the hot air released from the firearm, i.e. the discharge plume itself, rather than the particles travelling within it. The frequency of the heat damage perforations decreased after approximately 250 cm, which further corroborates this theory, as the firearm discharge plume would be significantly dispersed and cooled by the time it reached that distance. As the AX308 has the higher muzzle velocity, it is expected that the firearms discharge plume would be travelling with a greater velocity and force, ergo the greater amount of damage is a reasonable observation.

The particle morphologies for the residues observed with both the AX308 and G36C (Figures 6.9 and 6.10 respectively) appear to closely resemble the 'characteristic', spheroidal GSR morphology. This is especially evident with the AX308 (Figure 6.9 A and C) but both firearm residues exhibit some partial melting with a 'halo'-like spread that has been observed to expand to over 60 µm (Figure 6.13). These larger 'halo'-like spreads were more predominant when using the G36C. The size of the 'halo' in Figure 6.13 appears to be 64 µm. This could suggest that a large, spheroidal particle

with a diameter of at least 64 μm could have reached the substrate but, due to its size, had not been able to sufficiently cool before doing so. As a result, the particle hit the substrate at a normal incidence angle, depositing some of its residues in a circular, uniform manner, hence the 'halo'-like spread observed. Another hypothesis for the existence of these patterns could be that the residues that were expelled from the barrel, and subsequently got trapped in the firearm discharge plume, had insufficient time to form into a sphere. Therefore, the core of the particle may have started to form but impacted before the rest of the particle could come together. This would explain the solid, spheroidal particle observed at the centre of the residue spread, followed by a densely populated, intermediary perimeter before reaching the faint, outer layer of the 'halo'.

The G36C firearm produced residues containing the 'characteristic' GSR elements (Pb, Sb, Ba) and occasionally contained Cu (Table 6.3). However, the Cu was often replaced by K, and in the case of the AX308, no Cu was detected at the 1% level. (Table 6.2). Although this may initially appear inconsistent with previously acquired data, these observations can be explained by considering the less common elements present in GSR. As discussed in Chapter 2, Pb, Sb and Ba are 'characteristic' GSR elements as the existence of all three (in conjunction with a spheroidal morphology) from non-firearm related origins is highly unlikely. However, there are some less common elements that are also present in GSR, and K is one of them, along with aluminium (Al) and calcium (Ca). Al and Ca were also observed in some of the residues collected during both Experiments 3.1 and 3.2, however, their presence was not consistent within all particles. Moreover, as these elements are not exclusive to GSR and can be readily found in the environment, in conjunction with the low concentrations at which they were observed at ($\leq$ 2 %), they were excluded.

Upon investigating the relative elemental compositions in Table 6.3, it appears that the more spheroidal, solidified particles (such as Class 7 or Class 8) consist of a higher concentration of Pb in comparison to more irregular, or molten-like particles. This, however, is only true of the G36C firearm and the same cannot be said about the AX308 (Table 6.2). A key difference between these data which may explain this difference is the presence of Cu. The G36C data that shows a significant amount of Pb for class 6 and class 7 particles also exhibits the existence of Cu. However, none of the particles produced when using the AX308 contained any Cu whatsoever. Cu has often been observed to maintain its solid structure (discussed in Chapter 5), as the temperatures experienced by the residues upon ignition do not exceed its melting point of 1085°C. By removing a heavy element and replacing it with a Group 1 metal that, in its pure form, can be cut with a knife, it could mean particles cannot form with the

same efficiency. By removing that 'anchor' (Cu) that could be used to build upon, the vapourised, soft metals may form into more homogeneous spheroidal residues rather than be significantly dominated by lead as previously observed. This is made evident in Figure 6.12 where both the AX308 and G36C firearm residues show a greater variation in elemental composition with K present, unlike with Cu (Figure 6.11).

The firearms that are used by the Kent Police armed forces (including those that were used in this experiment) are modified to contain flash suppressors (Figure 6.15).

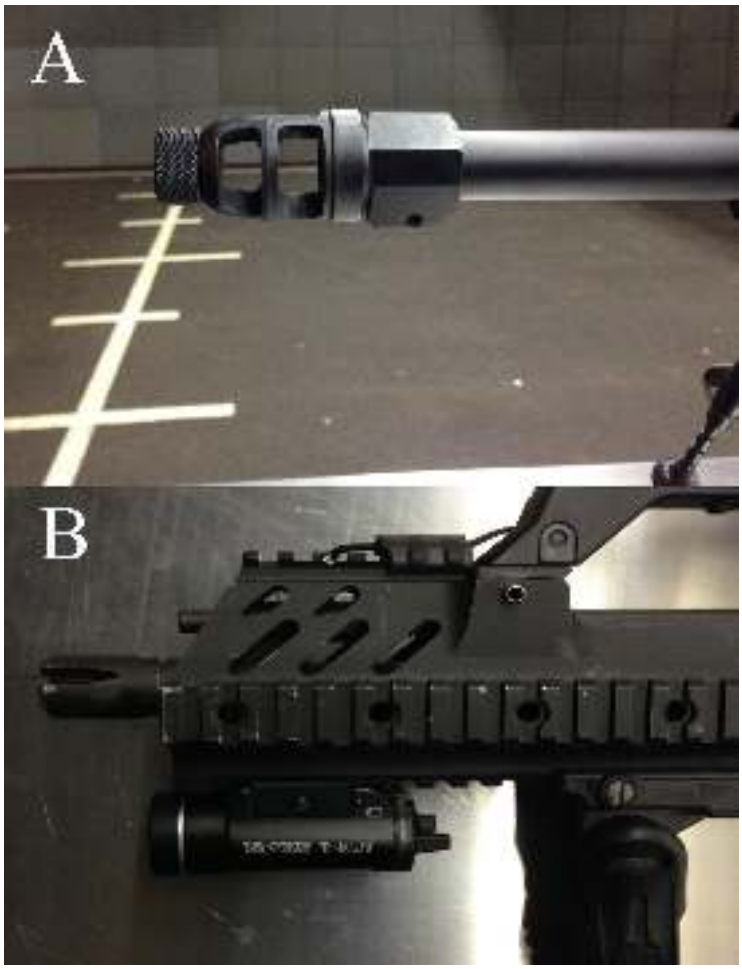

Figure 6.15: Photograph of the muzzles pertaining to each firearm. A: AX308 muzzle with 20″ barrel and flash suppressor, B: G36C muzzle with small flash suppressor.

Flash suppressors are often used in an attempt to mechanically limit the flash that occurs from the force of the explosion once a weapon is discharged and the bullet leaves the barrel. With the muzzle suppressors that are used by Kent Police, a series of slits at the muzzle can be observed (Figure 6.15: A) where the gas can escape to prevent a big flash from the end of the barrel. However, since the primary cause of the flash is the combustion of hydrogen and carbon monoxide, chemical suppressors (often part of

the ammunition) are also used. These chemical suppressors often consist of an alkaline salt, one of which can be NaCl (Wallace J.S. (2008); Rinker R.A. (2005)). Therefore, despite the particles observed in Figure 6.14 not being of particular GSR relevance, they are significant in demonstrating the use of chemical suppressors. This is further reinforced by the fact that these circular residues are not observed with the AX308, which has a more efficient flash suppressor with multiple, larger slits over the one used with the G36C.

The use of these suppressors could also explain the lack of residues collected during the test firing. As they have multiple slits nearing the end of the barrel in order to suppress the flash produced upon firing, a large amount of particles escape. This will affect the directionality at which GSR particles are travelling in, and so a smaller number of residues will exit from the end of the muzzle down the firing line.

Finally, upon investigating the muzzle velocity of each firearm and comparing them to their respective literature values (Figure 6.4), it can be seen that the values are fairly consistent. The AX308 boasts accurate values with a small $10.6\,\mathrm{m\,s^{-1}}$ maximum deviation. This is expected as a longer, $20''$ barrel was used for these test firings which would also lead to a slightly higher muzzle velocity. However, the G36C shows more inconsistent results with all measured values being less than the expected value based on the literature. This is not unexpected with burst fire or semi-automatic firearms as their 'quick-fire' nature can cause larger variations. Even so, a muzzle velocity of $588.3\,\mathrm{m\,s^{-1}}$ was low in comparison to the literature value of $722\,\mathrm{m\,s^{-1}}$ and so may imply that a faulty cartridge or incomplete primer burst may have caused this.

However, as Kent Police were unable to provide a follow-up test firing to further corroborate these data, these are just hypotheses. Further test firings need to be undertaken to prove these hypotheses, and would make an ideal post-graduate project.

In the next chapter, a light gas gun was used to control the environment in which GSR formed to gain further insight into the formation mechanisms.

Chapter 7

Experiments investigating the particle formation and impact melting of gunshot residue analogues using a light gas gun and hydrocode modelling

Content in this Chapter is based on, and in areas reproduced from, Spathis V. & Price M.C. (2019) entitled 'Experiments using a light gas gun to investigate the impact melting of gunshot residue analogues'. The aforementioned paper was produced during this PhD, and is listed in the declarations for this thesis.

7.1 Introduction

The investigation of centre-fire primers (discussed in Chapter 6) unfortunately did not yield sufficient results to allow for direct comparisons between rim-fire and centre-fire GSRs. Therefore, to understand the formation mechanisms of GSR, the metallurgy of

these inorganic residues were examined. In this set of experiments, the versatility of the University of Kent's light gas gun was utilised (Burchell M.J. et al., 1999) to obtain a selection of corroborative data regarding the formation, and impact, of metallic gunshot residues onto high purity silicon wafers. Prior investigation of GSR using subsonic rim-fire ammunition (presented in Chapter 5) led to the discovery that at certain distances from the firearm the residues exhibit irregular, typically molten, morphologies as they hit the target, rather than the 'traditional' spheroidal shape (Wolten G. et al. (1979a); Kara L. et al. (2016)). The morphologies of these impact-disrupted GSR were classified according to the degree of melt exhibited by the particles (Spathis V., 2017) and investigations commenced into determining whether their morphologies were temperature-related (due to their molten appearance) or due to the force of impact onto the substrate. Ueyama R.L. et al. (1980) examined muzzle-blast derived GSR and found irregular particles "appear only rarely at target distances of 12 inches [$\sim$ 30.5 cm] and beyond". They speculate that irregular particles will be subject to more drag, in comparison to spherical particles, and so will lose their energy sooner, travelling shorter distances. The light gas gun was used to do a set of controlled experiments to investigate GSR formation mechanisms by separating the ignition process of the primers from the residue impacts. This allowed for a closer look into the formation of these particles and helped determine whether their varied morphologies are due to the heating caused during the activation and combustion of the primer (section 7.3) or whether they are due to impact melting (section 7.4). This information can aid in the understanding of metallic particle formation in different pressure environments and give insight into the physical state of firearm residues when they impact a surface.

7.2 Materials & Methodology

The University of Kent's two stage LGG was used for both of the experiments described in this section. The targets used in these experiments were the 600 µm thick, optically polished, high purity silicon wafers that were used and described in Chapter 5. Prior to use, the silicon substrates were cleaned using 99.5 % isopropyl alcohol and cotton buds to remove any surface contaminants. Once dried, they were each fixed onto an aluminium stub with double-sided adhesive carbon tape and placed in an enclosed container. The substrates were removed solely for the test firing in the lab and gun room, using gloves to avoid any external contamination. This ensured that any residue-like particles found on them during the analytical process were a product of the firing itself.

7.2.1 Analytical Methodology

The samples were all analysed using the two SEMs equipped with their corresponding EDX detectors (discussed in Chapter 3). The Hitachi S-3400 SEM with Oxford Instruments' *X-Max* 80 mm^2 EDX detector was used to acquire low magnification topographical maps of the substrates, showing the abundance and dispersion of particles on each sample. Following that, the Hitachi S-4700 FEG-SEM with a Bruker *X-flash* 5060f flat-quad EDX detector was used for the individual morphological and elemental particle analysis due to its high spatial resolution which allows for elemental discrimination down to the sub-micron level (see Chapter 3). An accelerating voltage of 10 kV was used for all analyses to ensure sufficient X-ray emission stimulation from the metallic elements present, thereby providing discriminatory X-ray peaks for each, while still retaining topographical detail.

7.3 Variable Pressure Experiments

The first experiment investigated how metallic firearm discharge residues form as they traverse through air under differing environmental conditions. This experiment was carried out with two different types of primer: CCI 10 shotgun, and CCI Mini-Mag primer used for small rifles. As it was uncertain whether this experiment would produce any viable results, the CCI 10 shotgun primer was used to test the hypothesised experimental protocol. During normal operation of the LGG, the as-supplied CCI 10 primer fitted into the blank cartridges is fired off and removed from the cartridge. Thus, for the initial experiments these primers were used to avoid wastage, while at the same time determined whether residues were in fact successfully produced and collected using this method.

Once the experimental procedure was optimised and residues were successfully produced and collected onto the substrates, the CCI Mini-Mag primer was used in order to attempt to reproduce the findings presented in Chapter 5. This was done by first removing the CCI 10 shotgun primer caps (post-firing) prior to creating an adaptor system (Figure 7.1), then modifying the cartridges to hold the smaller, CCI Mini-Mag primer (discussed in the Experimental Set-up subsection below).

As it is solely the primer of the CCI Mini-Mag ammunition that was used, rather than the CCI Mini-Mag ammunition as a whole, this experiment does not entirely mimic the one discussed in Chapter 5, so some differences in the residues (both morphological and with regards to the elemental compositions) were expected. However,

Figure 7.1: Picture of the 3D printed primer adaptor holder for CCI Mini-Mag primers that was designed by Vassilia Spathis (author) to fit into a CCI 10 shotgun cartridge.

as the majority of the metallic residues produced are as a result of the primer rather than the propellant (see Chapter 2) and only particles from the primer are considered to be characteristic of GSR (Cellmark Forensic Services), an adequate comparison can be made between the results produced from each experiment.

7.3.1 Experimental Set-up

In order to examine the formation of metallic gunshot residues further, an experiment was devised in which primers were fired under different pressures. When using the CCI 10 shotgun ammunition for the preliminary part of the experiment, the cartridge was loaded into the gun in the same way as when doing a standard high speed shot on the Kent LGG (see Chapter 3). However, when the main part of the experiment was carried out using the CCI Mini-Mag primer, the shotgun primer was fired off and the primer caps were removed using a primer removing apparatus (Figure 7.2). An adaptor was then designed and 3D-printed (Figures 7.1, 7.3 and 7.4) to hold the smaller CCI Mini-Mag primer. This adaptor was fitted into the space previously occupied by the shotgun primer cap in the shotgun cartridge and epoxy resin was used to fix the adaptor in place (Figure 7.5). The CCI Mini-Mag primer was placed into the adaptor in the shotgun cartridge, followed by small amounts of polyvinyl acetate (PVA) glue around the 'top rim' of the primer and left to dry for 48 hours. This ensured that the primer would remain in place during the ammunition loading and firing process and provided an air tight seal. An example of the modified cartridges can be seen in Figure 7.6. Once the modifications were completed, the shotgun cartridge with the newly-installed adaptor system was loaded into the LGG as normal.

Once the shotgun cartridge with each primer was loaded into the LGG, the pump-

Figure 7.2: Picture of primer remover apparatus. Once the active primer was fired off on the LGG, the shotgun cartridge would be placed upside down with the pin sitting below the empty primer cap, allowing the cap to be removed and replaced by pushing the lever down.

tube (the first stage of the LGG) was used as a sealed gas container, allowing for the internal gas pressure to be accurately controlled. The target was then fixed at the entry to the launch-tube, thereby enabling particles to land on the substrate. The primer was initiated using an external striker and the residues were allowed to move down the pump-tube based solely on the energy released during the ignition of the primer.

A selection of shots using the CCI 10 shotgun primer under different gases, pressures and sub-zero temperatures, were initially carried out (Table 7.1). These test firings were initially used to determine whether a selection of gases and pressures should be investigated. This was primarily done out of interest to determine whether there would be any visible difference in residue formation between the different environments. This meant changing the gas used while maintaining the pressure as consistently as possible. However, prior to the test firing, the pump tube had been placed in a carbon dioxide freezer for a separate project and had not warmed up to room temperature. Therefore, rather than postpone the test firing, the cold pump-tube was used to investigate the effect different gases have on the morphology of the primer residues at sub-zero temperatures. The temperatures for each shot were measured using a PT 100 thermocouple, allowing for comparisons with the room temperature data.

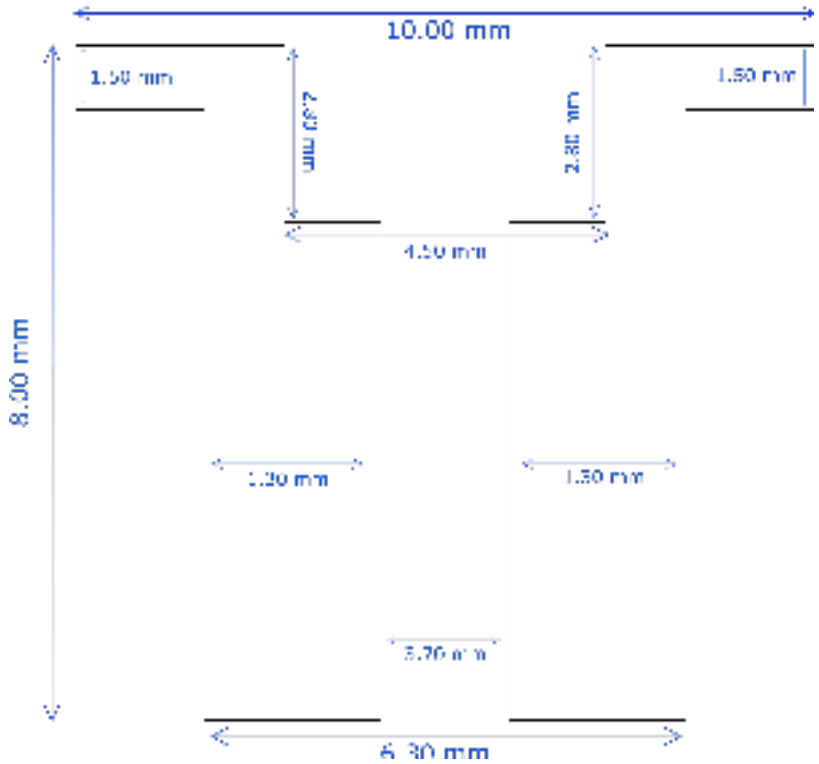

Figure 7.3: Side view diagram (not to scale) showing the primer adaptor schematic for Figure 7.1 which allowed rim-fire primer caps to sit within a shotgun cartridge.

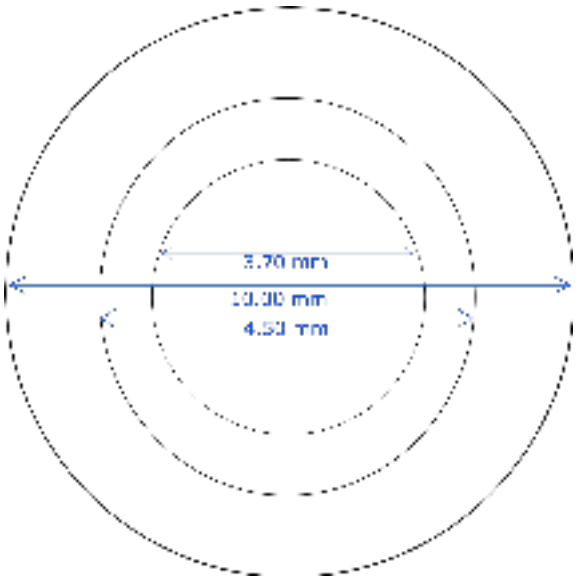

Figure 7.4: Top-down view diagram (not to scale) showing the primer adaptor schematic for Figure 7.1 which allowed rim-fire primer caps to sit within a shotgun cartridge.

Figure 7.5: Pictures of the CCI 10 shotgun cartridge modification steps to include the primer adaptor. A: an original CCI 10 shotgun cartridge, B: the shotgun cartridge post primer firing, C: the shotgun cartridge with the primer cap removed, D: the modified shotgun cartridge containing the primer adaptor.

Figure 7.6: Picture of the fully modified CCI 10 shotgun cartridge with the CCI Mini-Mag primer loaded using the 3D printed adaptor.

Once the selection of gases to be investigated had been narrowed down, approximate pressures of interest needed to be selected. The CCI 10 shotgun primer was utilised again, firing off the cartridges under a range of gas pressures. After the finalised pressures had been decided, the CCI Mini-Mag primer-modified cartridges were fired under the final selection of gases and pressures. The gases and pressures investigated with the two primers are shown in Table 7.2.

Table 7.1: Table showing the different gases investigated at sub-zero temperatures. As air was going to be included in the final list of gases investigated regardless, the pressure did not need to be maintained at ~ 1.3 mbar. Instead, the lowest pressure that could be achieved on the LGG at the time was used.

Gas	Pressure (mbar)	Temperature (°C)
Air	0.061	-26.0
Ar	1.2	-14.6
CO_2	1.2	-12.9
H_2	1.4	-15.0
He	1.6	-11.0
N_2	1.2	-11.6
	1.4	-3.0

Table 7.2: Table showing the different gases and pressures investigated with each primer type using the LGG. All shots were carried out at environmental temperature $\sim$ 18°C - 20°.

Primer Type	Gas	Pressure (mbar)
CCI 10	Air	0.056
		0.53
		0.52
		1.5
		1.8
		50
		100
		200
		1000
		2100
		3100
	CO_2	2300
	N_2	4900
		5000
		19900
		20000
CCI Mini-Mag	Air	0.67
		3.1
		3.8
		4.8
		1000
	CO2	2.7
		4.3
		1000
	N2	1.3
		2.8
		1000

7.3.2 Results

The results for the sub-zero temperature test firings are shown in Figure 7.7. It is clear that the different gases have an effect on particle formation at low pressures due to the range of morphologies observed.

Example image maps from the particle formation samples produced under different

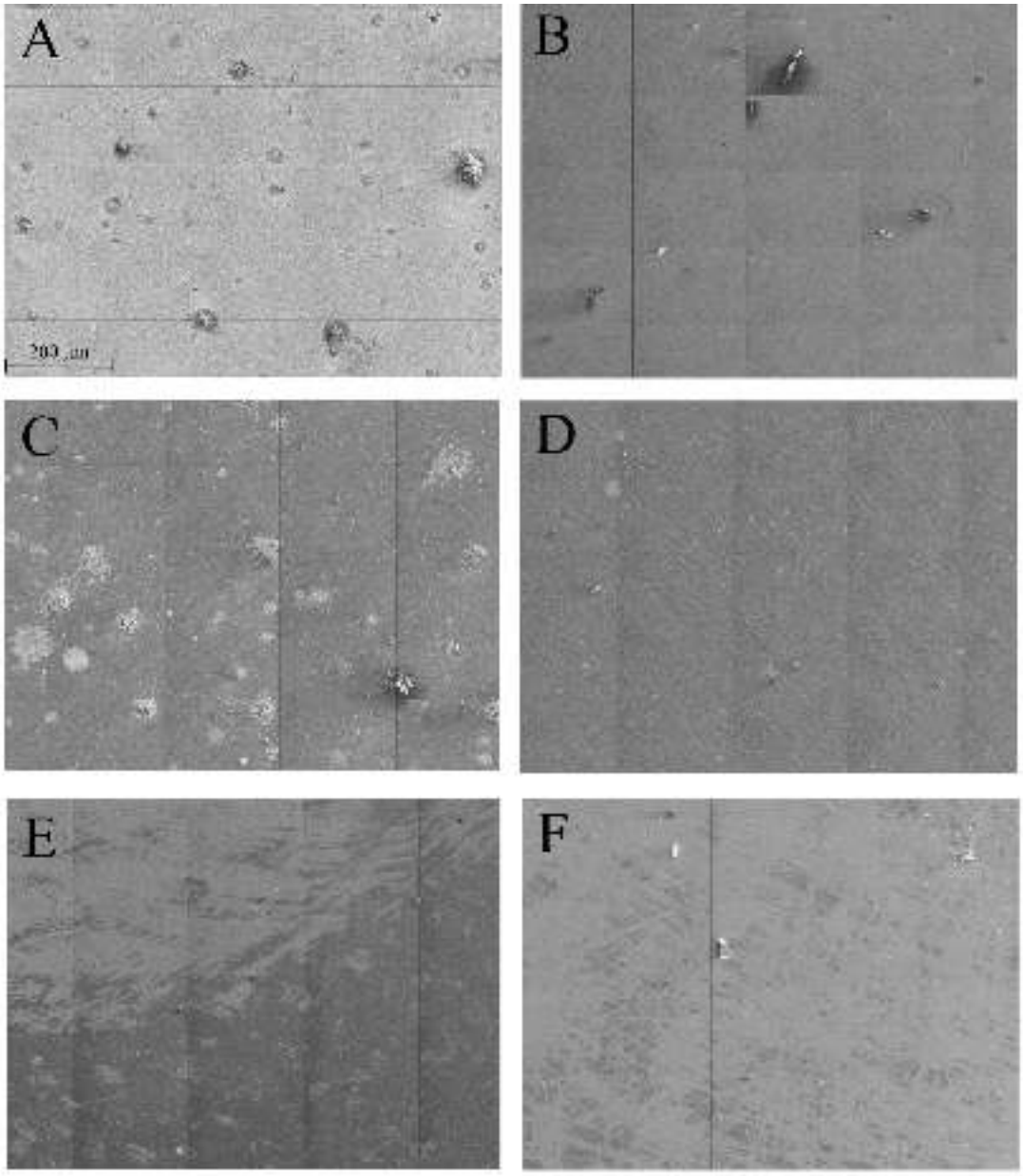

Figure 7.7: Partial SEM image montages of the particles collected at subzero temperatures for each gas showing the difference the abundance of residues as well as their varying morphologies, using the CCI 10 shotgun primer. The images were taken from the central part of the substrate where the maximum number of residues were observed and are all to the same scale (bottom left hand corner of Figure 7.7A). A: Air -26°C (0.061 mbar), B: Ar -14.6°C (1.2 mbar), C: CO_2 -12.9°C (1.2 mbar), D: H_2 -15.0°C (1.4 mbar), E: He -11°C (1.6 mbar) and F: N_2 -11.6°C (1.2 mbar). *HV* 10 kV.

air pressures are presented in Figures 7.8 and 7.9. Figure 7.8 displays residues found after firing the primer under atmospheric pressure (Figure 7.8A) and an example of the residues seen at 1.5 mbar (Figure 7.8B), whereas Figure 7.9 shows the results over a range of pressures from near-vacuum to two times atmospheric pressure. Due to the absence of particles collected under a pressure of 3100 mbar, this substrate was not included. From these data, it is apparent that as the pressure changes, so does the particle morphology and spatial density frequency on the silicon substrate.

The particles produced using the CCI Mini-Mag small firearm primer were significantly smaller in number than with the CCI 10 primer. Tetrahedral plots showing the relative elemental compositions were plotted for each gas (Figures 7.11, 7.12 and 7.13), with each colour representing a stage in the particles' morphology- solid, partially molten or molten (Figure 7.11).

The CCI Mini-Mag primer produced a range of results under different gas environments. When air was used, morphologies that have previously been encountered during both the CCI 10 test firings, as well as in Chapter 5, were observed. However, CO_2 produced very few particles at atmospheric pressure, none of which resembled the previously encountered GSRs. As the pressure decreased, the residues became increasingly more GSR-like, with spheroidal, nodular morphologies observed (Figure 7.10C). The gas that yielded the least particles was N_2, where very few particles were successfully collected under environmental pressure, despite N_2 making up 78.09% of dry air. The small number of GSR particles that were collected and analysed were done so at lower pressures, and also displayed an 'uncharacteristic' morphology (Figure 7.14).

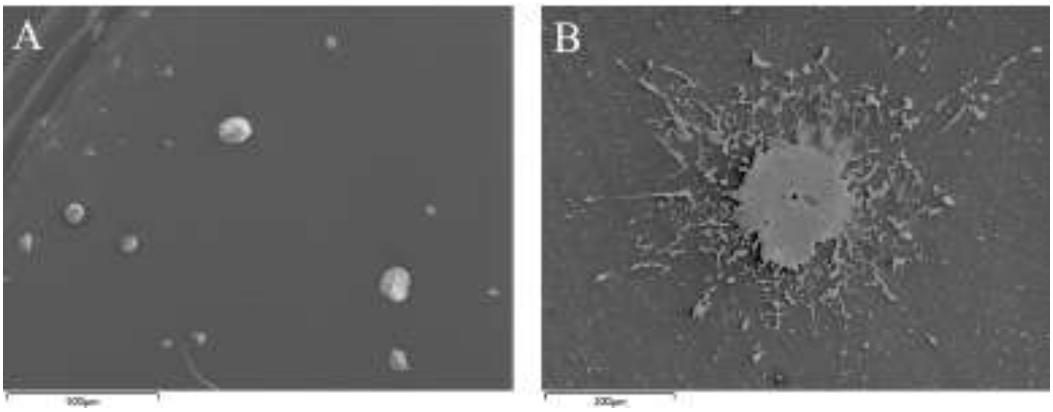

Figure 7.8: SEM images of the particles collected under atmospheric and low air pressures showing the difference in particle morphology, using the CCI 10 shotgun primer. A: Image showing the particle distribution and morphology after particle launch under atmospheric pressure (1000 mbar, scale: 500 µm), B: Image of an impacted particle ejected during the ignition of the primer under a pressure of 1.5 mbar (scale: 100 µm. HV 10 kV).

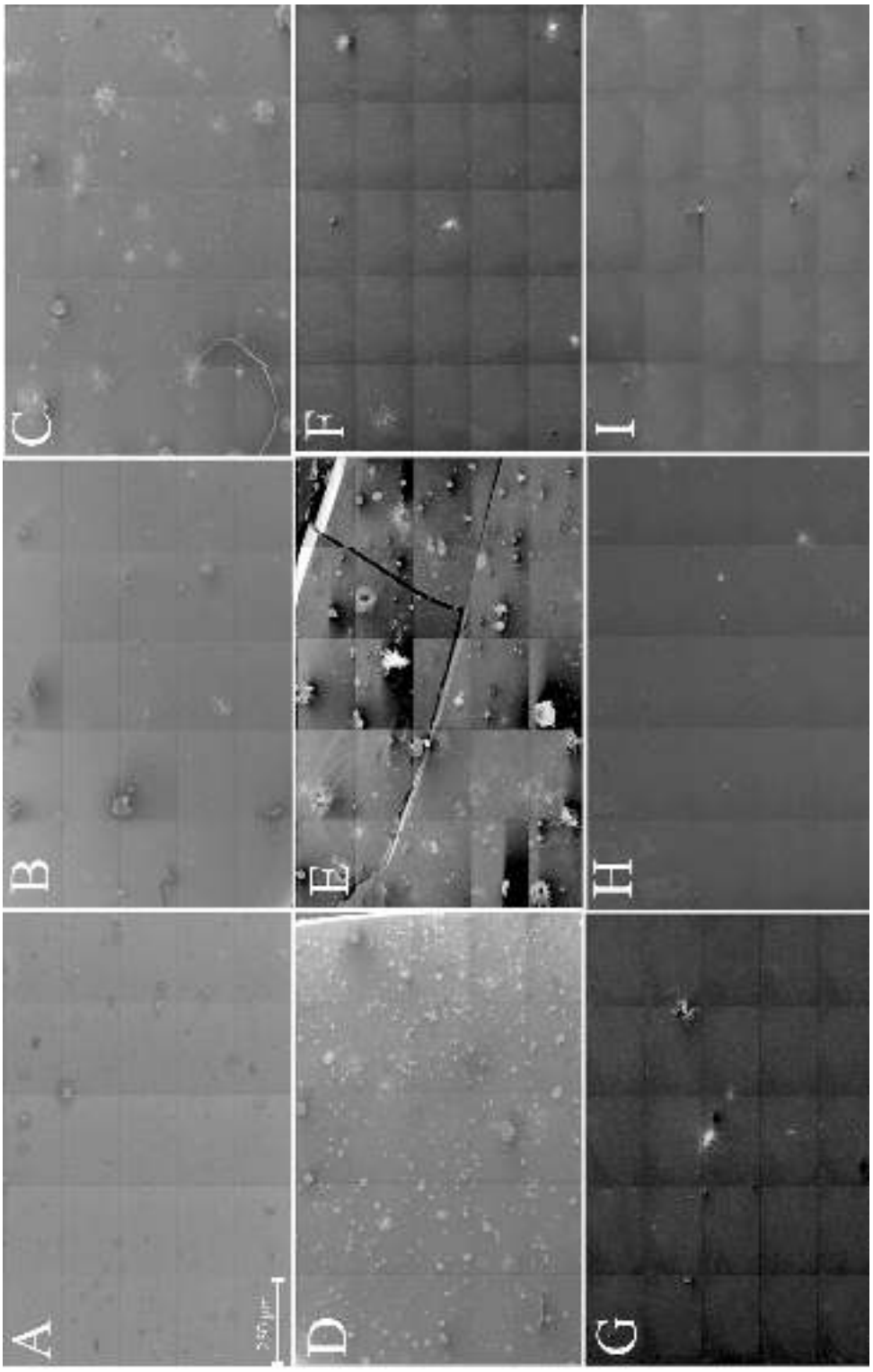

Figure 7.9: Partial SEM image montages of the particles collected under different air pressures, using the CCI 10 shotgun primer. The images were taken from the central part of the substrate where the maximum number of residues were observed and are all to the same scale. A: 0.056 mbar, B: 0.33 mbar, C: 0.52 mbar, D: 1.5 mbar, E: 1.8 mbar, F: 50 mbar, G: 100 mbar, H: 200 mbar and I: 2000 mbar. HV 10 kV.

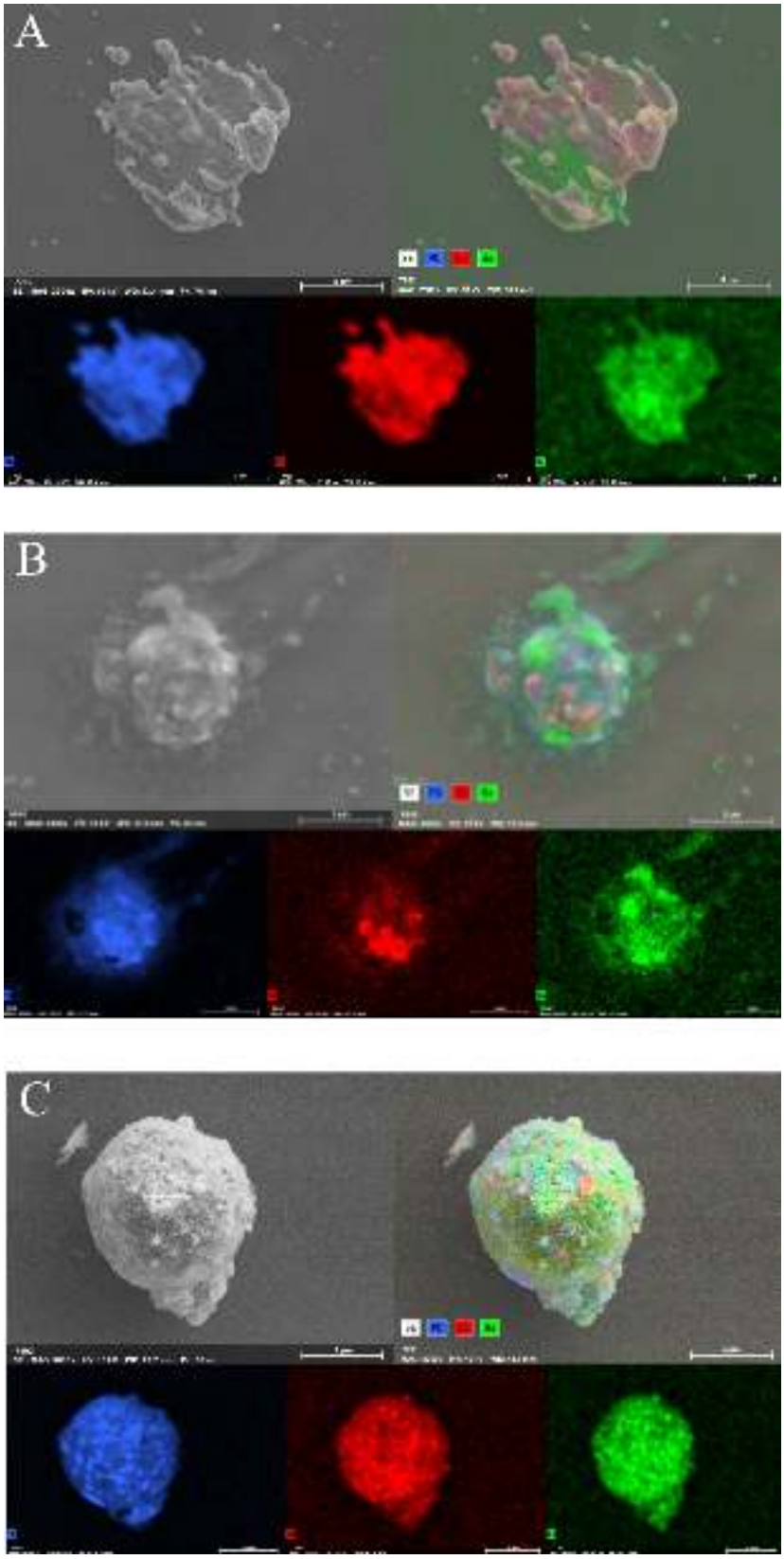

Figure 7.10: FEG-SEM/EDX images of the archetype residues used during the particle classification process (Figure 7.11) A: molten (scale bar = 8 µm), B: partially molten (scale bar = 5 µm) and C: solid (scale bar = 4 µm). *HV* 10 kV.

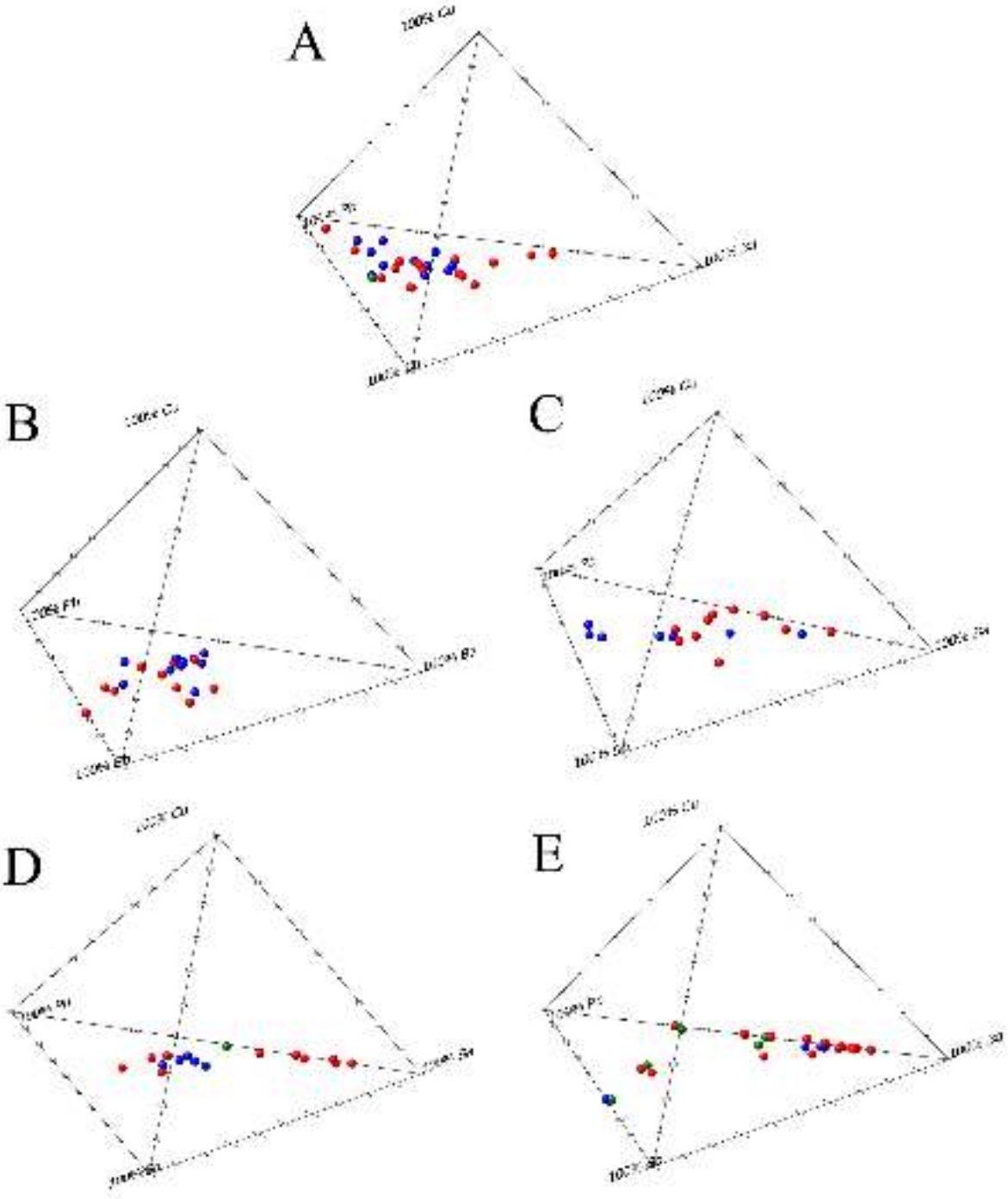

Figure 7.11: Tetrahedral plots showing the relative elemental compositions of the CCI Mini-Mag residues in air. A: 1000 mbar, B: 4.8 mbar, C: 3.8 mbar, D: 3.1 mbar, E: 0.67 mbar. Red: solid, blue: partially molten, green: molten.

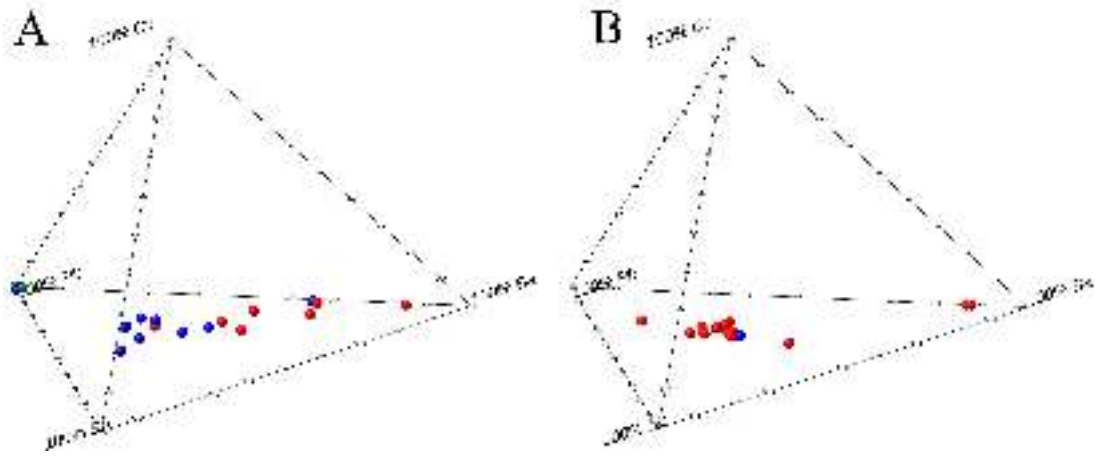

Figure 7.12: Tetrahedral plots showing the relative elemental compositions of the CCI Mini-Mag residues in CO_2. A: 1000 mbar, B: 2.7 mbar. Red: solid, blue: partially molten, green: molten.

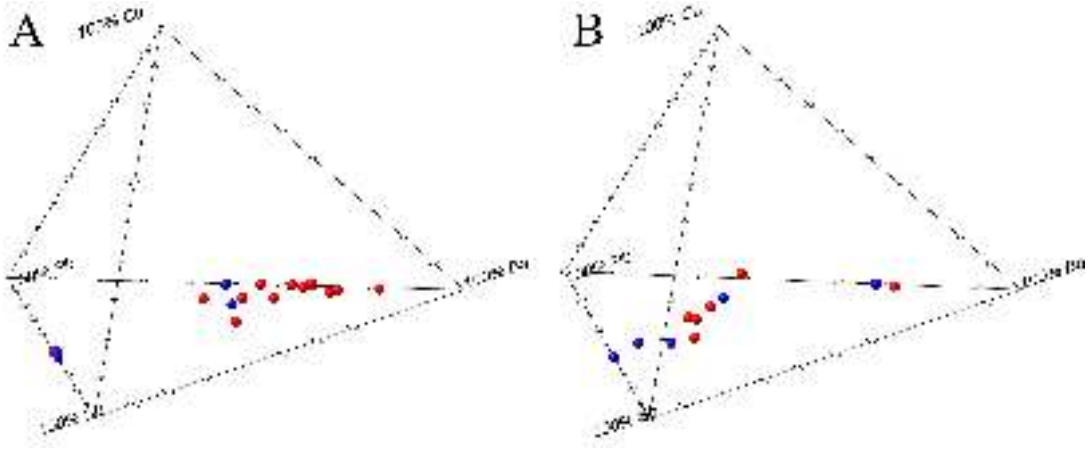

Figure 7.13: Tetrahedral plots showing the relative elemental compositions of the CCI Mini-Mag residues in N_2. A: 1000 mbar, B: 2.8 mbar. Red: solid, blue: partially molten, green: molten.

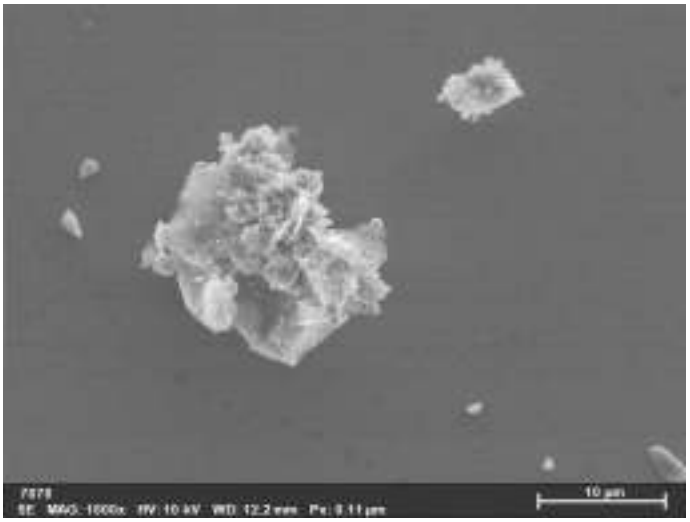

Figure 7.14: FEG-SEM image of the irregular GSR particle morphologies observed when using N_2. This particle was formed at 2.8 mbar of N_2. *HV* 10 kV.

7.3.3 Discussion

The results of the experiments carried out in this section provide useful insight into the formation processes of the primer residues during launch. Firstly, when considering which gases should be investigated during the sub-zero test shots, the existence of residues was crucial. Figure 7.7 demonstrates that a substantial number of residues were observed when using air, CO_2 and H_2. As these test shots were carried out under fairly low pressures (~ 1.4 mbar), the use of these gases did not present a safety problem. However, upon considering the different pressures that were to be investigated, the feasibility of using H_2 was reconsidered due to its highly flammable nature. Therefore, H_2 was to be replaced with Ar or He or N_2. As Ar and He are both noble gases that produced little to no residues, N_2 was chosen. Despite the lack of particles that were collected when using N_2, it was deemed as the most likely option to yield results due to the high concentration of nitrogen in dry air.

Figures 7.8 and 7.9 indicate that the frequency and morphology of the particles present do vary with pressure. The relation appears to be that as the pressure decreases, the number of particles increases, suggesting an inverse relationship. At a pressure of 1.5 mbar and 1.8 mbar, displayed in Figures 7.9D and 7.9E respectively, it appears as though the observable particle frequency is at its maximum, despite firing primer at even lower pressures. The particles also exhibit a molten morphology at these pressures, as shown in Figure 7.8. However, what is not immediately observable in the SEM images (Figure 7.9) is that the samples collected using a pressure of 0.056 mbar and 0.33 mbar were completely coated in a dark residue that could be seen under ambient light, which obscured smaller particles. This meant that trying to get overall

topographical detail with the SEM was challenging due to this additional layer of residue (presumed organic). Conversely, as the pressure was increased to atmospheric pressure and beyond, the particle frequency per substrate decreased, with only a few particles being visible. This is most likely attributed to the higher density gas in the pump tube as a result of the increased pressure. By increasing the air pressure in the pump tube, a larger number of particles are present so there are many gas particles packed within the tube that inhibit the movement of the residues coming down towards the substrate.

With respect to the particle morphologies, it is evident that the general pattern followed by the residues is that the lower the pressure, the more molten their appearance. When looking at the individual particles on the samples below atmospheric pressure, it is clear that there is a significant amount of progressive melting. At the lowest pressures, it appears as though the particles were either substantially molten, and/or hit the substrate with great speed as there is a thin, residual, 'splatted' outline around each particle core, which is the only part of the particles that is clearly discernible. As the pressure was increased, the 'splats' became more structured, until they reached a semi-molten, coagulated shape at 1000 mbar (Figure 7.8). However, their structured morphology also appears to be size-dependent, as the smaller particles seem to have solidified into spheres whereas the larger ones still retain a molten centre. This is expected as, to first order, the relative particle cooling time is a function of the volume of a particle, and thus is eight times faster for a particle with half the diameter, as mentioned in Chapter 5. The larger particles would not have had the chance to cool because of their added size and, adding to that the lack of aerodynamic drag and friction at the lower pressures, there was insufficient time for the particles to cool by the time they reached the substrates.

When using the CCI Mini-Mag ammunition, very few particles were produced, irrespective of pressure. Due to the modifications that had to be made to the cartridge in order to accommodate for the smaller primer, it was likely that some of the residues got trapped inside the different, custom components of the cartridge. Moreover, as this primer used is for small calibre firearms rather than shotguns, the primer itself is weaker and produces a smaller blast. This would produce less residues altogether, with even fewer successfully making their way down the pump-tube for collection and analysis.

The particles that were successfully recovered were crudely classified according their degree of melting, as indicated in Figure 7.10. Figure 7.11 maps out the relative elemental compositions of the particles classified at each pressure using air. Although there is not a large variation between the elemental compositions of particles found at

each pressure, it is worth noting that the residues are significantly more homogeneous than those encountered in Chapter 6, with some skewing towards the 100 % Ba peak. This is most likely due to the absence of a projectile, which consists primarily of Pb and would significantly contribute to the overall elemental make-up of the residues. As can be seen in Figure 7.11, there are very few particles that exhibit a molten morphology, despite the promising results yielded by the CCI 10 ammunition. This pattern is also observed when firing under both CO_2 and N_2 (Figure 7.12 and Figure 7.13 respectively), therefore, it appears as though the lower energy, small pistol primers did not produce residues with a significant enough energy to recreate the morphologies observed previously.

The residues produced under different gas environments yielded unexpected results. The CCI 10 test shots suggest that as pressure decreases, more molten-like residues will be encountered. However, in the case of the CCI Mini-Mag primers used here, no substantial melting was observed, as discussed above. At atmospheric pressure, both CO_2 and N_2 did not produce a significant number of particles. However, as the pressure decreased, 'characteristic' GSR particles began to be discerned on the CO_2 samples. The use of N_2 did not yield many results, with the only particle morphologies observed being the unfamiliar structures like those displayed in Figure 7.14. This was unexpected as, due to the high concentration of N_2 in dry air, morphologies similar to those included in Chapter 5 or under air conditions were assumed. But alas, 'twas not so.

Understanding the characteristics of metallic particles before impact, and how molten metallic morphologies form, can have applications in various metal coating technologies (Fauchais P. et al. (2004); Cisek J. et al. (2013)). Metal coating techniques can be thermal (Brandolt C.D.S. et al., 2017), warm (Kuroda S. et al., 2008) or cold spraying (Stoltenhoff T. et al., 2002). Thermal spraying is performed when a metallic powder is injected into a hot stream of gas to melt the powder prior to spraying, whereas warm spraying is a coating technique in which coatings are formed by the high-velocity impact of solid powder particles heated to temperatures below the melting point of the powder material. Kuroda S. et al. (2008) has demonstrated that as the carrier gas (i.e. the gas that carries the powder particles) is changed, coatings also change as a result, as was observed in the experiments discussed in this section. However, cold spraying is performed when the powder is not heated, but instead, is sprayed at high velocity onto the surface to be coated. The force from this high velocity impact causes partial melting and adhesion, which is demonstrated in Section 7.4 below.

7.4 Impact melting experiments

To investigate the effects of impact melting on GSR particles, the LGG was used in a more conventional way. For this set of experiments, two powder mixes resembling GSR were made. They were then fired using the LGG, utilising both the single-stage and two-stage capabilities. The premise behind these experiments was to determine whether the force that the particles experience upon impact was responsible for the IDGSR morphologies observed in Chapter 5. This was achieved by loading the powder mixes in a sabot and firing them under vacuum at a range of velocities, from $362\,\mathrm{m\,s^{-1}}$ to $2000\,\mathrm{m\,s^{-1}}$. Loading the powders into a sabot and using a vacuum ensured that there was no ignition, or heating of the powders due to air resistance, unlike in the first experiment. Therefore, the morphology of the particles collected would be due solely to the force of impact.

7.4.1 Experimental Set-up

After having examined a number of particles of all morphologies from the previously acquired rim-fire ammunition data, an average relative elemental composition was obtained for the particles that had not fully formed into a sphere. This consisted of the 'characteristic' GSR elements: Pb, Sb and Ba, as well as Cu. The corresponding metallic powders were obtained (with the exception of barium which, due to its reactivity, was replaced by barium nitrate) and sieved within a range of 20 µm - 50 µm.

Two powder mixes were then created using the pre-determined relative elemental composition (75 % Pb, 15 % Ba, 7 % Sb, 3 % Cu by wt %) considered to represent the typical composition of a GSR particle, discussed in Chapter 5. The first projectile powder mix was used after simply mixing the powders, whereas the second projectile powder mix was heated to 913 K and allowed to cool, exceeding the melting point of three out of the four components (Pb, Sb, Ba). This created a more intimate mix, representative of GSR that was molten (or partially molten) prior to impact due to the heat of primer and powder ignition. The powder was then re-ground and re-sieved to the same diameter range as with the unheated, shaken powder (20 µm - 50 µm). The Pb powder that was used to make these mixtures was also fired, providing a set of 'pure' Pb shots that could be used for comparison with the hydrocode modelling discussed in the section 7.5 below.

The rest of the experiment was identical for the powders; they were loaded in a split-sabot and fired at a range of velocities under vacuum (Table 7.3) using the same high-

grade, polished, silicon wafer targets that were used in Experiments 2 and 3 (Chapters 5 and 6 respectively). These silicon wafers were attached to 25 mm aluminium SEM stubs using carbon double-sided adhesive tape. The aluminium stubs with the silicon wafers attached were then loaded in the target chamber prior to evacuating and removed after the LGG had sufficiently aired post-firing.

7.4.2 Results

The EDX maps of the unshot powder mix standards are displayed in Figures 7.15 and 7.16. It can be seen from the elemental composition maps that the merely shaken powder (Figure 7.15) shows distinct individual particles of each element. The original morphology of each powder has also not been affected. Conversely, the heated powder mix (Figure 7.16) shows a more intimate mix has been created, where the individual particles from the elemental powders are no longer discerned. The Pb powder standard and post-firing morphologies can be seen in Figure 7.17.

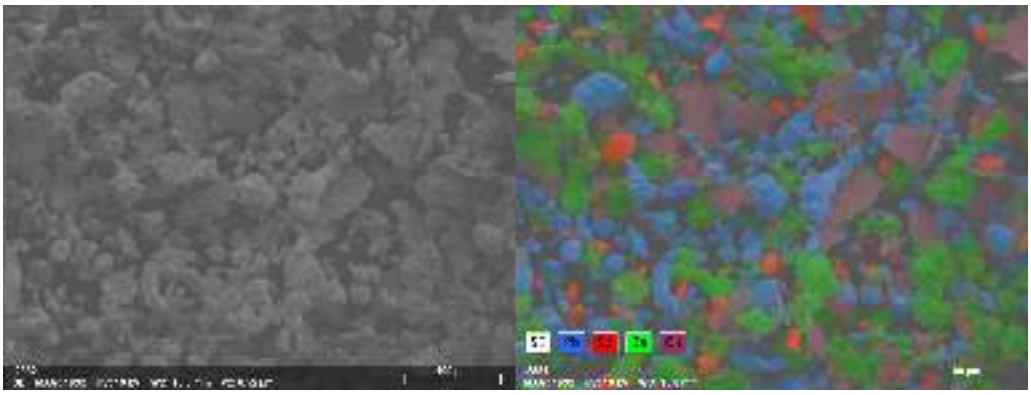

Figure 7.15: FEG-SEM/EDX image and elemental composition map of the 'standard' shaken powder showing the distinct morphologies and individual particles for each elemental powder. *HV:* 10 kV.

Table 7.3 shows the results of the substrate analyses for each powder. For the final Pb powder shot at 362 $\mathrm{m\,s^{-1}}$, no residues were successfully collected. This was due to the powder being too fine and light that it could not make it to the target before dispersing.

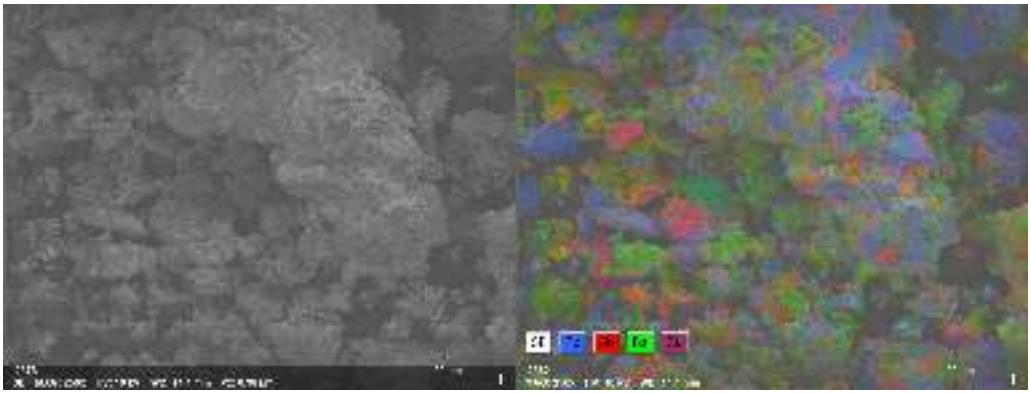

Figure 7.16: FEG-SEM/EDX image and elemental composition map of the 'standard' heated, mixed powder showing the intimate mix that has been created after heating. HV 10 kV.

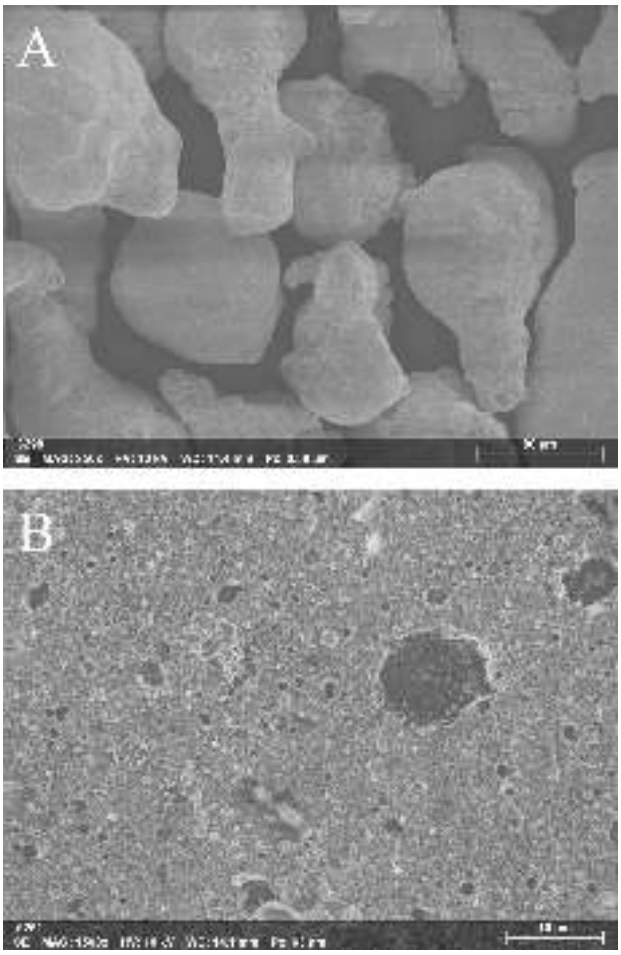

Figure 7.17: FEG-SEM image of the 'standard' Pb powder as provided by Sigma Aldrich. A: Untouched, original Pb powder and B: Pb powder post 520 m s^{-1} shot. HV 10 kV.

Table 7.3: Table showing the results for the different powders and velocities investigated with each primer type using the LGG. The velocities marked with an asterisk (*) indicate the speeds at which unsieved, > 50 μm powders were used. All shots were carried out under a pressure of 0.5 mbar.

Powder Type	Velocity (ms^{-1})	Substrate Damage (Yes / No)	Particle Melting (Yes / Partial / No)
Unheated Shaken Standard	2160	Yes	Yes
	2000	Yes	Yes
	1940	Yes	Yes
	810	Yes	Yes
	809	Yes	Yes
	500	No	Yes
	561*	No	Yes
	427	No	Yes
	374	No	Yes
Heated Mixed Standard	2130	Yes	Yes
	2000	Yes	Yes
	810	Yes	Yes
	789	Yes	Yes
	510	No	Yes
	538*	No	Yes
	405	No	Partial
	369	No	Partial
Pb powder (99.9 %)	520	No	Yes
	503	No	Yes
	362	No	N/A

The results indicate that when firing at $2000\,\mathrm{m\,s^{-1}}$ the substrates used display a significant amount of cratering and surface damage, whereas the $500\,\mathrm{m\,s^{-1}}$ target substrates barely show any residues on them at all. An elemental and morphological comparison of two impacted particles of different velocities is shown in Figure 7.18. Although both particles appear to be molten to an extent, the particle launched at $2000\,\mathrm{m\,s^{-1}}$ exhibits visible, structural damage to the silicon substrate.

At $500\,\mathrm{m\,s^{-1}}$, there are three distinct particle populations present: molten (Figure 7.18B), semi-solid (Figure 7.19A), and partially molten, structured residues with a number of nodules attached to the main body of the particle (Figure 7.19B).

The biggest difference that was observed between the two powders was around $370\,\mathrm{m\,s^{-1}}$. At this velocity, the unheated, shaken powder produced molten particles whereas the residues collected from using the heated, intimately mixed powder were significantly more well-formed (Figure 7.20).

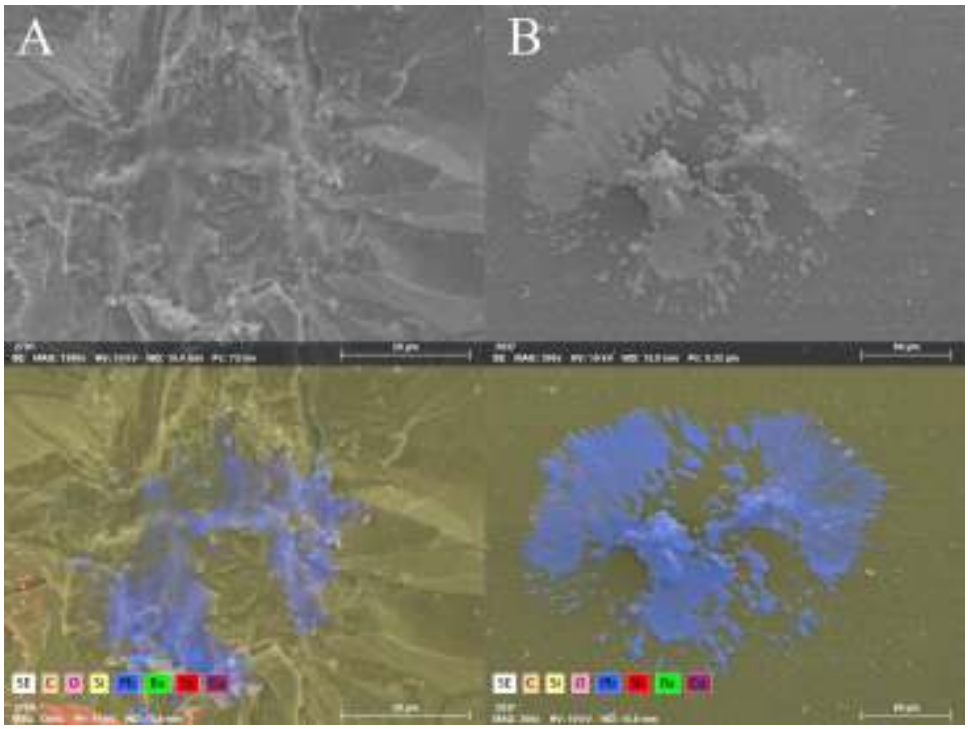

Figure 7.18: FEG-SEM/EDX map images showing molten impact Pb residues formed at different velocities using the shaken, unheated powder mix. A: $2000\,\mathrm{m\,s^{-1}}$ residue inside a silicon crater with some antimony on the outskirts of the crater, B: $500\,\mathrm{m\,s^{-1}}$ residue with a relatively structured particle centre and no evidence of damage to the silicon substrate. HV 10 kV.

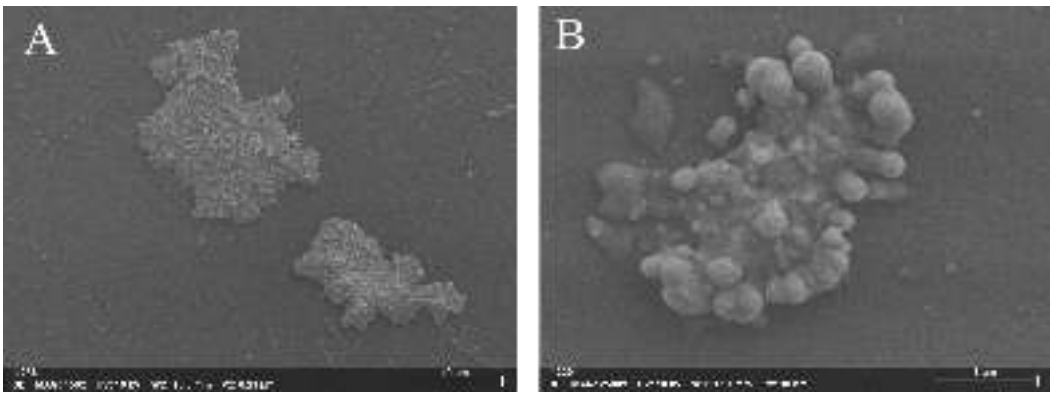

Figure 7.19: FEG-SEM images of the types of residues encountered at $500\,\mathrm{m\,s^{-1}}$ with both the unheated, shaken and heated, intimate powder mixes. A: semi-solid where the particles appear to be on the edge of impact melting due to their flattened appearance and homogeneous matrix (scale: 40 µm), B: partially molten, structured residues with a number of nodules attached to the main body of the particle (scale: 8 µm). The seemingly condensed particles appear to be coalesced via a molten particle segment in the centre. HV 10 kV.

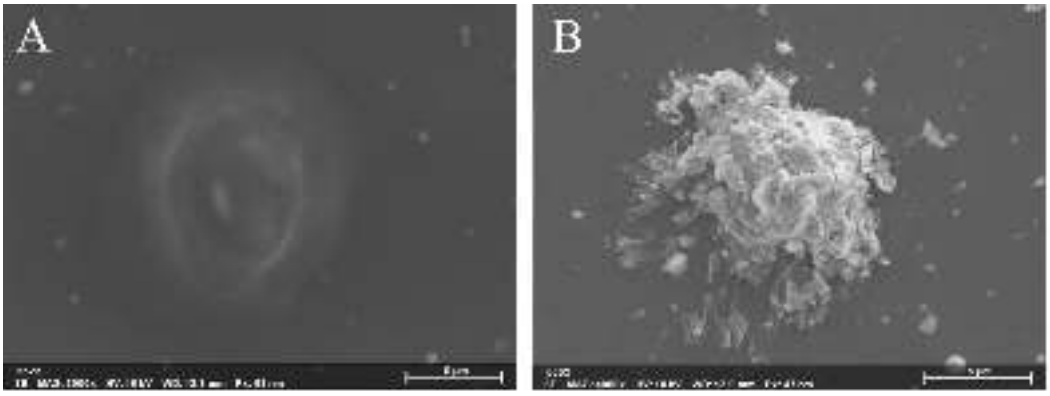

Figure 7.20: FEG-SEM images of the types of residues encountered at approximately 370 m s^{-1} with each powder mix. A: the molten particles observed at 374 m s^{-1} using the shaken, unheated powder (scale: 6 µm), B: the only partially molten, significantly structured residues observed at 369 m s^{-1} using the intimately mixed, heated powder (scale: 5 µm). *HV* 10 kV.

7.4.3 Discussion

Table 7.3 displays the results for the powders fired at different velocities to investigate impact melting. It is clear that at higher velocities, particles melted upon impact and the silicon substrates were damaged (Figure 7.18A). Only once the velocities are restricted to a maximum of 561 m s^{-1} are the silicon substrates unaffected.

As Pb is a 'soft' metal, low speeds of up to 369 m s^{-1} are still sufficient to cause some degree of melting. This is reinforced by comparing the residues in Figure 7.18, where it can be seen that the impacted residues appear to be molten at both velocities examined. In Figure 7.18B, the impacted side of the particle is molten, however the remaining part of the particle appears to retain its structure as the impact energy dissipates. Figure 7.19, on the other hand, shows a lead particle that has collapsed in on itself (A) and another that boasts multiple globular nodules that are attached to the main body matrix (B). The powders all contained spheroidal particles of a diameter between 20 µm - 50 µm, and so despite the lack of obvious melting, it is evident that the shape of the particle exhibited in Figure 7.19A has been deformed either in-flight, or due to the force of the impact, which could only occur if the particles were in a semi-molten state when they hit the target. Therefore, despite their sometimes structured-like appearance, it would appear as though at 500 m s^{-1} the powder residues are on the verge of melting prior to impacting the target. The range of molten states observed (from solid to completely liquid) at nominally the same impact velocity can, potentially, be explained by the heterogeneous compressional heating of the individual particles in the projectile mix during the launch process.

The most substantial difference observed with the two powders was at $\sim$ 370 m s^{-1}.

Here, the shaken, unheated powder still produced primarily molten residues, whereas the residues collected when using the intimately mixed, heated powder are significantly more structured and only exhibit partial melting. This is likely due to the difference in the powder mixes as Pb had been shown to melt at even lower velocities. In the unheated, shaken powder mix Pb exists as its own individual elemental particles (Figure 7.15). However, when heated and mixed thoroughly, the elemental powders have melted into each other, forming particles of mixed compositions. The addition of these elements would strengthen the 'soft' Pb, producing the more structured morphologies observed at these speeds for these projectiles.

7.5 AUTODYN Hydrocode Modelling

The experimental data described above shows that the particles were predominantly either molten on impact, or melted during the impact due to the liquid appearance of the residue. To gain insight into the processes going on during impact, as well as the initial launch of the projectile, hydrocode modelling was performed using Ansys' AUTODYN software (Hayhurst C.J. & Clegg R.A., 1997). The goal was to investigate the temperatures experienced during the launch and subsequent impact, to determine the point at which significant impact melting of the projectile material began.

7.6 Introduction

Computational modelling has been employed to gain insight into the behaviour of materials while undergoing an impact. During the experimental studies of impacts in a laboratory environment, it is impossible to measure and determine multiple factors going on during the impact event, including temperature changes, due to the very fast (and small size) scales of the event. However, computational modelling can assist with this.

Constitutive models (also known as strength models) can be used to determine the effects impacts have on target materials. To achieve this, the models relate the amount of distortion that occurs as a result of the stress the material experiences, by calculating the total stress applied compared to the yield strength of the material. There are a number of constitutive models which incorporate some (or all), of the variables that can affect yield strength, such as temperature, pressure and size. Steinberg-Guinan

(Steinberg D.J. et al., 1980) was the constitutive model used for the Pb projectile in these simulations, and the Johnson-Holmquist (Johnson G.R. & Cook W.H. (1983); Holmquist T.J. et al. (2016)) constitutive model used for the float-glass target.

Numerical solvers can be used to provide information during the simulations by utilising the conservation equations, equations of state and constitutive models. The solvers that were used were Lagrangian (target) and Smoothed Particle Hydrodynamics (SPH) (projectile). Both of the numerical solvers used utilise discrete computational cells, which allow the computer to divide the objects, and their respective materials, into fewer cells. The behaviour of the individual cells is governed by the conservation equations, the materials' equations of state, and constitutive models, which reproduce the material's response.

The primary difference between Lagrangian solvers and SPH is that Langrangian solvers use a mesh, whereas the SPH solver is a mesh-less grid (Figure 7.21). When using a Lagrangian solver, the mesh generated is filled in the defined geometries of the projectile and target, where the size of the cells can be selected accordingly. The cell has a fixed mass of material but the mesh can deform in response to resulting external and internal forces experienced during impact. On the other hand, SPH solvers populate the defined particle areas with individual nodes that act as pseudo-particles, defining the geometry. These cells are considered physical fluid particles and the nodes can be tracked even if they are separated by large distances (Zukas J., 2004).

Figure 7.21 shows that Lagrangian cells can experience extreme deformation, making Lagrangian solvers useful in modelling impact target substrates. However, SPH solvers show the interaction between objects, defining the geometry, and can be tracked even when separated by large distances (Zukas J., 2004) making SPH particles ideal for modelling particle fragmentation and deformation.

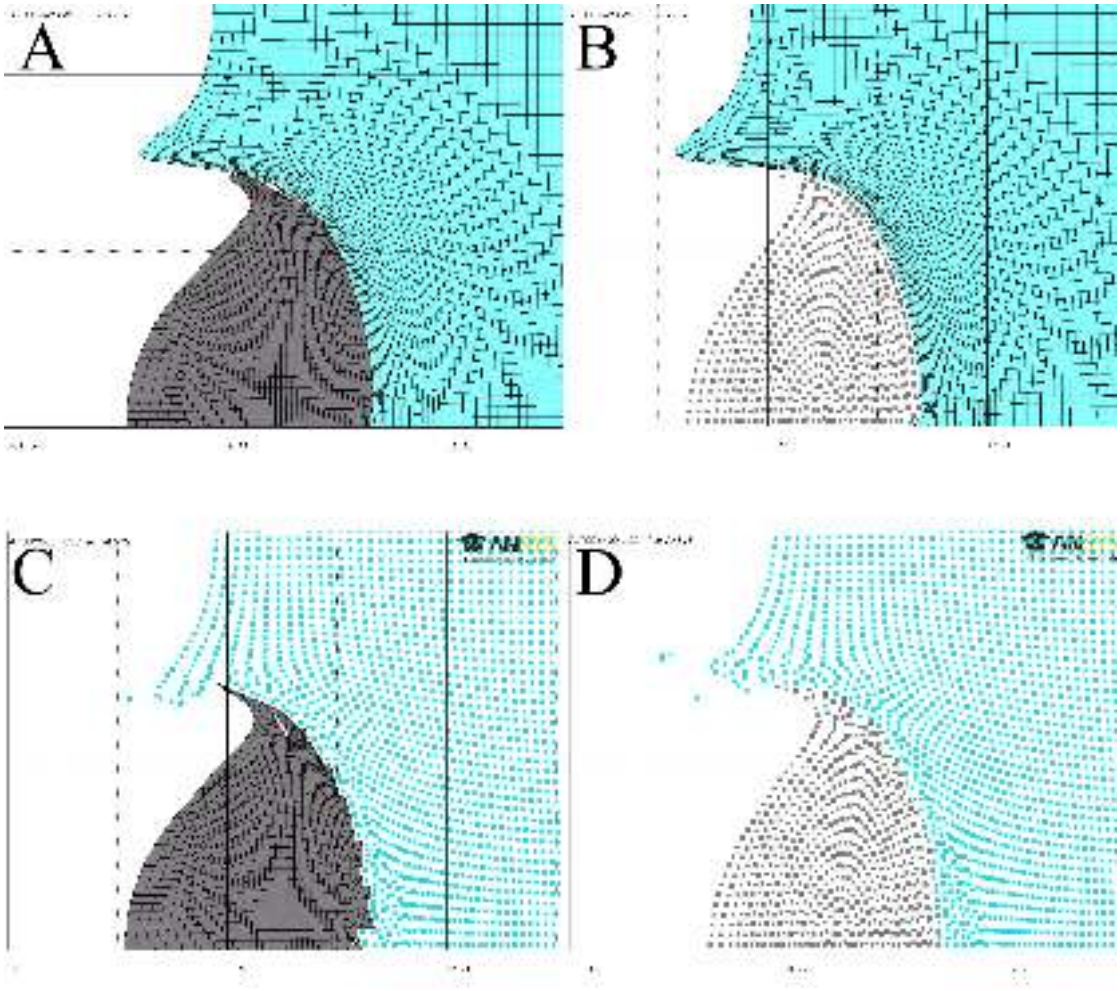

Figure 7.21: Pictures, courtesy of Mark Price (Price M.C. et al., 2010), showing differing solver combinations at t = 3 ns after impact. 'P' denotes projectile and 'T' denotes target. A: Lagrangian (P) – Lagrangian (T), B: SPH (P) – Lagrangian (T), C: Lagrangian (P) – SPH (T), D: SPH (P) – SPH (T). Note: B was the chosen solver combinations for the simulations presented in this section.

7.7 Materials & Methodology

The capabilities of the Ansys' AUTODYN software were utilised to investigate the processes going on during impact, as well as during the initial launch of the projectile. All the hydrocode modelling simulations that were ran and presented in this section were done so using 100 % Pb spherical projectiles. These Pb projectiles incorporated a Steinberg-Guinan constitutive model (Steinberg D.J. et al., 1980) which encompassed both strain-hardening and thermal softening. The other metals were not included in any of the simulations as some lacked strength models, and so the projectile would

behave like a liquid, rather than a solid. Moreover, as the vast majority of the particles examined in Sections 7.3 and 7.4 above were predominantly Pb, the use of 100 % Pb projectiles was an appropriate choice.

One hypothesis was that during the launching process (where the projectile can experience accelerations of $\sim 1 \times 10^6$ m s^{-2}) the projectile was subjected to sufficient force to experience partial or full melting, and thus was exiting the sabot in an already-molten state. To test this compressional heating hypothesis, a 2-D multi-material Euler model was set up to simulate the acceleration by a driver gas at an initial pressure of 20 kbar of a Pb-loaded sabot down the 0.7 m long launch-tube of the Kent LGG. Gauges were placed within the Pb to measure the velocity, pressure (and thus temperature) of the projectile during the acceleration process. The ambient (pre-launch) temperature was set to 300 K.

To investigate the temperatures that Pb particles reached during impact, a range of 2-D models were set up. The aforementioned Pb projectiles were modelled using SPH, which subsequently impacted a float-glass target Lagrangian mesh (Figure 7.22). As silicon was not an available target option, float-glass was the closest material that could be used instead. The Pb spherical projectiles were set to a diameter of 50 µm, with temperature gauges placed evenly every 2.5 µm across the particle (Figure 7.23) to measure the temperatures experienced throughout the particle during impact. The ambient temperature was set to 300 K and the models were ran for 1000 × natural time-scale (Equation 7.1) using different velocities- 2000 m s^{-1}, 1000 m s^{-1}, 750 m s^{-1}, 500 m s^{-1} and 350 m s^{-1}.

The rationale for the use of an SPH projectile was that initial modelling carried out using a Lagrangian mesh for the projectile resulted in numerical erosion of highly distorted cells. These were the cells with the highest temperature, leading to the model 'running cold'. By changing to an SPH solver, the problem of numerical erosion is not encountered and it is much more suitable for modelling the disruption of small impactors travelling at high speed. Similar models using a range of solvers have been used successfully to model the splat formation of metal aerosols during thermal and cold spraying coating processes (Zhang M.Y. et al. (2008); Yildrim B. & Müftü S. (2012); Fauchais P. et al. (2004); Kumar S. et al. (2017)).

The effects of different temperatures and velocities on the morphologies of the residues were also investigated. 3-D simulations were ran using the same 50 µm Pb projectiles as before, with a melting point of ∼600 K and resolution of 20 cells across the radius of the projectile. Each simulation was ran for 1000 × τ seconds, where τ

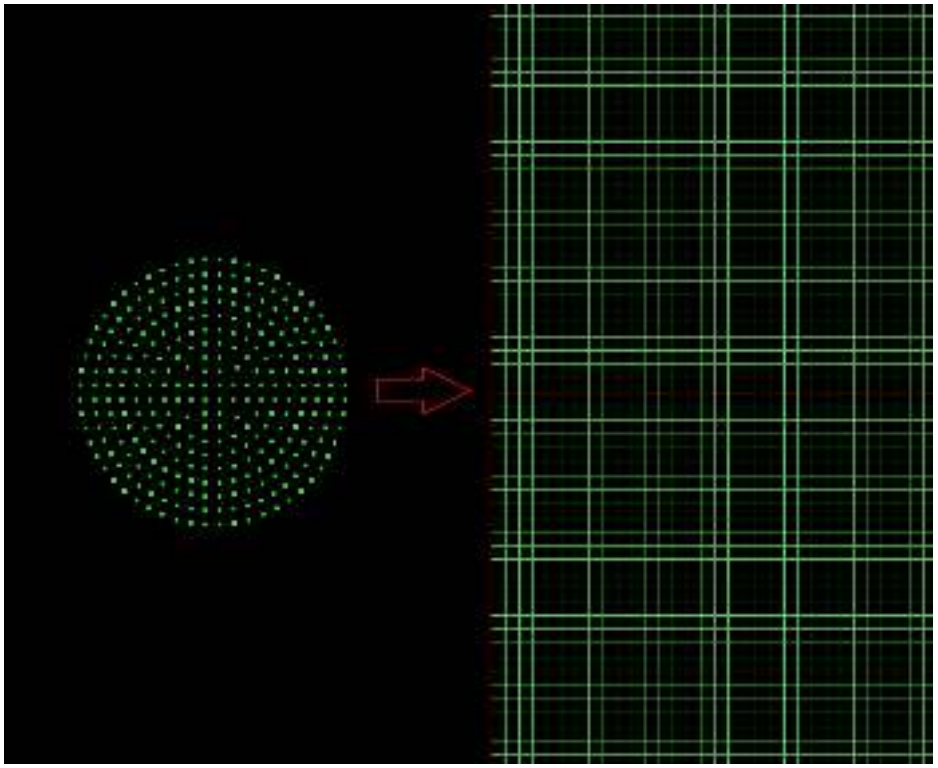

Figure 7.22: Picture showing the Ansys' AUTODYN simulation set-up of a 50 µm SPH-modelled, spherical, Pb projectile prior to impacting a Lagrangian float glass target mesh.

represents the 'natural time-scale' (Melosh H.J., 1987) determined by Equation 7.1:

$$\tau = \frac{radius}{velocity} \tag{7.1}$$

where,

τ = 'natural time-scale', i.e. the amount of time it takes for the event to take place experimentally (s)

radius = radius of the projectile (m)

velocity = velocity at which the projectile is travelling upon impact ($m\,s^{-1}$).

The projectiles impacted the float glass target in two different ways:

- The velocities at which the projectile impacted the target were changed while the initial temperature of the projectile remained constant
- The initial temperatures of the projectile were changed while the velocity at which the projectile impacted the target remained constant

For the first set of simulations investigating the effect of velocity on particle morphologies, the initial projectile temperature was maintained at 300 K. The velocities

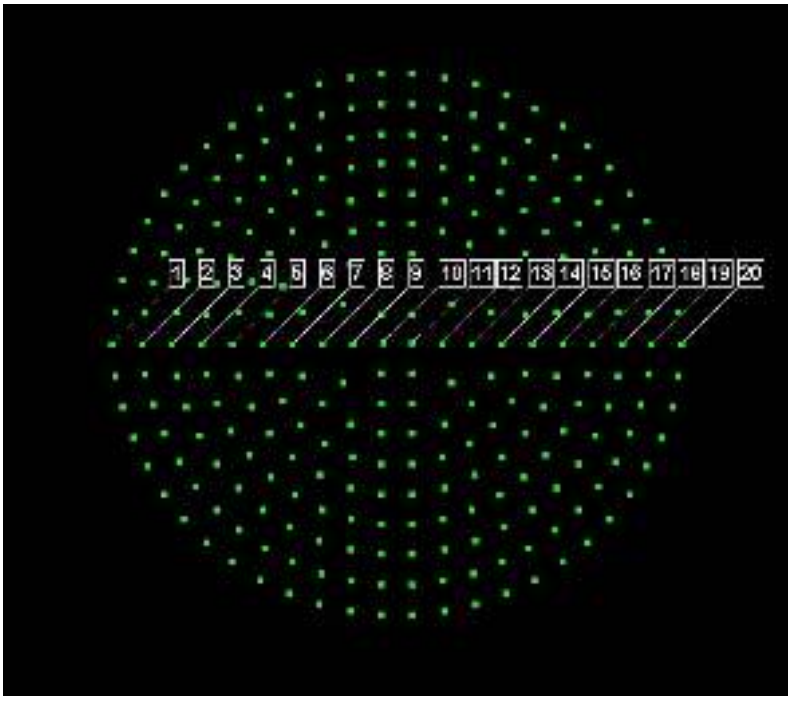

Figure 7.23: Picture showing the thermal gauges placed every 2.5 µm across a 50 µm SPH-modelled Pb projectile. Gauge 1 is located at the back of the projectile whereas Gauge 20 sits at the front of the projectile and would impact the target first.

investigated at this temperature were: $2000\,\mathrm{m\,s^{-1}}$, $1000\,\mathrm{m\,s^{-1}}$, $750\,\mathrm{m\,s^{-1}}$, $500\,\mathrm{m\,s^{-1}}$, $400\,\mathrm{m\,s^{-1}}$, $350\,\mathrm{m\,s^{-1}}$, $200\,\mathrm{m\,s^{-1}}$ and $100\,\mathrm{m\,s^{-1}}$.

The second set of simulations had a more selective approach. Due to the amount of time required for the simulations to run ($\sim$ 2 days per simulation), the velocities at which the change in initial temperature was investigated were restricted to $1000\,\mathrm{m\,s^{-1}}$, $750\,\mathrm{m\,s^{-1}}$ and $350\,\mathrm{m\,s^{-1}}$. The decision to choose these velocities came after the completion of both the experimental investigations and first set of simulations described above. During the experimental tests, it was observed that at speeds over $\sim$$1000\,\mathrm{m\,s^{-1}}$ the silicon shatters. Therefore, to stay in accordance with the experimental observations, $1000\,\mathrm{m\,s^{-1}}$ was chosen as the maximum velocity to be tested, $350\,\mathrm{m\,s^{-1}}$ was the minimum and $750\,\mathrm{m\,s^{-1}}$ was the intermediate velocity investigated as a comparison with the centre-fire ammunition.

For each of the impact velocities specified in this section, three initial temperatures were examined: 600 K, 500 K and 300 K. These initial temperatures were chosen to test whether the state that the Pb projectile was in during the launching process would affect the final morphologies created during impact. 600 K is the melting point of lead, and so implied an already molten projectile, whereas at an 'ambient' temperature of 300 K the projectile is solid during the initial launch process. The choice to use

500 K came from a desire to model a partially molten projectile at the time of launch. These three temperatures allowed for the effects of the initial physicality of GSRs to be investigated at each velocity.

7.8 Results

The results obtained from the hydrocode simulations have been separated into relevant subsections and displayed below. The subsection entitled "Compressional heating and peak temperature determination" contains the data obtained from 2-D simulations encompassing temperature gauges whereas "Investigating impactor velocity and initial temperature" focuses on the 3-D simulations and morphological results.

7.8.1 Compressional heating and peak temperature determination

Figure 7.24 shows the results of the simulation investigating compressional heating of the projectile upon launch. The simulation gave a final projectile velocity of $1600\,\mathrm{m\,s^{-1}}$, however, it should be noted that the sabot was still being accelerated at the point it exited the launch tube.

The results from the simulations investigating the temperatures experienced during impact are also included in this section. Figure 7.25 shows the results obtained from the temperature gauges for the particles flying at each velocity. However, these temperatures are only experienced for a very short amount of time, and may not be sufficient to melt a projectile (see Chapter 8 for a detailed analysis).

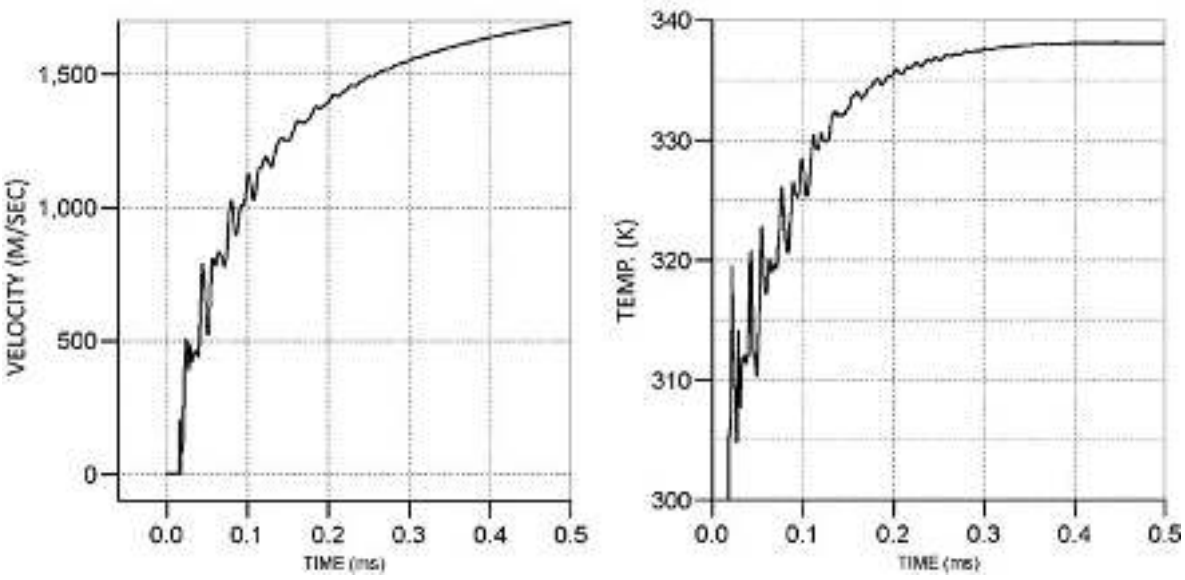

Figure 7.24: Graphs showing the modelled velocity (left) and temperature (right) of a solid Pb-projectile during acceleration down the launch tube of the Kent LGG.

Table 7.4 gives the modelled temperature rise of a 50 μm diameter sphere impacting a silicon target at a range of impact velocities. The quoted "ΔT" gives an indication of the amount of heating experienced averaged across the whole projectile.

A graph showing the temperature changes on the front and back of the projectile at each speed is displayed in Figure 7.26. The black line refers to the temperature gauges at the back of the projectile, whereas the blue line represents the temperature gauges at the front of the projectile.

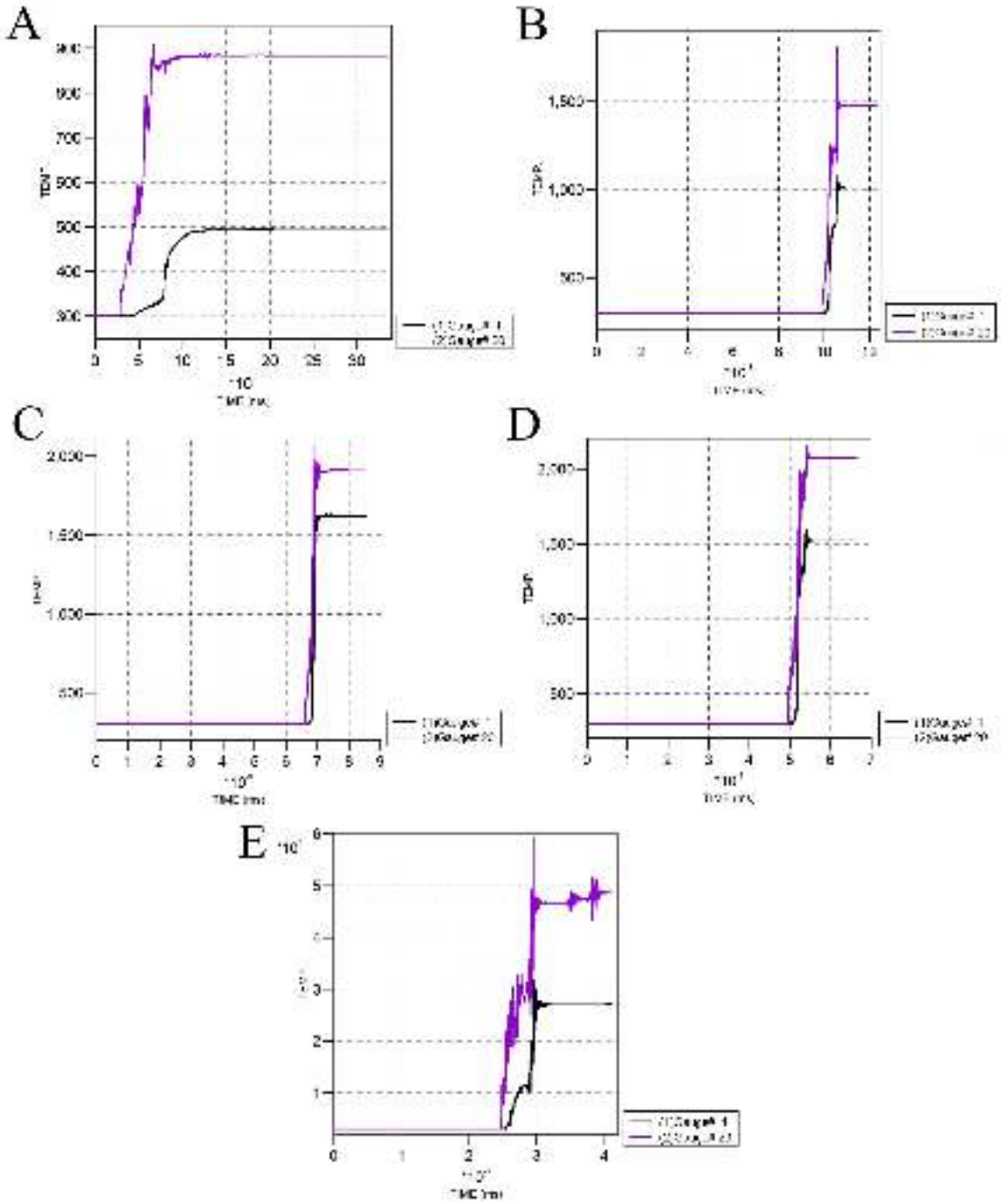

Figure 7.25: Graphs showing the modelled temperature of a solid Pb-projectile during impact. Gauge 1 was at the back of the projectile, gauge 20 was at the forefront of the projectile. A: 350 m s^{-1}, B: 500 m s^{-1}, C: 750 m s^{-1}, D: 1000 m s^{-1}, E: 2000 m s^{-1}. Note: the y-axis of 'E' is in thousands K.

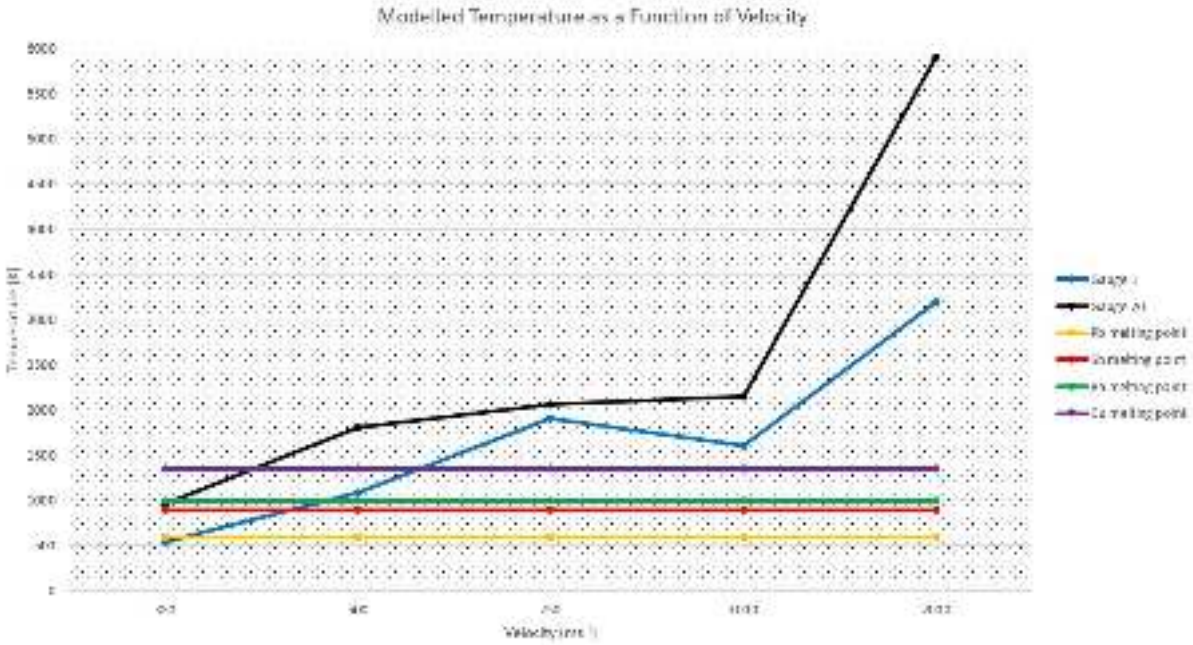

Figure 7.26: Graph comparing the modelled temperature gauge values for the projectiles at each velocity. The melting points of the GSR elements investigated are also included for reference. Blue: gauge 1 (back of projectile), black: gauge 20 (front of projectile), yellow: Pb melting point, red: Sb melting point, green: Ba melting point, purple: Cu melting point.

Table 7.4: Table comparing the results from the 2-D impact simulations of a solid 50 µm diameter Pb sphere onto a silicon target. ΔT represents the temperature increase of the whole sphere if the temperatures of all nodes are averaged.

Impact Velocity (ms^{-1})	ΔT (K)
200	313
350	451
500	1146
750	1686
1000	1581
2000	4757

7.8.2 Investigating impactor velocity and initial temperature on particle morphology

The results of the 3-D hydrocode modelling are displayed in this section. For these simulations, the initial temperature of the projectile was maintained at 300 K. Figure 7.27 shows that the lower velocities exhibit a splat-like morphology that increased in size until approximately 750 $m\,s^{-1}$, after which more 'confined' morphologies are observed. The results from the 3-D simulations investigating the morphology of the

residues post-impact as a function of impactor temperature are displayed in Figure 7.28. Three temperatures were investigated at each velocity: 600 K, 500 K and 300 K.

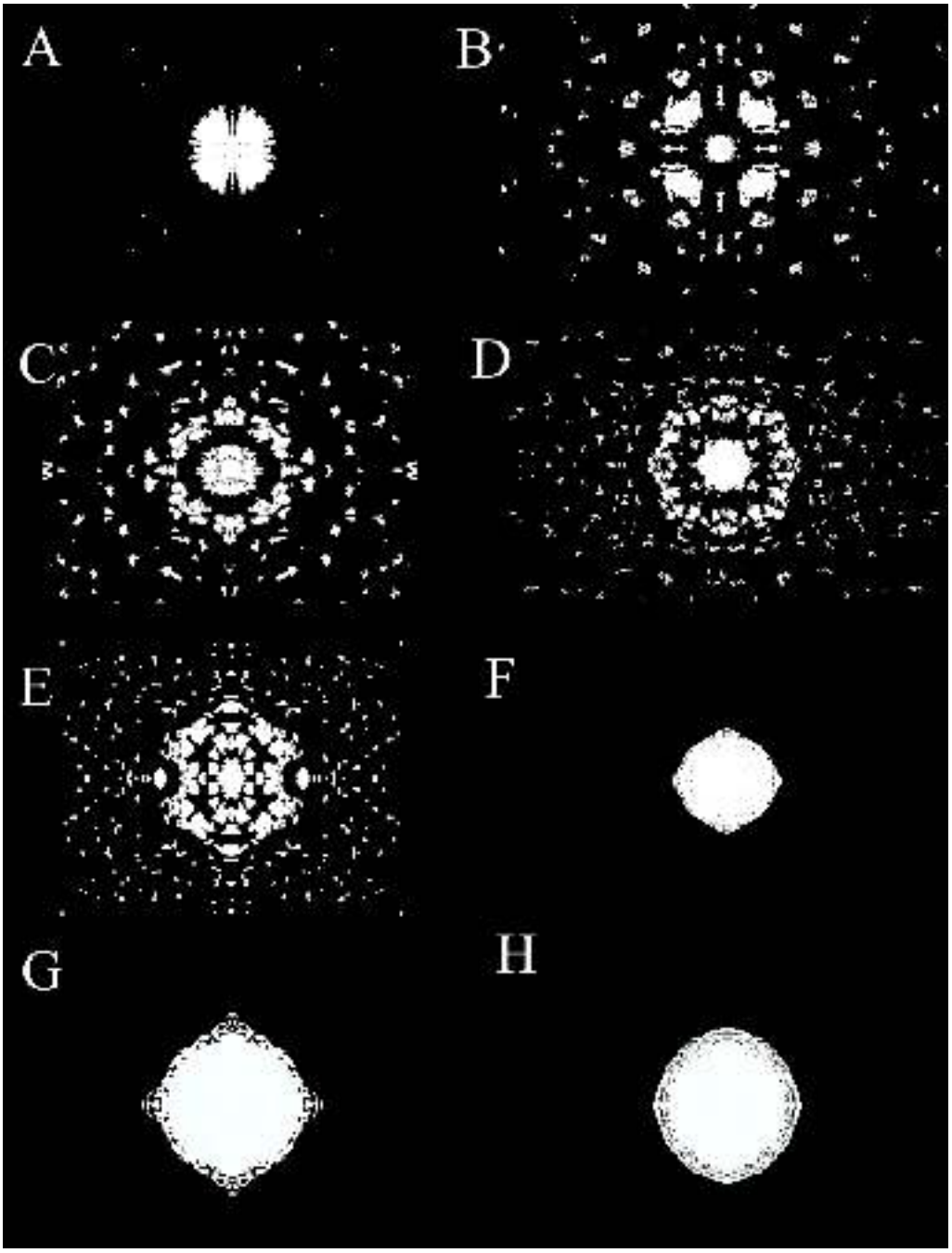

Figure 7.27: Hydrocode modelling results showing the particle morphology as a function of impactor velocity for an initial fixed impactor temperature of 300 K. A: 100 m s^{-1}, B: 200 m s^{-1}, C: 350 m s^{-1}, D: 400 m s^{-1}, E: 500 m s^{-1}, F: 750 m s^{-1}, G: 1000 m s^{-1} and H: 2000 m s^{-1}. The images are to the same scale with each panel being 400 μm across. The images show the impacted SPH particle morphologies at the end of each respective hydrocode modelling simulation run.

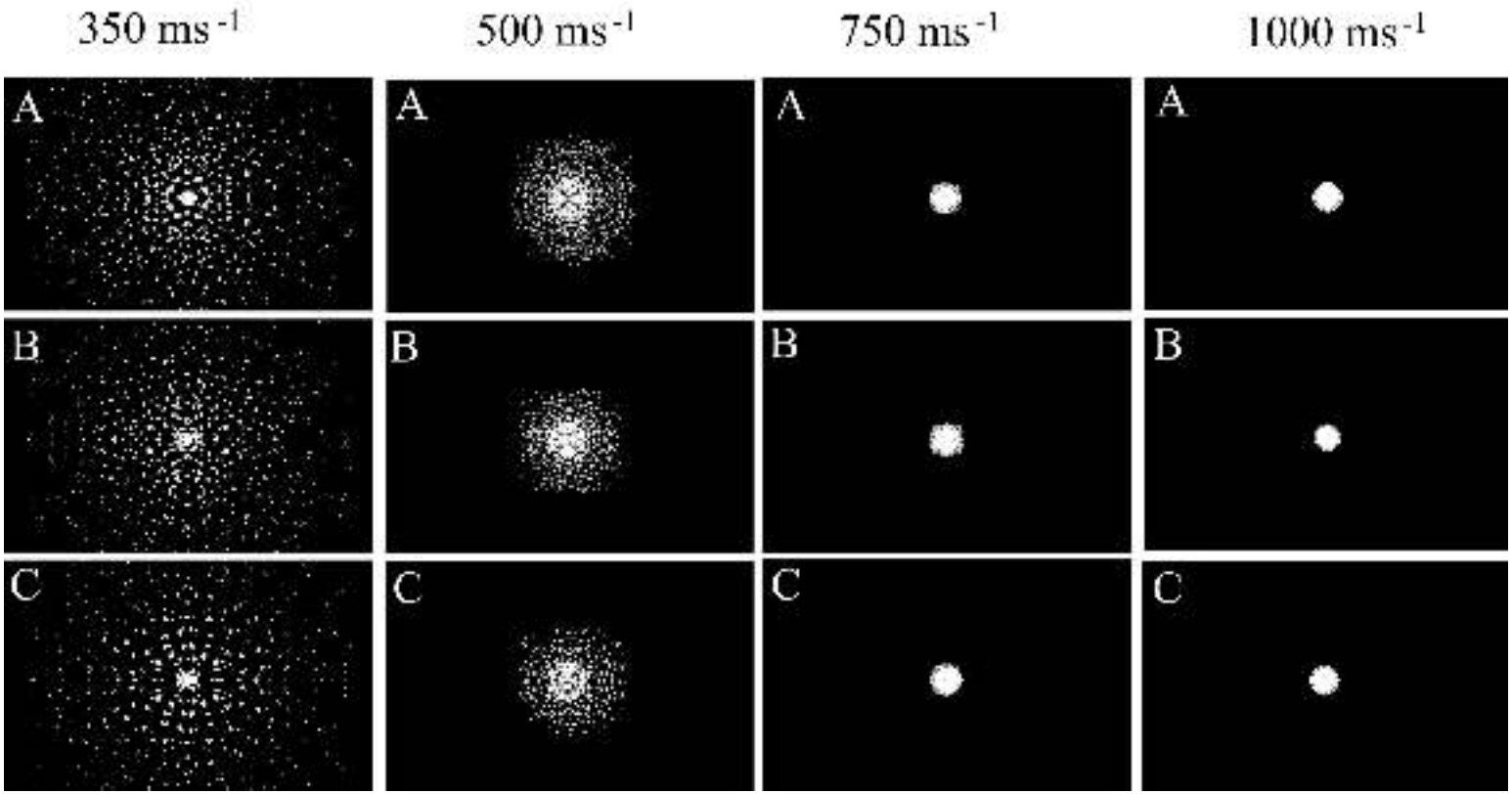

Figure 7.28: Hydrocode modelling results showing the particle morphology as a function of initial impactor temperature for each impact velocity. Left: $350\,\mathrm{m\,s^{-1}}$, middle left: $500\,\mathrm{m\,s^{-1}}$, middle right: $750\,\mathrm{m\,s^{-1}}$, right: $1000\,\mathrm{m\,s^{-1}}$. A: 600 K, B: 500 K and C: 300 K. The images show the impacted SPH particle morphologies at the end of each respective hydrocode modelling simulation run.

7.9 Discussion

The results of the simulation investigating compressional heating suggest that a solid Pb projectile would undergo some heating due to the launch acceleration. However, the amount of heating would be modest ($\sim 40\,\mathrm{K}$ for a launch velocity of $1600\,\mathrm{m\,s^{-1}}$) which would be insufficient to cause any appreciable softening or melting. However, during the impact melting experiments, the metal powder had been sieved and was loosely packed into the sabot forming a pseudo-porous projectile. Modelling of impacts into porous bodies (Davison T.M. et al., 2010) have shown that the temperature experienced by a porous target can be significantly higher than for impacts into solid targets. Therefore, an additional, fully 3-D, simulation (with the same spatial resolution as the 2-D simulation) which modelled the projectile as a discrete set of Pb particles (with an overall porosity of ~ 50 %, based on the void spacing inside an actual sabot filled with metallic powder) confined within the sabot was run. The results of this simulation show a much wider range of temperatures within the projectile material, with a maximum of $\sim 750\,\mathrm{K}$, and significant compaction of the projectile particles during the launch acceleration. It is therefore likely that during launch the individual particles making up the projectile experienced differing degrees of heating and that some of the particles could be significantly softened, or even totally molten, at the time of impact.

Table 7.4 indicates a linear relationship between impact velocity and the average heating experienced by the projectile. This is expected as the higher the velocity with which a projectile impacts the target, the higher the energy of the impact. The temperature gauge data also follows this pattern (Figure 7.23), with the temperature at the front of the projectile increasing with increasing velocity.

Investigating the splat formation as a function of impact velocity shows a clear evolution, shown in Figure 7.27. At lower velocities, the particles stay fairly structured and begin to form molten residues as the impact velocity is increased. However, from an impact speed of $500\,\mathrm{m\,s^{-1}}$ and up $2000\,\mathrm{m\,s^{-1}}$, the morphologies become dense and constricted. This is due to crater formation in the target material. As the crater forms, the projectile ejecta is forced back along the line-of-flight and no longer lands on the target surface, additionally the crater contains the projectile material so it remains localised. These data are consistent with what is observed with silicon breaking at $560\,\mathrm{m\,s^{-1}}$.

The 3-D models that were ran to look at the splat formation as a function of impactor temperature (Figure 7.28) show a distinct change in the particle morphology as well. This change is observed for the impact speeds at $750\,\mathrm{m\,s^{-1}}$ and $1000\,\mathrm{m\,s^{-1}}$.

The results of this hydrocode modelling shows a definite progression from a solid splat state, to a very liquid state where the projectile material is totally molten and shows a fine filigree patination, which has been observed experimentally with nylon and glass projectiles (Hörz F. et al. (1994); Loft K. et al. (2013)).

The results of the hydrocode modelling capture the observed evolutionary morphologies of Pb splats. Most importantly the results help to interpret the range of morphologies seen for the fixed impact velocity experiments: i.e. that a mix of solid, semi-solid and molten Pb residues were observed which may be due to the inhomogeneous compressional heating experienced by the projectile during the LGG launch process. They also reveal that the size of the splat seems to decrease as the impact speed is increased, likely due to the projectile material being ejected back along the impact direction and not landing on the target material, and/or the formation of a crater in the silicon, confining the projectile material.

Overall, the LGG experiments show that convective cooling is the dominant cooling process (rather than radiative cooling) during a projectile's flight. Moreover, the projectiles must have impacted the silicon surface at speeds $< 500\,\mathrm{m\,s^{-1}}$ as no damage is observed on the experimental samples, and the AUTODYN modelling for impacts onto glass give similar results. However, Price M.C. et al. (2014) have found that "bruising" occurs on the same Si wafer targets at speeds as low as $362\,\mathrm{m\,s^{-1}}$. As no substrate "bruising" is observed during the experiments presented in this section, it is likely that GSR particles travel at a speed below $362\,\mathrm{m\,s^{-1}}$. Moreover, different ambient atmospheres (such as N_2 and CO_2) seem to give rise to differing GSR morphologies, indicating a chemical interaction with the atmosphere. Finally, at velocities about $350\,\mathrm{m\,s^{-1}}$, the modelling indicates that a significant proportion of the impactor reaches its melting point. However, the temperature increase is a sensitive function of the impact speed and the modelling does not account for the energy required for a phase change in the material. Therefore a particle could be 'flash heated' to several thousand kelvin for a fraction of a second, but still remain solid. This is reinforced by the results of firing the shaken, unheated powders at different speeds and only seeing significant melting of Pb at $\approx 500\,\mathrm{m\,s^{-1}}$, described in detail in Chapter 8.

Understanding the formation of metallic particles can aid in understanding how metals mix through the air and in different pressure systems, giving insight and applications in materials science, i.e. aerosols and a range of coating systems from hot (Brandolt C.D.S. et al., 2017), warm (Kuroda S. et al., 2008) and cold (Stoltenhoff T. et al., 2002) spraying, all of which rely on a spray of metallic droplets through a carrier gas to create a coating, and the properties of the coating are a function of the aerosol's environment.

Chapter 8

Discussion

This thesis has described a series of experiments and their results in an attempt to better understand the formation and distribution of GSR particles. In this chapter, some analyses are provided to help evaluate these results.

8.1 The size distribution variance as a function of distance from the firearm

The results of the experiments investigating the distribution of particles, presented in Chapter 4 demonstrate that 'unique' (or 'characteristic') GSR particles are identifiable up to 400 cm from the firearm (the maximum distance sampled) when using the CCI Mini-Mag ammunition and Buck Mark long rifle pistol. Figure 4.7 suggests that the maximum number of residues collected was between 40 cm and 60 cm from the firearm, for all three INCA GSR classification ranks ('unique', 'indicative' and 'environmental'). This is corroborated in Chapter 5, where the maximum number of residues collected on the silicon substrates, using the same firearm and ammunition combination, is again between 40 cm and 60 cm. Ditrich H. (2012) investigated the influence of weapon type on the distribution of GSR and found that in both revolvers and pistols, different phases of the plume formation can be distinguished (Figure 8.1). Although Ditrich H.

(2012) did not test the specific firearm and ammunition combinations used in these experiments, the author states that the plume formation sequence pattern was "rather similar" in all of the investigated guns, with the sizes and volumes of the plume differing between various weapons and ammunition types.

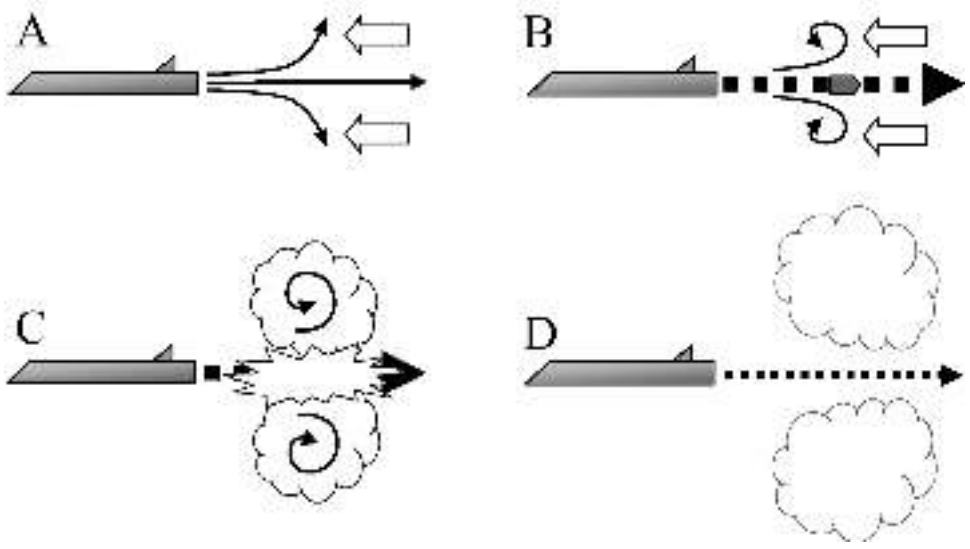

Figure 8.1: Diagram (not to scale) by Ditrich H. (2012) of the general sequence of the plume formation process at the muzzle of small firearms. The phases are not distinct steps, but rather show the continuous transition from one phase to the next. A: cone / vortex formation, B: projectile emission, C: jet blast following projectile, D: gas "bleeding" from barrel.

As is illustrated in Figure 8.1, the author states that initially gas, unburned propellant and GSR particles are ejected from the muzzle in a rapid, narrow stream, approximately the size of the calibre. Shortly afterwards, this stream of gas and particles forms into a cone with an angle up to 145° due to the resistance of the surrounding air. A ring-like cloud forms from this stream which increases in size by internal expansion, and from additional gases from the barrel. The projectile only causes minor turbulence in the particle stream from the barrel as the particle stream is initially slightly faster than the bullet itself. However, smoke and GSR particles are decelerated much more, in comparison to the projectile, due to their small size. The jet blast following the projectile consists primarily of propellant, expanding gases, as well as burnt and unburnt ammunition load components, the reaction of which results in the main blast of the weapon. Only a small proportion of this jet blast consists of 'characteristic' GSR particles. Ditrich H. (2012) suggests that the intensity of the blast effect largely depends on ammunition type and barrel length. However, while the main direction of gases, fire and particles is in the direction of the shot, the blast is also observed to spread laterally (although to a lesser extent) and disperses material, along with the

components of the (initially) ring-like cloud. The final stage of the process, as indicated in Figure 8.1D, is when smoke and particulates "bleed" from the barrel. By this point of the firing process, the stream of gases and particles decreases in both velocity and quantity. Additionally, as unburnt propellant particles are no longer present, the blast ends. However, smoke and, occasionally, larger burning particulates will gradually emerge from the barrel.

Here, we undertake a theoretical analysis to explain (or partially explain) the distribution of GSR particles observed in the experiments described in Chapter 4. Investigating the distribution of GSR particles over the 400 cm range sampled, two possibilities are encountered. Firstly, a sphere (representing a spheroidal GSR particle) has its own velocity and is travelling in a stationary medium, i.e. air (Figure 8.2).

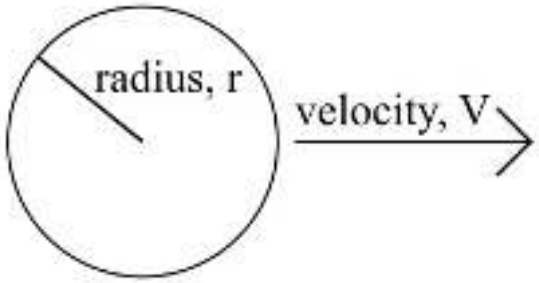

Figure 8.2: Diagram (not to scale) showing a sphere of radius 'r' with its own velocity travelling in a stationary medium.

Air resistance is therefore an opposing motion as given in the drag force equation.

$$\mathrm{F_{drag}} = \frac{1}{2}\rho C_d A v^2 = mass \times acceleration \tag{8.1}$$

where,
ρ = density of air, $1.225\,\mathrm{kg\,m^{-3}}$
$\mathrm{C_d}$ = drag coefficient of sphere, 0.5
A = cross-sectional area of sphere, πr^2 (m^2)
v = velocity of particle travelling through air $(\mathrm{m\,s^{-1}})$.
Therefore,

$$acceleration \propto \frac{1}{r} \tag{8.2}$$

This suggests that the smaller the sphere, the faster it decelerates, which makes sense since air resistance is discounted for macro-sized objects.

The second possibility is that the sphere is being dragged ('entrained') in a flow of gas, and only has a velocity as it is being pushed (Figure 8.3).

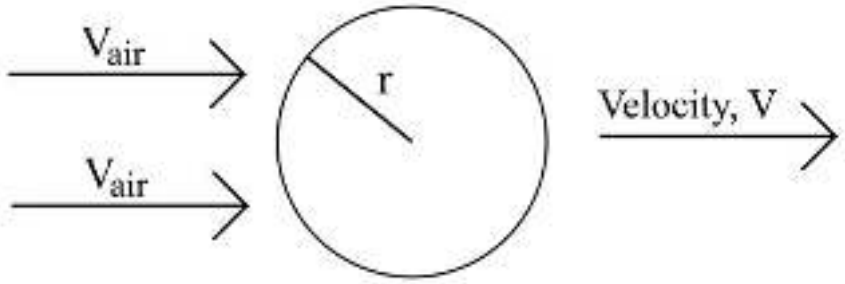

Figure 8.3: Diagram (not to scale) showing a sphere of radius 'r' being entrained in a flow of gas.

Now the 'drag' becomes a 'push' and small particles will get pushed further than large particles (Figure 8.4).

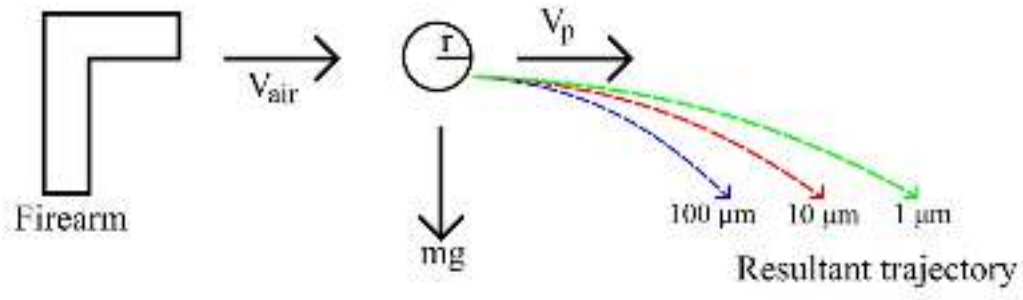

Figure 8.4: Diagram (not to scale) showing the possible particle trajectories for different sized particles, assuming they are entrained in a flow of gas.

The first possibility would lead to observation of large IDGSRs at longer distances, and no small IDGSRs, or spheres, at longer distances, which is not seen in this set of experiments (Figure 4.8). However, the second possibility would lead to the observation of large splats closer to the firearms and fewer at larger distances, which is (generally) observed. Therefore, it seems very likely that the spheres are travelling by being entrained in the gas from the firearm. This corresponds to what Ditrich H. (2012) observed in the first steps of a firearm being discharged, where a rapid, narrow stream of gas, propellant and GSR particles are expelled from the barrel.

If spheres are being entrained in the gas from the firearm, there are potential implications for cooling times due to convection/conduction to the air. In the first scenario, the cooling would be rapid as heat is being lost with the fast flowing air,

whereas in the second scenario, the particle is moving with the air and so the cooling time would be less. This is discussed in the section "Heating and cooling mechanisms" below.

By considering the forces on a particle, its trajectory can be quantified based on its velocity and size (Figure 8.5).

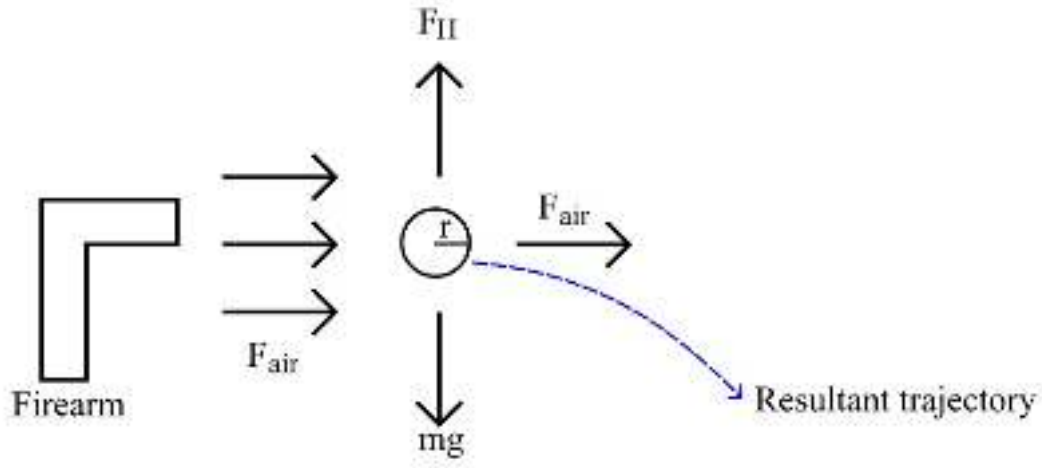

Figure 8.5: Diagram (not to scale) showing the particle trajectories that can be crudely determined based on a particle's velocity and size.

F_{air} = push force from gases expelled by the firearm. This will fall off quickly as the gases expand into the environment.

Here, we assume:

$$F_{air} = F_0 \exp(-kt) \tag{8.3}$$

where,

t = time

k = unknown constant that controls the blast duration.

The average particle area was determined for all classification types over the 400 cm range, and Figure 4.8 shows that the 'unique'/'characteristic' particles are smallest. The maximum particle size for all three classifications is seen at 100 cm, after which the mean particle areas drop significantly. Only particles with an area less than 40 μm^2 making it to the 400 cm sampling range.

The experiments have thus shown that the size of a GSR particle, or IDGSR, is a function of the distance, x, from the firearm (Figure 8.4).

Consider a GSR particle made of a lead sphere of radius r, travelling with a velocity v_p. It is also assumed that the particle is entrained in a flow of gas (scenario 2) moving

horizontally at a velocity $v_{air} = v_p$ so there is no drag due to any differential velocity between the particle and the surrounding air. Therefore, the particles will fall under the effect of gravity alone (Figure 8.6).

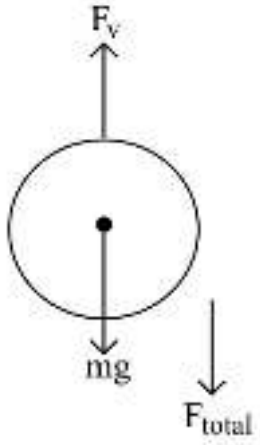

Figure 8.6: Diagram (not to scale) showing the effects experienced by a falling, spherical particle.

F_v is the drag force opposing falling through the atmosphere. Therefore, the resultant force, $F_{total} = mass \times acceleration$ of particles can be expressed as:

$$F_{total} = mg - F_v = mg - \frac{\rho C_d A v^2}{2} \tag{8.4}$$

where,
m = mass of particle (kg)
ρ = density of air, $1.225\,kg\,m^{-3}$
A = cross-sectional area of sphere, $\pi\ r^2$ (m^2)
C_d = drag coefficient of sphere, 0.5.

Therefore, Equation 8.4 can be written in a differential form.

$$m(\frac{dv}{dt}) = mg - \frac{\rho C_d A v^2}{2} = \frac{2mg - \rho C_d A v^2}{2} \tag{8.5}$$

Rearranging gives:

$$\left(\frac{dv}{dt}\right)\frac{2m}{2mg - \rho C_d A v^2} = 1$$

$$\left(\frac{2m}{2mg - \rho C_d A v^2}\right) dv = dt$$

and assuming variables are separable,

$$2m \times \left(\frac{1}{2mg - \rho C_d A v^2} \right) dv = dt$$

$$2m \times \left(\frac{1}{\rho C_d A (\frac{2mg}{\rho C_d A} - v^2)} \right) dv = dt$$

$$\frac{2m}{\rho C_d A} \times \frac{1}{\left(\left(\frac{2mg}{\rho C_d A} \right) - v^2 \right)} dv = dt \tag{8.6}$$

Let:

$$B = \sqrt{\frac{2mg}{\rho C_d A}}$$

Therefore, Equation 8.6 can be written as:

$$\frac{2m}{\rho C_d A} \times \frac{1}{(B^2 - v^2)} dv = dt$$

Integrating both sides:

$$\frac{2m}{\rho C_d A} \int_o^v \frac{1}{(B^2 - v^2)} dv = \int_o^t dt$$

and using the standard integral:

$$\int \frac{1}{(B^2 - x^2)} dx = \frac{1}{2B} \ln \left(\frac{B + x}{B - x} \right)$$

Therefore,

$$\frac{2m}{\rho C_d A} \times \frac{1}{2B} \ln \left(\frac{B + v}{B - v} \right) \Big|_o^v = t \Big|_o^t$$

$$\frac{m}{\rho C_d A} \times \frac{1}{B} \ln \left(\frac{B + v}{B - v} \right) = t \tag{8.7}$$

which, after some algebra, becomes:

$$v = B \times \left[\frac{\exp\left(\frac{B \rho C_d A t}{m}\right) - 1}{1 + \exp\left(\frac{B \rho C_d A t}{m}\right)} \right] \tag{8.8}$$

Recall,

$$B = \sqrt{\frac{2mg}{\rho C_d A}}$$

which is the terminal velocity of a particle falling under gravity. To confirm the calculations, the properties of Equation 8.8 can be verified.

As:

$$m \to \infty, v \to B = \sqrt{\frac{2mg}{\rho C_d A}}$$

which means that the terminal velocity of a particle falling under gravity is instantly reached (no time dependence).

Whereas,

$$m \to 0, v \to 0$$

indicating particles never reach terminal velocity. Therefore, we have confidence that Equation 8.8 captures the essential physics.

To simplify, we ignore the constant terms to see how v varies with r,

$$B \propto \sqrt{\frac{r^3}{r^2}} \propto \sqrt{r}$$

$$\mathrm{v_t} \propto \sqrt{r} \times \left[\frac{\exp\left(\frac{\sqrt{r}\times r^2 \times t}{r^3}\right) - 1}{1 + \exp\left(\frac{\sqrt{r}\times r^2 \times t}{r^3}\right)}\right]$$

$$\mathrm{v_t} \propto \sqrt{r} \times \left[\frac{\exp\left(r^{-0.5t}\right) - 1}{1 + \exp\left(r^{-0.5t}\right)}\right] \tag{8.9}$$

which can be plotted for different values of r (Figure 8.7).

Therefore, Figure 8.7 shows that larger particles will fall out of the gas stream faster than the smaller particles. Realistic values can then be applied to Equation 8.8 to determine a particle's trajectory in an attempt to reproduce the results from the rim-fire experiments detailed in Chapter 4 (Figure 8.8).

Figure 8.8 follows the general distribution of the particle sizes seen in Chapters 4 and 5. However, this is still a simplification and does not take into account turbulence between the gas from the firearm and the ambient air, and/or horizontal air resistance encountered as the velocity of the particles decouples from the gas stream. Such works are beyond the scope of this thesis, but could be the subject of future work.

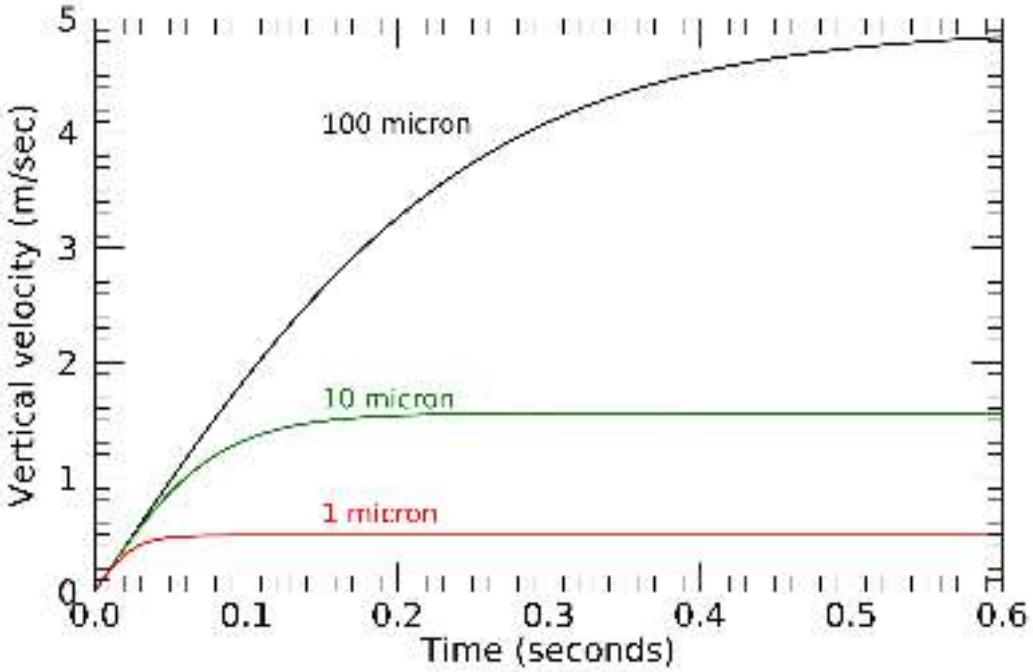

Figure 8.7: Graph showing the vertical velocity over time for different values of particle radius, r, indicating larger particles will fall out of the gas stream faster than smaller particles.

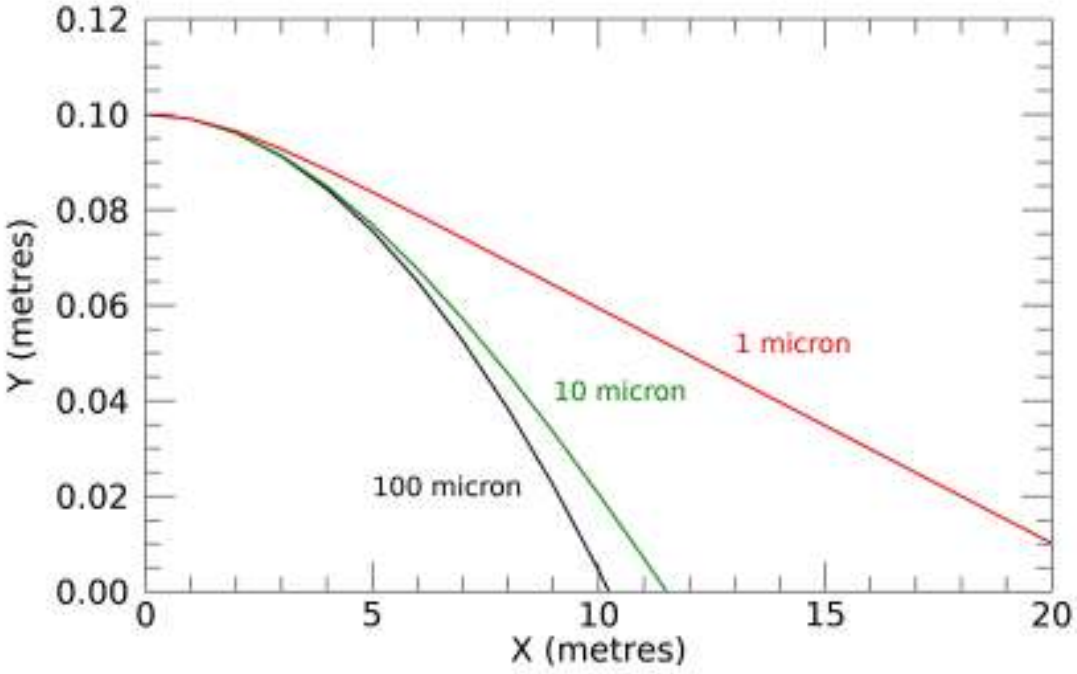

Figure 8.8: Graph showing the trajectories for projectiles of different sizes which demonstrate that larger particles are found closer to the firearms than smaller ones. The firearm is assumed to be 0.1 m from the ground.

8.2 Heating and cooling mechanisms

The results of the experiments carried out using the LGG (see Chapter 7) provided useful insight into the formation processes of the primer residues during launch. To gain further insight into the cooling and heating processes that happen during a GSR particle's passage through an atmosphere and impact onto a surface, it is useful to consider the various separate physical mechanisms: impact heating and radiative and convective/conductive cooling.

The results of the AUTODYN modelling, with regards to projectile impact heating, demonstrate that a particle reaches temperatures higher (and in some cases much higher) than the melting point of Pb. However, AUTODYN has limitations and cannot model the phase changes associated with that heating (i.e. impact melting). Nevertheless, we can consider a simple case of a sphere impacting a solid surface (which is assumed rigid and does not deform). The only energy present in the system just prior to impact is the kinetic energy of the impactor, E_0:

$$E_o = \frac{1}{2}mv^2 \tag{8.10}$$

where,
m = mass of the particle (kg)
v = velocity ($m\,s^{-1}$).

Upon impact, the assumption is made that 50% of the kinetic energy goes into deforming the projectile ('plastic work') and 50% goes into heating, and possibly melting, of the projectile. This 50% assumption is justified by the energy conservation plots that are generated inside AUTODYN, which show that approximately 50% of the initial energy is plastic work (but remembering that AUTODYN does not consider phase changes). Therefore, we make the assumption that the energy available for heating and phase changes, E_a:

$$E_a = \frac{1}{4}mv^2 \tag{8.11}$$

The amount of energy required to heat, E_h, a substance is:

$$\Delta E_h = mc\Delta\Theta \tag{8.12}$$

where,
c = specific heat capacity ($J\,kg^{-1}\,K^{-1}$)

$\Delta\Theta$ = temperature change (K),

and the amount of energy required to completely melt, E_m, a substance is:

$$E_m = mL_f \tag{8.13}$$

where,

L_f = latent heat of fusion ($J\,kg^{-1}$).

Thus, the problem is divided into two parts. Firstly, the amount of energy, E_{heat}, required to heat an impacted particle from it initial temperature, Θ_o, to its melting point, Θ_m was calculated using Equation 8.14.

$$E_{heat} = mc(\Theta_m - \Theta_o) \tag{8.14}$$

Therefore, the energy remaining to melt the projectile, E_{melt} is:

$$E_{melt} = \frac{1}{4}mv^2 - E_{heat} \tag{8.15}$$

The fraction molten, F_{melt} can then be defined as:

$$F_{melt} = \frac{E_m}{E_{melt}}$$

$$F_{melt} = \frac{mL_f}{\left(\frac{1}{4}mv^2 - E_{heat}\right)}$$

$$F_{melt} = \frac{mL_f}{\left(\frac{1}{4}mv^2 - mc(\Theta_m - \Theta_o)\right)}$$

which, when simplified, becomes:

$$F_{melt} = \frac{L_f}{\left(\frac{1}{4}v^2 - c(\Theta_m - \Theta_o)\right)} \tag{8.16}$$

where F_{melt} is capped at a maximum value of 1, indicating the particle has totally melted.

Using the values in Table 8.1, F_{melt} as a function of material and impact velocity can be plotted (Figure 8.9).

Table 8.1: Table showing the relevant material data to determine F_{melt} as a function of material and impact velocity.

Material	Θ_m (K)	Specific heat capacity ($JKg^{-1}K^{-1}$)	L_f (JKg^{-1})
Lead	600	130	24500
Antimony	903	210	160000
Barium	1000	204	55800
Copper	1360	385	210000

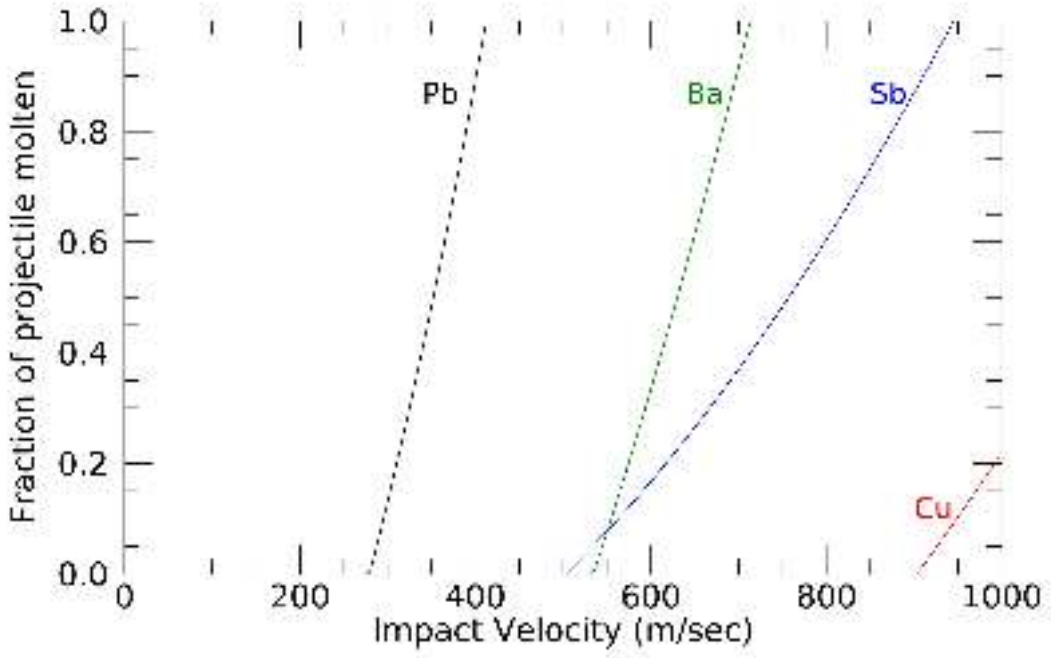

Figure 8.9: Graph showing the fraction of projectile that is molten, F_{melt}, as a function of material and impact velocity. Note, as mass cancels, the fraction molten is size independent.

Interestingly, Figure 8.9 indicates that there is only a relatively narrow range of velocities ($\sim$ 275 - 400 m s^{-1}) for which partially molten lead particles would be expected, along with much higher velocities being needed to induce impact melting in the other metals. This is also what was observed. At velocities of approximately 350 m s^{-1}, the modelling indicates that a significant proportion of the impactor reaches its melting point. However, the temperature increase is a sensitive function of the impact speed and, vitally, the AUTODYN modelling does not account for the energy required for a phase change in the material. Therefore a particle could be 'flash heated' to several thousand K for a fraction of a second, but still remain solid, as seen in the results from firing the shaken, unheated powders at differing speeds, and only seeing significant melting of Pb up to speeds of approximately 500 m s^{-1}, consistent with the first order analysis undertaken here. Therefore, as the maximum impact velocity is $\sim$ 300 m s^{-1},

due to the lack of damage on the silicon substrates (Price M.C. et al., 2014) in Experiment 2 (see Chapter 5), any observed melting of Sb, Ba or Cu particulates in GSR must be due to its initial state in the firearm discharge plume.

The morphologies for the GSR particles observed experimentally during the LGG primer launch experiments appear to be size-dependent. Smaller particles seem to have solidified into spheres whereas the larger ones still retain a molten centre and exhibit different extents of melting. It is insightful to consider, therefore, the different possible cooling mechanisms, and how they depend on particle size. For convective cooling, the mechanism is described by Newton's Law of cooling (Equation 8.17).

$$\dot{Q} = hA(T_{\mathrm{f}} - T)^b \tag{8.17}$$

where,
$\dot{Q}$ = heat transfer per unit time (W)
A = area of the object (m^2)
h = heat transfer coefficient (W / m^2K)
T = surface temperature of the object (K)
T_{f} = fluid temperature (K)
b = a scaling exponent.

However, to fully describe the cooling process we also need to consider radiative cooling. Coupling radiative and convective cooling mathematically is a complex process, and quickly adds to the requirement for computational (i.e. non-analytical) solutions.

Ansys' "Transient Thermal" software package, part of the Ansys Mechanical suite of engineering design tools (which include AUTODYN), was used to help model the cooling of spheres of different sizes under both radiative only, and radiation plus convective conditions.

In the models we assumed an emissivity of 1, and a value of the convection coefficient, h, of 300 W/m^2K - which represents a high, but realistic, value of cooling due to a high speed (approximately 100 m s^{-1}) air stream (Saidi M. & Abardeh H. (2010); Morgan V.T. (1975)).

The spheres were then modelled with radii of 1, 10 and 100 μm respectively, cooling from 573 K (300 °C) to ambient and the temperature at the centre of the sphere was modelled (Figure 8.10).

Interestingly, the radiative cooling time for a 100 µm diameter sphere is greater than ten seconds, but drops very quickly for smaller particles. To compare with the results of the LGG experiments detailed in Chapter 7, we estimate that the length of

time a GSR particle is in flight for before landing on the silicon substrate was ~ 0.01 second (i.e. the time take for a particle travelling at $100\,\mathrm{m\,s^{-1}}$ to travel 1 m, which approximates the set-up used in those experiments). After zooming in on Figure 8.10, we obtain Figure 8.11.

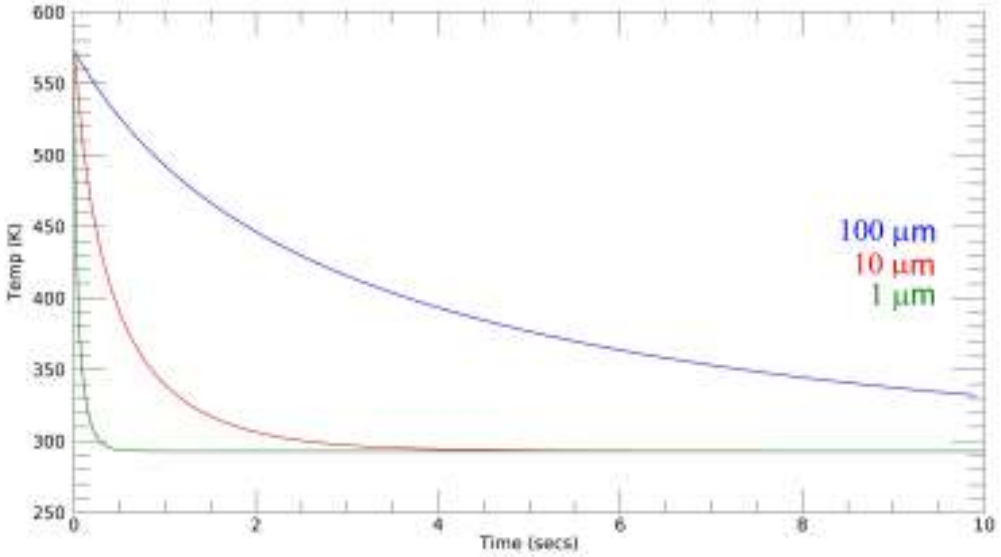

Figure 8.10: Graph showing the radiative cooling curves (no convection) for spheres of 100 μm (blue), 10 μm (red) and 1μm radii (green).

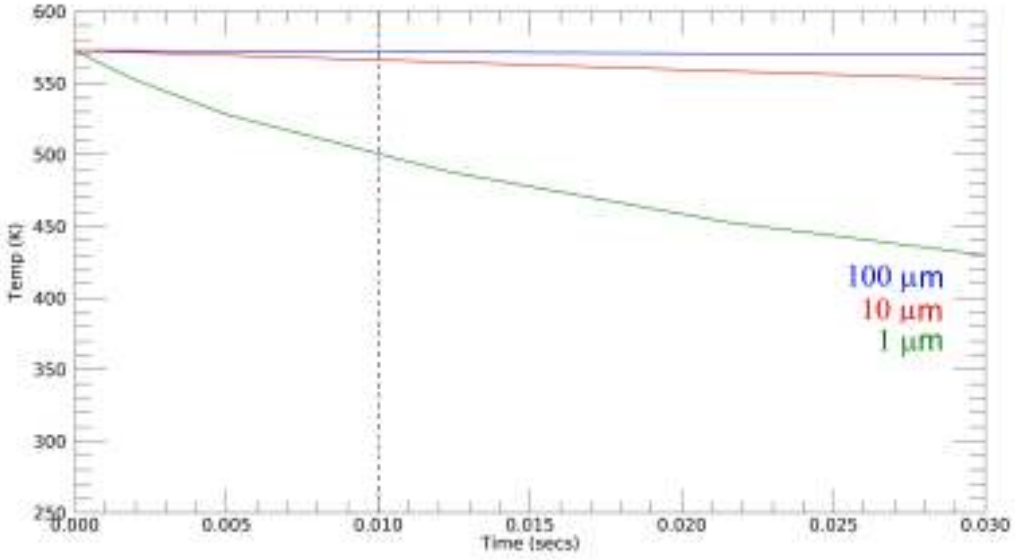

Figure 8.11: Radiative cooling curves (no convection) for spheres of 100 μm (blue), 10 μm (red) and 1μm radii (green). The dashed line represents the approximate length of time a particle is in-flight.

Figure 8.11 demonstrates that there is very little time for the particle to radiatively

cool, even for the smallest particles modelled here. This is in agreement with the experimental findings of the LGG experiments where (for the shots performed under vacuum) the majority of residues looked molten.

Once convection is added into the model, we obtain Figure 8.12. The data presented here is the maximum likely cooling, and it would be less if the particle is still entrained (or partially entrained) within the gas stream.

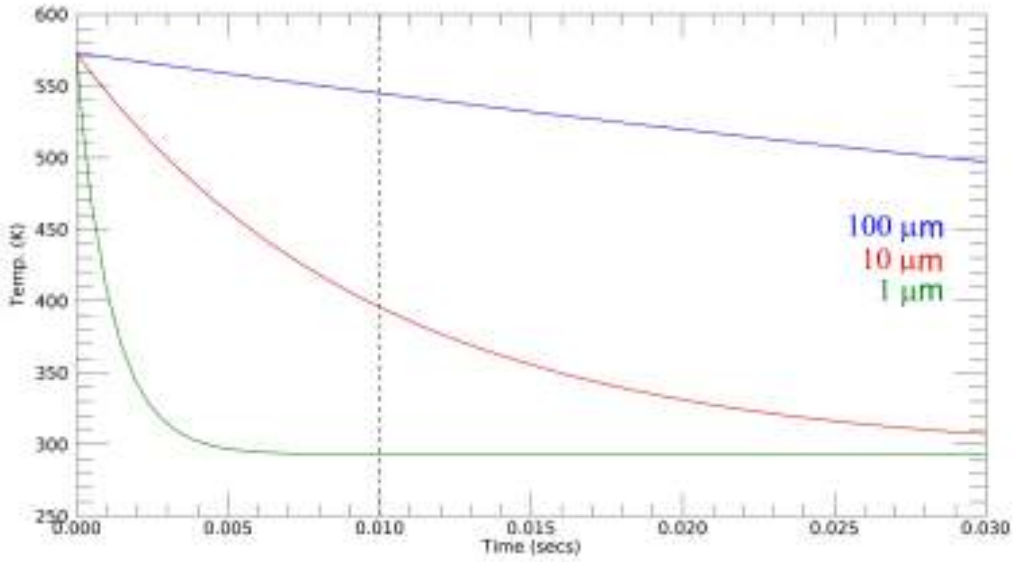

Figure 8.12: Radiative cooling curves (radiation and forced air convection) for spheres of 100 μm (blue), 10 μm (red) and 1μm radii (green). The dashed line represents the approximate length of time a particle is in-flight.

As can be seen, with the addition of convection cooling, the very smallest spheres can cool from the melting point to ambient before landing, but the for spheres of the order of 10s of microns in diameter, they could be in a mixed state of molten and solid. Again, this is what is seen experimentally (Figure 7.8).

One final model aimed to determine how long a molten disc of lead would take to cool once it had landed on a silicon substrate. The model is shown in Figure 8.13. Figure 8.14 shows the results of this model, and illustrates that the lead would have 'frozen' within a few micro-seconds of landing on the silicon. Again, this corresponds to the dynamic looking images seen in the experiments where the splats look almost frozen in time.

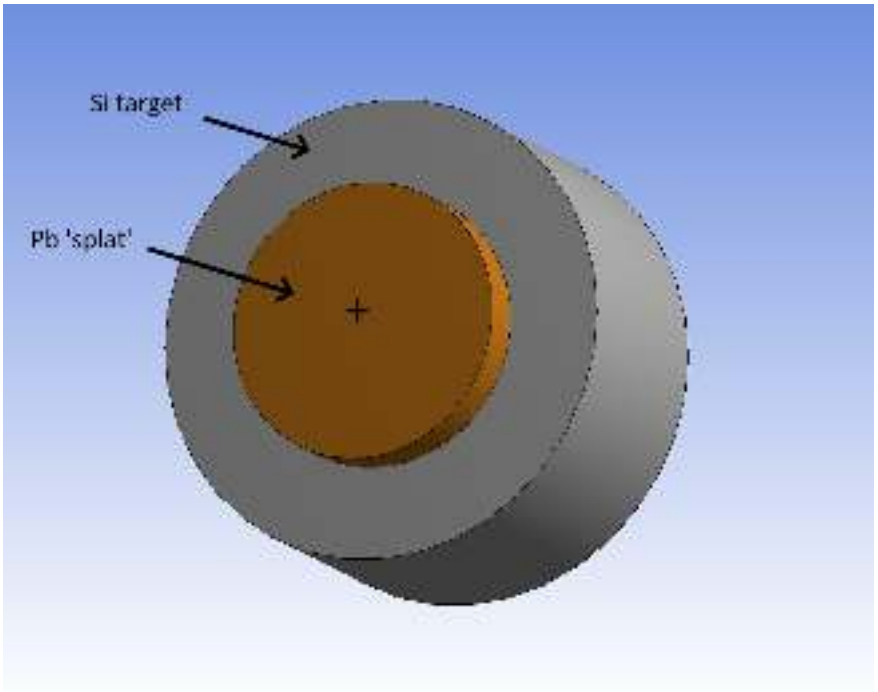

Figure 8.13: Simple model of a 20 µm diameter lead disc (brown) at an initial temperature of 573 K on a silicon (grey) substrate at (298 K). The '+' represents the position at which the temperature was modelled.

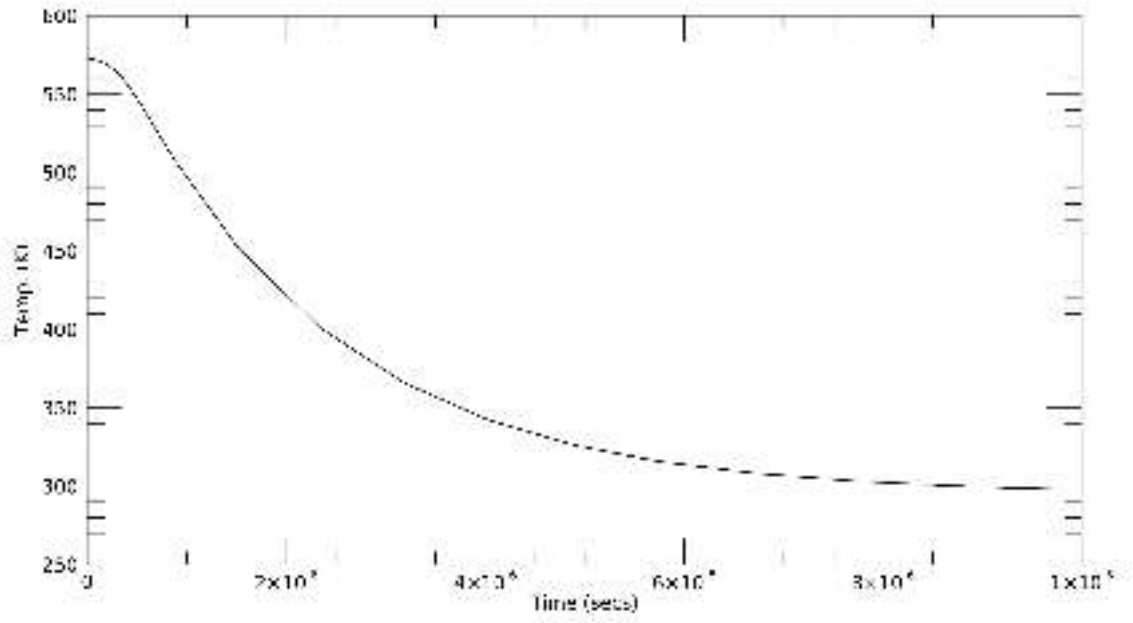

Figure 8.14: Cooling curve for the centre of a 20 μm diameter lead disc at an initial temperature of 573 K on a silicon substrate at 298 K.

This relatively simple modelling goes some way to explaining the range of morphologies seen across the experiments: small spheres cool very quickly, and thus appear

mostly spheroidal, whereas larger objects could still be completely/partially molten on landing to give the fascinating array of IDGSRs seen.

8.3 Differences in composition and morphology

The results from the morphological examination of the impact-disrupted GSRs (see Chapter 5) indicate that there is a clear pattern in class type as a function of distance. Table 5.1 indicates that at around the centre of the sampling range, at approximately 40 cm from the firearm, the residues analysed primarily fall within Classes 1, 3 and 4, producing the largest number of particles encountered over the 400 cm and 100 cm sampling range using the carbon and silicon substrates respectively. Therefore, due to the consistency in the distance at which the maximum number of particles are collected, it appears that the maximum dispersion of the firearm discharge plume using this firearm and ammunition combination is at approximately 40 cm from the firearm. These data also suggest that, although these residues are not prominent on the samples placed within the first 20 cm of the firearm, they have still not had sufficient time to cool in-flight, resulting in their liquid and molten forms. This reinforces the hypothesis that spheres are being entrained in the gas from the firearm as particles moving with the air would likely result in a shorter cooling time, as discussed earlier in this section.

Upon examination of the elemental composition of the different particle classes, it can be seen that the more liquid the appearance of the particle, the higher the lead content of said particle appears to be. However, the elemental composition results in Figure 5.9 indicate that there is very little variation in the individual particle morphologies. This could suggest that the primary difference for the differing morphologies may lie within the internal elemental composition of particles. However, due to time constraints this was not investigated, but would be a fundamental part of future work.

Despite the general lack of particles, the particle morphologies for the residues observed with both the AX308 and G36C firearms (Figures 6.9 and 6.10 respectively) appear to closely resemble the 'characteristic', spheroidal GSR morphology. However, K was frequently detected at levels above the 1% threshold, with a maximum abundance of 39.96% wt. Investigation of numerous firearm and ammunition types by Wallace J.S. (2008) indicates that K, in conjunction with sulphur (S), is often observed in GSR (or FDR, as referred to by Wallace J.S. (2008)), despite not being a 'characteristic' GSR element. The presence of these elements often suggests the use of black powder, with potassium chlorate being used in primer compositions (Bydal B.A. (1971); Styers G.R. (1987)) prior to barium nitrate. In this set of experiments, trace amounts of S

were also detected at $\leq 2\%$ levels, but were excluded from analysis due to potential background contamination. Polysulphide adhesives are widely investigated and manufactured (Bishop J. (2011); Ebnesajjad S. & Landrock A.H. (2015)) and the carbon tape applied to the substrates used to collect the discharged residues, in part, consist of sulphur due to the tape's adhesive layer. As the trace amount of sulphur were barely distinguishable from the background, the trace amounts of sulphur detected could not solely be attributed to GSR.

As mentioned in Chapter 6, the presence of K can also be attributed to the use of flash suppressors. Potassium nitrate (KNO_3) and potassium sulphate (K_2SO_4) are often used as chemical flash suppressors by preventing the ignition of fuel rich combustion gases that are expelled from the barrel (Varghese T.L. & Krishnamurthy V.N., 2017). This is done by introducing species which slow down reaction rates making ignition more difficult (Young H.H. (1954); Carafagno S.P. & Rudyj O.N. (1960); Cohen A. & Decker L. (1981)). However, K-rich flash suppressors have the disadvantage of producing smoke (Wallace J.S. (2008); Varghese T.L. & Krishnamurthy V.N. (2017)).

In this chapter, we have discussed some of the main findings of the thesis and developed several models which help to explain these findings and give new insights into the mechanisms of GSR formation. The next, and final, chapter lists the main conclusions of this work and details new avenues of research that could be explored by follow-up researchers.

Chapter 9

Conclusions

In this thesis, the formation mechanisms and distribution of GSR particles were investigated using both experimental procedures, as well as hydrocode computer modelling. The first objective that was initially to be investigated was to determine the distance range at which GSR is present, and examine individual particle morphologies at each distance (see Chapters 4 and 5). In this set of experiments, 5.56 mm CCI Mini-Mag rimfire ammunition in conjunction with a Browning Buck Mark long rifle pistol were used and it was found that (with this given firearm and ammunition combination) GSR particles were successfully collected and detected at up to 400 cm from the firearm (down the firing line), the maximum distance sampled, using Oxford Instruments' automated INCA GSR software.

INCA GSR was successfully used to discriminate between GSR and non-GSR particles using morphological and compositional exclusion parameters. In order to identify a particle as having originated from a firearm and be classified as GSR, spheroidal particles were first identified using INCA GSR's morphological filters. However, as 'unconventional' GSR morphologies were encountered during sub-micron analyses using the FEG-SEM/EDX (see Chapter 5), the morphological filters were disabled for all automated analyses, and particles were classified solely based on their relative elemental compositions. INCA GSR successfully identified and classified 'characteristic', 'indicative' and 'environmental' particles at all the distances investigated, but was found to be very sensitive to SEM set-up conditions and beam stability. The size of

the GSR particles was found to drop off with distance, with a maximum particle area of 100 μm^2 for 'unique' GSR particles at 100 cm from the firearm, for this firearm and ammunition combination. The particle number distribution also changes with distance from the firearm, but 'unique'/'characteristic' GSR particles were still detected at the maximum distance investigated, 400 cm from the firearm. This demonstrates that samples and swabs collected for trace GSR analyses should also be taken at distances > 2 m for any shooting event.

As part of the GSR distribution experiments (see Chapter 4), the approximate velocity at which GSR particles travel prior to impact was attempted to be determined. This was done using high purity, silicon wafer targets that can display damage and 'bruising' that can be identified using Raman spectrometry, for velocities as low as 362 $m\,s^{-1}$. As a result of this investigation, a selection of 'uncharacteristic', molten-like residues were identified and were characterised as impact-disrupted GSR, or IDGSR (see Chapter 5). Although these residues may not be spheroidal in shape, they are a product of a discharged firearm and are, therefore, GSRs. The IDGSRs were classified according to their degree of melting, with class 0 particles having a completely molten-like appearance and class 7 particles being solid and spheroidal.

Although INCA GSR allowed for an overall elemental composition of the residues to be identified sufficiently to classify particles into their corresponding ranks, there was little information as to the distribution of those elements within the individual particles. This is why the second objective that was to be investigated was to determine the elemental composition for each particle class. This was done to establish whether different morphologies are due to varying elemental compositions using the FEG-SEM/EDX, allowing for compositional and morphological analyses at the submicron level. However, the results of these experiments suggested that the residues travelled at velocities < 362 $m\,s^{-1}$ due to the lack of damage on the silicon substrates, and, ultimately, the elemental composition of GSR does not change significantly as a function of distance for this firearm and ammunition combination. This suggested that there was another factor affecting particle formation, such as in-flight cooling and/or impact melting.

To corroborate these results, the experiments investigating GSR distribution and particle morphology were repeated using a Heckler & Koch G36 Carbine firearm (G36C) with 5.56 mm Federal Premium tactical bonded centre-fire ammunition, and an Accuracy International AX308 firearm (AX308) with 7.62 mm Federal tactical bonded semi-jacketed centre-fire ammunition, used by Kent Police (see Chapter 6). However, only a small number of particles were successfully collected onto the substrates, with G36C samples showing particles at up to (and including) 175 cm from the firearm,